



Computational Design Tool for the Synthesis and Optimization of Gel Formulations (SOGeF)

US Army STTR Phase II Project

**Final Report
(Draft)**

By:

Glen Wilt	CFDRC
Jonathan Hood	CFDRC
Jerry Jenkins	CFDRC
Matt Thomas	CFDRC

Jeff Morris	CCNY
Morton Denn	CCNY

Boris Khusid	NJIT
Yueyang Shen	NJIT

January 2009

CFDRC Project: 8731/Final

**Submitted to
US Army-RDECOM ACQ CTR**

**Technical Monitor: Ralph Anthenien
Contract Monitor: Leroy Hardy**

**US Army STTR Phase II Project
Contract # W911NF06C0186**

CFD Research Corporation

www.cfdrc.com

215 Wynn Drive • Huntsville, Alabama 35805 • Tel: (256) 726-4800 • FAX: (256) 726-4806 • info@cfrc.com

Report Documentation Page				Form Approved OMB No. 0704-0188	
Public reporting burden for the collection of information is estimated to average 1 hour per response, including the time for reviewing instructions, searching existing data sources, gathering and maintaining the data needed, and completing and reviewing the collection of information. Send comments regarding this burden estimate or any other aspect of this collection of information, including suggestions for reducing this burden, to Washington Headquarters Services, Directorate for Information Operations and Reports, 1215 Jefferson Davis Highway, Suite 1204, Arlington VA 22202-4302. Respondents should be aware that notwithstanding any other provision of law, no person shall be subject to a penalty for failing to comply with a collection of information if it does not display a currently valid OMB control number.					
1. REPORT DATE 30 JAN 2009		2. REPORT TYPE		3. DATES COVERED 29-09-2006 to 31-01-2009	
4. TITLE AND SUBTITLE Computational Design Tool for the Synthesis and Optimization of Gel Formulations (SOGeF)				5a. CONTRACT NUMBER	
				5b. GRANT NUMBER	
				5c. PROGRAM ELEMENT NUMBER	
6. AUTHOR(S)				5d. PROJECT NUMBER	
				5e. TASK NUMBER	
				5f. WORK UNIT NUMBER	
7. PERFORMING ORGANIZATION NAME(S) AND ADDRESS(ES) CFD Research Corporation, 215 Wynn Dr., 5th Floor, Huntsville, AL, 35805				8. PERFORMING ORGANIZATION REPORT NUMBER	
9. SPONSORING/MONITORING AGENCY NAME(S) AND ADDRESS(ES)				10. SPONSOR/MONITOR'S ACRONYM(S)	
				11. SPONSOR/MONITOR'S REPORT NUMBER(S)	
12. DISTRIBUTION/AVAILABILITY STATEMENT Approved for public release; distribution unlimited					
13. SUPPLEMENTARY NOTES					
14. ABSTRACT					
15. SUBJECT TERMS					
16. SECURITY CLASSIFICATION OF:			17. LIMITATION OF ABSTRACT Same as Report (SAR)	18. NUMBER OF PAGES 105	19a. NAME OF RESPONSIBLE PERSON
a. REPORT unclassified	b. ABSTRACT unclassified	c. THIS PAGE unclassified			

Abstract

Gel propulsion systems combine the best characteristics of solid and liquid propellants. The gel system stores like solid propellant, but flows like a liquid when pressurized, enabling throttle and restart capability similar to liquid propellants. In addition, gels have a lower vapor pressure compared to their liquid counterparts. Consequently, the storage containers holding them can be much lighter.

An enabling technology for the further advancement of gelled propulsion is the development of tools to render the synthesis of propellant formulations more systematic. In Phase I, various models were developed to support the project objectives. Given the multi-scale scope of the problem, first quantum mechanical and Grand Canonical Monte Carlo (GCMC) simulations were used. The results of these simulations were then fed into Stokesian models to compute stress characteristics. Finally, Brownian and continuum models were used for syneresis studies.

In Phase II, Quantitative Structure-Property Relationship (QSPR) techniques, in the form of a feed-forward / backpropagation neural network (NN), were employed to join together the molecular-scale, particle-scale, and continuum models begun in Phase I. In addition, a large-scale organic gel database (over 39 different entries) was created to train and validate the NN. To facilitate operator handling, the network and database were wrapped in a convenient and robust Graphical User Interface (GUI), written in the platform independent Python programming language. Preliminary results show that this software (named SOGeF-Synthesis and **Optimization of Gel Formulations**) offers a reliable and comprehensive design tool for the prediction of gel formulations. SOGeF uses gel constituent properties (i.e. solvent density, boiling point, silica content, etc.) to make predictions of gelled properties. This approach is advantageous over physics-based models in that input parameters are easily identified and can be arbitrarily chosen. In addition, as the size of the training database grows, SOGeF predictions become more reliable. This comprehensive approach accomplishes the Army's objective of a model to describe the physical properties of gelled propellants.

Preface

This is the final report for the US Army-RDECOM ACQ CTR STTR Phase II project entitled “Computational Design Tool for the Synthesis and Optimization of Gel Formulations (SOGeF)”. This project was sponsored by the US Army-RDECOM ACQ CTR (Contract Number W911NF06C0186), and performed by researchers at CFD Research Corporation (CFDRC Project Number 8731). The principal investigators were Dr. Stelu Deaconu and Dr. Glen Wilt (CFDRC), co-investigators were Dr. Jeff Morris (City College of New York) and Dr. Boris Khusid (New Jersey Institute of Technology) and the project manager was Matt Thomas (CFDRC). The Army-RDECOM technical monitor of this project was Dr. Ralph Anthenien and the contract representative was Leroy Hardy.

TABLE OF CONTENTS

Abstract.....	i
Preface.....	ii
Table of Contents.....	iii
List of Figures.....	v
List of Tables.....	ix
1. INTRODUCTION.....	1
1.1 Motivation and significance of the current research.....	1
1.2 Proposed solution: QSPR-Neural Network.....	2
2. PHASE I TECHNICAL OBJECTIVES AND ACCOMPLISHMENTS.....	3
2.1 Phase I Technical Objectives.....	3
2.2 Summary of Phase I Accomplishments.....	3
2.3 Rheology of Fumed Silica Gels.....	3
2.4 Syneresis of Fumed Silica Gels.....	7
2.5 Molecular Level Modeling and Simulations.....	13
2.6 Particle Scale Models and Simulation.....	15
3. PHASE II TECHNICAL OBJECTIVES AND ACCOMPLISHMENTS.....	18
3.1 Objectives of the Phase II study.....	18
3.2 Summary of the Phase II accomplishments.....	18
4. TECHNICAL APPROACH.....	20
4.1 Measurement Procedures.....	20
4.1.1 Density.....	20
4.1.2 50 Caliber Test.....	20
4.1.3 Modulus of Elasticity.....	21
4.1.4 Syneresis.....	22
4.1.5 Extrusion and Drop Formation.....	28
4.1.6 Gel Structure During Solvent Evaporation.....	30
4.1.7 Rheometry (Yield Stress, Storage, and Loss Modulus).....	31
4.1.8 Gelation Dynamics.....	35
4.1.8.1 Dynamic Light Scattering (DLS).....	35
4.1.8.2 Dynamic Rheology.....	37
4.2 Organic Gel Mixing / Database Development.....	40
4.2.1 Initial Production.....	40
4.2.2 Gel Test Matrix.....	41
4.2.3 Extraneous Factors.....	44
4.3 QSPR Model: Neural Network.....	45
4.3.1 Theory.....	45
4.3.1.1 Training.....	46
4.3.1.2 Prediction Risk: Nonlinear Cross Validation (NCV).....	47
4.3.1.3 Sequential Network Construction (SNC).....	47
4.3.2 Application.....	48
4.3.2.1 Descriptors / Predictors.....	48
4.3.2.2 Training and Validation.....	52
4.3.3 Python GUI.....	62
4.3.3.1 Graphical User Interface Application Development.....	62

4.3.3.2	Development of a Chemical Compound Library.....	62
4.3.3.3	Design and Implementation of Chemical Compound Library Management Page.....	63
4.3.3.4	Design and Implementation of Calculation Page.....	64
4.3.3.5	Design and Implementation of Training Page	65
4.4	Dynamic Brownian / Stokesian Gelation Simulation	66
5 .	SUMMARY	70
6 .	CONCLUSIONS.....	71
7 .	RECOMMENDATIONS.....	73
9.	REFERENCES	74
	Appendix A (Solvent Descriptor Values).....	75
	Appendix B (Additional Syneresis Data)	78
	Appendix C (NN Code Listing).....	81

LIST OF FIGURES

Figure 1: View of Gelled MMH/IRFNA Combustion Inside a Vortex Motor 115 ms After Ignition. The Striations on the Upper Left Hand Corner of the Window are Deposits of Silica. The Development of an Innovative Computational Design Tool for the Synthesis and Optimization of Gel Formulations (SOGeF) in Phase II has made Propellant Formulation Development More Systematic.	1
Figure 2: SOGeF Program Flowchart.....	2
Figure 3: G' (filled symbols) and G'' (open symbols) for Gel 9 following the same loading procedure with an additional pre-shear at 0.02 /s for 2 and 5 minutes. The response is characteristic of a strong gel, with the elastic component (G') independent of frequency and more than an order of magnitude larger than the viscous component (G'').	4
Figure 4: Step-stress and recovery curves at different imposed shear stresses, Gel 8.5.....	5
Figure 5: Linear moduli versus strain at a frequency of 1Hz for Gel 9 (triangles) and Gel 8 (squares).	5
Figure 6: Relaxation modulus of Gel 9 as a function of time following step strains of 0.5 (circles), 1 (triangles) and 5% (squares).	6
Figure 7: Storage (circles) and loss moduli (triangles) at 1 rad/s for Gel 1B versus strain.....	7
Figure 8: Storage and Loss Moduli of Gel 1C As Functions of Frequency.	7
Figure 9: Photos of a GEL 8 sample before (left) and after (right) the 90-min exposure to 5,500 G at 20oC. The circle indicates the location of water exudated from the gel.	8
Figure 10: Syneresis of silica gels GEL 8, GEL 8.25 and GEL 8.5 for 200C following the 30-min exposure to acceleration (in G). The amount of exudated water is given as the fraction of the initial sample mass.	9
Figure 11: Time dependence of syneresis of GEL 8 following the exposure to acceleration for 20oC.	9
Figure 12: Time dependence of syneresis of GEL 8, GEL 8.25 and GEL 8.5 following the exposure to acceleration of 5,500G for 20oC.	10
Figure 13 Figure 14 Figure 15.....	11
Figure 16: The SEM images of structures formed by particles in GEL 8 revealed by supercritical extraction of water: (left) as-received; (right) following the 30-min exposure to 11,500 G at 200C, syneresis 33.12 (v/v) %.	12
Figure 17: Oxygen-17 NMR resonance peaks for (1) D2O, (2) D2O with Degussa A200 silica powder, and (3) D2O with GEL 8.	13
Figure 18: Four different structures of silicon clusters. The red atoms are terminal oxygen atoms (only bound to 1 Si atom), the blue atoms are bridging oxygen atoms (bound to two Si atoms) and the grey atoms are silicon atoms.	14
Figure 19: Calculated energies of the various molecular arrangements of SiO2 cluster and water as a function of center-of-mass separation distance.....	14
Figure 20: Snapshot of of final configurations a silica particle with water adsorbed to its surface at low and high relative humidities, respectively.	15
Figure 21: Adsorption isotherm for the adsorption of water onto the surface of a silica particle at 300 K compared to the experimental data [Meyer, 1966].	15

Figure 22: Examples of interparticle force forms employed, plotted as a function of r , with $r=1$ being particle contact. The squares denote a potential with a generalized Lennard-Jones (of 36–18 form) soft-core potential and minimum of $V/kT = -9.5$ at $r = 1.07$, while the crosses show a combined steeply repulsive hard-core potential near $r=1$ with a linear attraction out to $r=1.2$.	16
Figure 23: Plot of particle positions after 100 Brownian diffusion times ($100a^2/D_0$) showing clustering in a 15% by area dispersion with strong attraction.	17
Figure 24: Full symbols show structure in unit cell of a small two-dimensional attractive particle simulation, with minimum energy of -3 kT at $r/a = 2.05$, for Peclet number of $Pe = 0.1$ ($Pe = \gamma a^2/D_0$ where γ is the shear rate) after a strain of 10.	17
Figure 25: (A) Fisher Scientific Pycnometer, and (B) Digital Precision Balance Used to Determine Gel Density	20
Figure 26: Setup for Gel Sound Speed Measurements (1) DP 2000 Ultrasonic Doppler Velocimeter / Pulse Generator, (2) Tektronics TDS-210 Digital Oscilloscope, (3) Dial Caliper, (4) Gel Samples, (5) Ultrasonic Probe, and (6) Plexiglass Disk	22
Figure 27: Photos of Hexane Silica Gel Before (left) and After (right) a 30-min Exposure to 10,000G at 20°C. The Circle Indicates the Location of Organic Solvent Exudated From the Sample.	23
Figure 28: Time dependence of syneresis in organic solvents gelled with 9 w/w% fumed silica subjected to 5,000G acceleration at 20°C.	24
Figure 29: Syneresis of organic solvents (iso-pentane, n-pentane, hexane, heptane, octane, iso-octane, and decane) gelled with 9 w/w% fumed silica, following the 5 (top) and 10 (bottom) minute exposure to acceleration (in G) at 20°C.	25
Figure 30: Syneresis of silica gels SILICA 50, SILICA 8.25 (8.25 parts of water to 1 part of fumed silica by weight) and SILICA 8.50 (8.50 parts of water to 1 part of fumed silica by weight) following the 30-min exposure to acceleration (in G) at 20°C. The amount of exudated water is given as the fraction of the initial sample mass. [7].	26
Figure 31: Syneresis of organic-based silica gels with 9 and 11% (w/w) silica following the exposure to acceleration 20,000 (top) and 10,000 (bottom) G for 30min at 20°C.	27
Figure 32: Gel Jetting Setup: (Left) Experimental setup for testing pressure driven syneresis (Right) Syringe 3 loaded with gel. (Volume: 5ml; barrel ID: 11.6 mm, nozzle ID: 2.0 mm, nozzle length: 17.0 mm)	28
Figure 33: Pressure Driven Flow of a Hexane-based Gel Showing Drop Formation at 15 psi	29
Figure 34: Extrusion and Drop Formation of a Colloidal Silica Gel (4.7%) at the Same Flow Rate Through a 250-micron (Left) and 2-mm (Right) Orifice	29
Figure 35: NIKON fluorescence microscope system used to study solvent evaporation	30
Figure 36: Evolution of a Hexane-based Gel Structure Under Evaporation	31
Figure 37: Storage Modulus G' , Loss Modulus G'' , and Stress vs. Strain. Yield Stress ~ 460 Pa. (Tri-ethylamine 11% Cabosil)	33
Figure 38: Schematic representation of two possible scenarios that can occur in the case of silica particles dispersed in a liquid: (A) strongly H-bonding liquid (a solvation layer is formed on the particles by H-bonding, resulting in a stable sol);	

(B) weakly H-bonding liquid (the particles interact directly by H-bonding to form a gel) [9].	34
Figure 39: Hydrodynamic Radii of Clusters, Measured with DLS, During the Gelation Process Following Addition of Salt (% weight) at Various CS Percentages	36
Figure 40: Hydrodynamic Radii of Clusters, Measured with DLS, During the Gelation Process Following Addition of Salt (molarity) at Various CS Percentages	36
Figure 41: The storage and loss moduli obtained at a strain of 100% from the dispersion of 1.78-wt% salt and 10.31 wt % SiO ₂ . The same symbol, open and closed, respectively, is used for G' and G'' at the noted times after adding the destabilizing salt solution.	38
Figure 42: Elastic (G') and loss (G'') moduli a function of the oscillation frequency for a CS dispersion of 5.2 % silica by volume, and 0.347 M in NaCl at three times following addition of salt.	38
Figure 43: Strain Sweeps at 190 and 1450 Minutes After Salt Addition (0.347 M) for a Ludox Dispersion at $\phi = 0.047$.	39
Figure 44: (A) Gallon Size, Pneumatic Mixer, and (B) 500ml Hand Operated Mixer (Images Not to Scale).	40
Figure 45: Results of Yield Stress for Initial Test Matrix of Alkanes (CCNY data) Showing a Strong Dependence on Silica %.	42
Figure 46: Feed-forward / Backpropagation NN Architecture Used to Predict Gel Properties From Solvent Descriptors	45
Figure 47: Percentage Descriptor Influence for Alkanes (A, B, and C) and Alcohols (D, E, and F). NN Training with Set of Ten Descriptors and Six Gel Parameters	50
Figure 48: Average Euclidian Distance Between Input Pairs of the Alkanes and Alcohol Groups Showing Only a Slight Distinction Between the Groups	51
Figure 49: Average Distance (Accentric Factor) Between Input Pairs of the Alkanes and Alcohol Groups Showing a Significant Distinction Between the Groups	52
Figure 50: Comparison of NN Fit to its Training Values (Full 11% Data Base with 23 Hidden Neurons) Showing Good Agreement Over Most of the Training Data (Red-Large Spread in the Output Data, Yellow-Arbitrarily Chosen Output Values Used to Fill Void Data, Blue-Normal Data)	53
Figure 51: Comparison of NN Fit to its Training Values (Full 9% Data Base with 23 Hidden Neurons) Showing Good Agreement Over Most of the Training Data (Red-Large Spread in the Output Data, Blue-Normal Data)	53
Figure 52: Training on a Progressively Large Spread in the Training Set (Two Values) Showing a Significant Favor Towards the Larger Output.	54
Figure 53: Comparison of Average Fit Errors in a Re-Trained "Error NN" to the Original NN Indicating Significant Potential to Increase Overall Predictive Quality	59
Figure 54: Path Taken by SNC in Determining the Optimal Number of Hidden Neurons (11%-G' Data).	60
Figure 55: Comparison of Networks (Same Size) Trained with SNC and Random Initialization. Indicating That SNC has Potential Beyond Finding an Optimal Number of Hidden Neurons.	61

Figure 56: The custom XML schema of the chemical compound library	63
Figure 57: Screenshot of chemical compound library management page	64
Figure 58: SOGeF GUI Application Windows: (Left) Screenshot of calculate page (Right) Screenshot of training page	65
Figure 59: Form of the inter-particle force typical of silica in aqueous environments. The repulsive portion with local maximum away from contact ($r=2$) is due to charged surface	66
Figure 60: Mean square displacement (in units of particle radius a) as a function of dimensionless time, $t^* = Dt/a^2$ with D the bare-particle diffusion constant (Stokes-Einstein) for simulations by Brownian and Stokesian Dynamics (BD, SD) of identical initial configurations; the simulations differ in BD lacking hydrodynamic interactions which are rigorously accounted in SD. These are conditions yielding strong gels	67
Figure 61: Number of bonds, defined as particle pairs having centers within 2.3 radii, as a function of dimensionless time with 124 particles in the unit cell	68
Figure 62: (Left) Snapshot of particle configuration for an initially uniformly distributed system, with 1000 particles in the unit cell, at solids fraction of $\phi =$ 0.05 and the force parameter (see Fig 3) of $A=20$. (Right) The pair distribution function of a gelling system, showing large value at contact and local crystalline ordering	68

LIST OF TABLES

Table 1: Characteristics of structures formed by silica particles	10
Table 2: Summary of 50-Caliber Test Results Showing a Much Improved Pass Rate in the 11% Data Over the 9% Data.....	21
Table 3: Reproducibility of Syneresis Measurements	23
Table 4: Syneresis of organic solvents gelled with 9 w/w% fumed silica following the exposure to 500G, 2,000G and 30,000G accelerations for 5 min and 90min at 20°C.	24
Table 5: Comparison of Syneresis after Long Storage Time (Decane).....	28
Table 6: DLS-Based Measurements of Gelation Time at Various NaCl Concentrations (From Results Shown in Figure 16).....	37
Table 7: The (9%) Gels Database (06/08/2008)	43
Table 8: The (11%) Gels Database (06/08/2008)	43
Table 9: List of Repeat Mixes Used to Determine Extraneous Factors in Gel Preparation	44
Table 10: MEP Derived Parameters of Alkanes and Alcohols (Originally Intended as Descriptors in the QSPR Model)	48
Table 11: Most Effective Descriptor Set (Solvent Properties) To Date (1/12/09) Manually Selected to Optimize NN Output.....	49
Table 12: Predicted 11% Values Obtained by Removing All of the Listed Solvents from the Training Set (13 Hidden Neurons and Single Output Variable).....	55
Table 13: Predicted 9% Values Obtained by Removing All of the Listed Solvents from the Training Set (13 Hidden Neurons and Single Output Variable).....	55
Table 14: Comparison of Predictions Made with Arbitrary Error (-30%) Imposed on One of Ten Training Values (Fit Error Was Within 0.001% for Each Case). Showing Significant Loss in Average Prediction Quality (11% Data).....	57

1. INTRODUCTION

1.1 Motivation and significance of the current research

Gel propulsion systems combine the best characteristics of solid and liquid propellants. The gel system stores like solid propellant, but flows like a liquid when pressurized, enabling throttle and restart capability similar to liquid propellants. In addition, gels have a lower vapor pressure compared to their liquid counterparts. Consequently, the storage containers holding them can be much lighter.

Gelled propellants are physical gels that are formed and stabilized in the solvent mainly through physical interactions (secondary forces like hydrogen bonding, van der Waals forces, hydrophobic forces, etc.) between polymer molecules and/or particles. The common feature of physical gels is a fragile space-filling connected network. Here we focused entirely upon gelation caused by the addition of solid particles, in particular fumed silica (FS), with the goal of being able to predict thermodynamic and rheological properties of this network based on knowledge of the component liquids and particles.

The physical interactions, which cause gelation, will impact upon the preparation, loading, storage, flow, injection, atomization, and combustion of a gelled propellant in a propulsion system. The properties required for a propellant may be obtained by manipulation of the chemical architecture and chemical environment of its components. In Phase I, we focused primarily on the gel performance in storage and transportation, where the material must have sufficient rigidity to maintain solids in suspension (added metallic powders, for example), and also be stable against network collapse and syneresis. Our Phase I emphasis was on gelation by fumed silica for a range of liquid propellant and oxidizer formulations. The propellant and oxidizer systems were treated as individual gels, i.e. systems where mixing occurs only as part of the combustion process was considered.



Figure 1: View of Gelled MMH/IRFNA Combustion Inside a Vortex Motor 115 ms After Ignition. The Striations on the Upper Left Hand Corner of the Window are Deposits of Silica. The Development of an Innovative Computational Design Tool for the Synthesis and Optimization of Gel Formulations (SOGeF) in Phase II has made Propellant Formulation Development More Systematic.

An enabling technology for the further advancement of gelled propulsion is the development of tools to render the synthesis of propellant formulations more systematic. The efforts of this project have established a Quantitative Structure Property Relationship (QSPR) software tool (named SOGeF-Synthesis and Optimization of Gel Formulation) that can be used to predict gel physical properties from the gel's constituent properties.

A key advantage of SOGeF is that, apart from training, model predictions are explicit and do not require lengthy physics-based gelation simulations. In addition, SOGeF input parameters are easily identified, as apposed to the challenging specification physical constants in gelation models. Also, as the size of the training database grows, predictions from SOGeF will only become more reliable, whereas the accuracy of physics-based models is relatively fixed.

1.2 Proposed solution: QSPR-Neural Network

The overall flow diagram of the SOGeF software is given in Figure 2. SOGeF operates by pulling select training data from a gel property database, forming intrinsic relationships between the gel descriptors (constituents) and predictors (gel properties), and storing the relationships in a functional form (QSPRs) for future predictions. The QSPR selected for this study was that of a feed-forward / backpropagation neural network.

The training data set can be created from computed and / or experimental data. In our Phase II implementation, emphasis was placed on generating experimental data. CFDRRC teamed up with the New Jersey Institute of Technology (NJIT) and City College of New York (CCNY) to measure the properties of over 39 different organic-based gels. These were used to train SOGeF in two distinct categories of gels (9 and 11% silica content by weight).

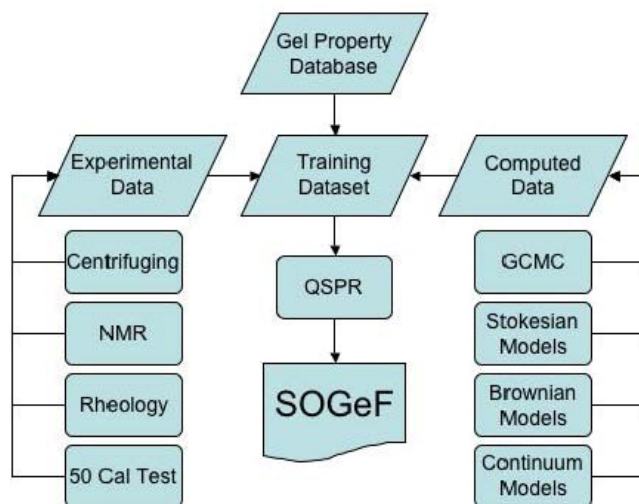


Figure 2: SOGeF Program Flowchart

2 . PHASE I TECHNICAL OBJECTIVES AND ACCOMPLISHMENTS

2.1 Phase I Technical Objectives

The primary technical objective of the Phase I program was the development of a model(s) to describe the physical properties of gelled propellants. To obtain these goals requires an understanding of the physico-chemical structure of propellants and its relation to the various material properties that takes us beyond the identification of mere empirical trends.

Specific objectives of the Phase I research included:

- i. Identification of critical parameters which affect the structural and material property characteristics of gelled propellants
- ii. Provide the basis for modeling gelled propellant performance based on the component properties

2.2 Summary of Phase I Accomplishments

Experimental studies were conducted at CCNY on the rheological properties of the gels while NJIT conducted syneresis studies. Given the difficulties, both infrastructural and logistic, associated with mixing and shipping samples of hypergolic gels to the various research institutions, it was decided to work with gel simulants in Phase I. The simulant chosen for these preliminary studies was a gel composed on fumed silica and water. To ensure consistency and statistical reproducibility, all samples were prepared by CFDRC in single batches and subsequently divided and sent to the various labs for testing. All gels contained Cabot Cab-O-Sil M5 fumed silica. Four different types of gel were prepared. The first was a standard 8:1 water silica gel (8 parts of water to 1 part of fumed silica by weight). CFDRC also mixed 8.25:1, 8.5:1, and 9:1 silica gels so that the effects of silica concentration could be evaluated. These are denoted Gel 8, Gel 8.25, Gel 8.5, and Gel 9, respectively.

2.3 Rheology of Fumed Silica Gels

Rheological studies on samples of aqueous fumed silica gels prepared with Cabot CAB-O-SIL M-5 silica were carried out. A complete battery of rheometric tests of the fumed silica-water gels was conducted. The rheology of the gels showed an apparent yield stress of several hundred Pascals and an elastic modulus of the order of 104 Pa; the breakdown strain of these materials, as well as the weaker gels prepared onsite, is of the order of 0.06.

Gel samples were also prepared at City College for the purpose of estimating the gel point of the fumed silica-water system. The two sets of samples are not directly comparable, however; a sample with a water-to-silica ratio of 9:1 prepared by this procedure formed a weaker gel than the 9:1 sample (Gel 9) prepared by CFDRC.

Some experiments were carried out in a controlled-stress rheometer (TA AR 1000) using 40 mm diameter parallel plates. As discussed below, the results show that the samples prepared by CFDRC are strong gels with elastic moduli of about 10,000 Pa and yield stresses of about 450 Pa (both values depending on concentration). The 16.6:1 water-to-silica gel seems to be very close to the point of incipient gelation.

Figure 4.1 shows the storage modulus (G') and loss modulus (G'') for Gel 9 as functions of frequency in the controlled stress rheometer. LVR data was taken after application of a slow steady shear of 0.02 / s for two and five minutes (total strains of 2.4 and 6) to Gel 9. The data for both moduli, G' and G'' , essentially superimpose after this pre-shear as seen in Figure 3.

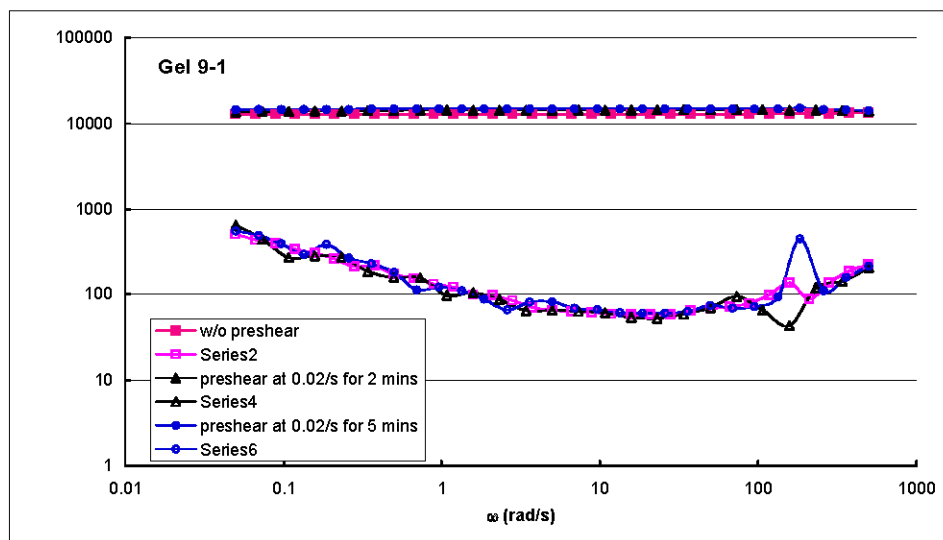


Figure 3: G' (filled symbols) and G'' (open symbols) for Gel 9 following the same loading procedure with an additional pre-shear at 0.02 /s for 2 and 5 minutes. The response is characteristic of a strong gel, with the elastic component (G') independent of frequency and more than an order of magnitude larger than the viscous component (G'').

The response is characteristic of a strong gel, with the elastic component (G') independent of frequency and more than an order of magnitude larger than the viscous component (G''). Strain was monitored and plotted as a function of time. Results are shown for Gel 8.5 in Figure 4.

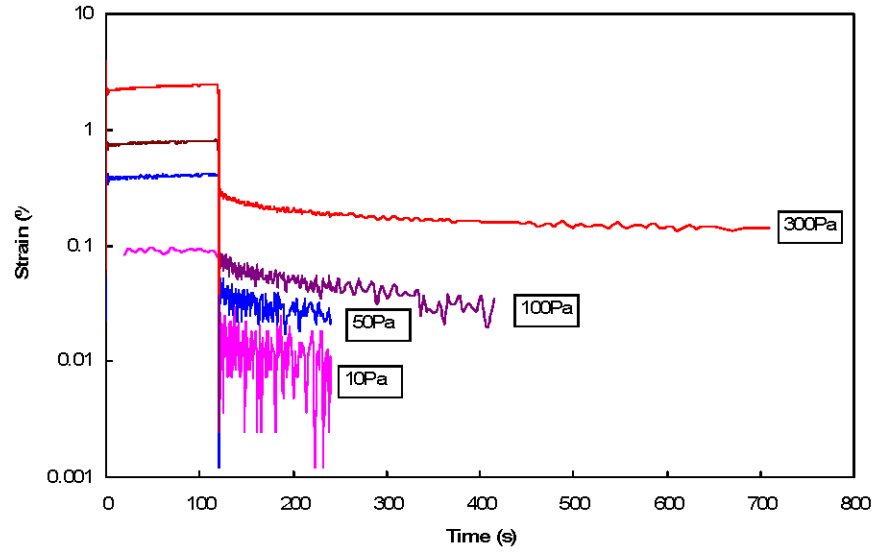


Figure 4: Step-stress and recovery curves at different imposed shear stresses, Gel 8.5.

Both G' and G'' decrease dramatically at higher strains, which is certainly due to breakdown of the gel structure (

Figure 5). Similar behavior is observed in Gels 8.25 and 8. The first deviation in G' from the low-strain limit occurs at a strain of about 4% for Gel 8.5; the modulus G' is 11,000 Pa, corresponding to a yield stress of 440 Pa. The high- and low-frequency asymptotes of G' intersect at a strain of 6.6%, which would give a yield stress of 720 Pa. The maximum in G'' occurs at a strain of 17%, corresponding to a yield stress of 1500 Pa based on the low-frequency asymptote of G' (G' and G'' are nearly equal at this strain, with a value of 340 Pa; the magnitude of the complex modulus $G^* = \sqrt{(G'^2 + G''^2)}$ is 470 Pa.). The corresponding values of the yield stress for Gel 9 are deviation from linearity, 260 Pa; intersection of asymptotes, 1500 Pa; and the maximum in G'' , 1700 Pa.

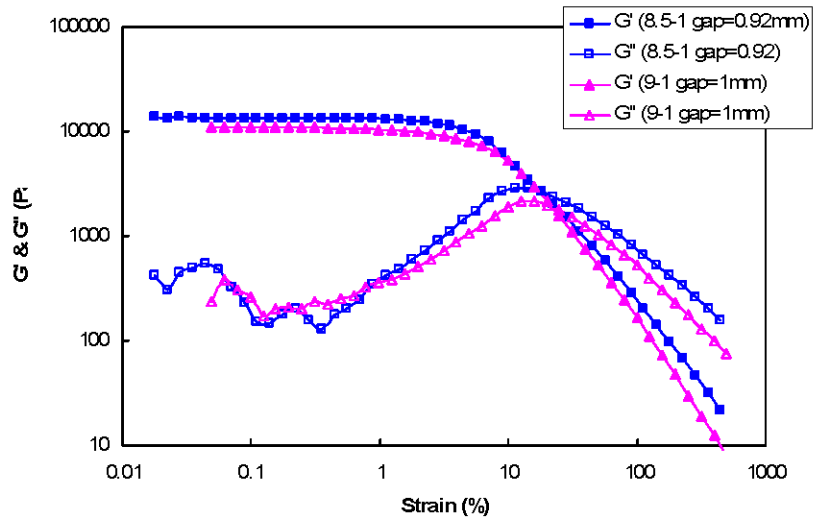


Figure 5: Linear moduli versus strain at a frequency of 1Hz for Gel 9 (triangles) and Gel 8 (squares).

The stress relaxation modulus $G(\gamma, t)$ following step strains of 0.5, 1, and 5% on the ARES rheometer is shown in Figure 6 for Gel 9. The data overlap for $\gamma = 0.5\%$ and 1%, establishing that 1% is within the linear range but 5% is not. This indicates that there are short-time processes acting on a separate length scale that affect the onset of nonlinearity; these are likely to involve rapid deformation of the equilibrium structure.

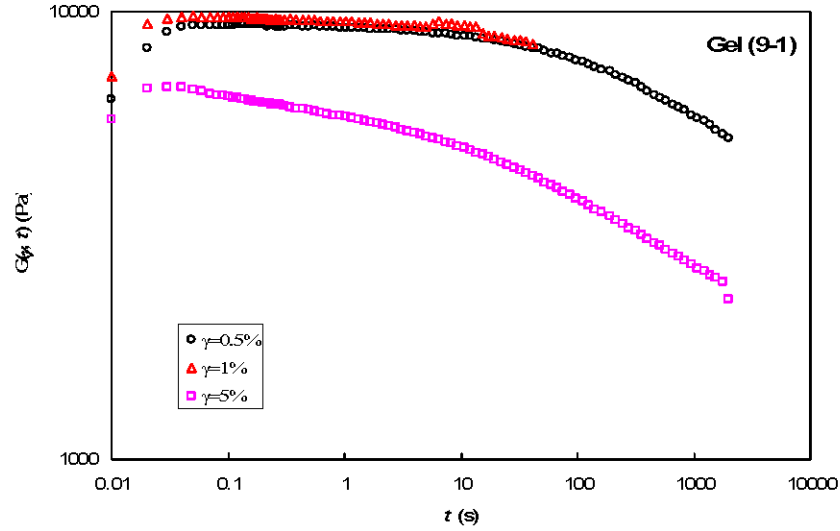


Figure 6: Relaxation modulus of Gel 9 as a function of time following step strains of 0.5 (circles), 1 (triangles) and 5% (squares).

The dynamic moduli of Gel 1B, a 14.7:1 water-to-silica ratio gel prepared at City College, are shown in Figure 7 at 1 Hz as functions of strain. The moduli are several orders of magnitude smaller than moduli for the 9:1 gel prepared by CFDRC (Figure 5). This is because the data presented are for lower solids content, as we sought to determine the gel point. Interestingly, the onset of nonlinearity occurs at roughly comparable strain levels in the weak gels and strong gels, suggesting that strain and not stress may be the critical variable defining failure.

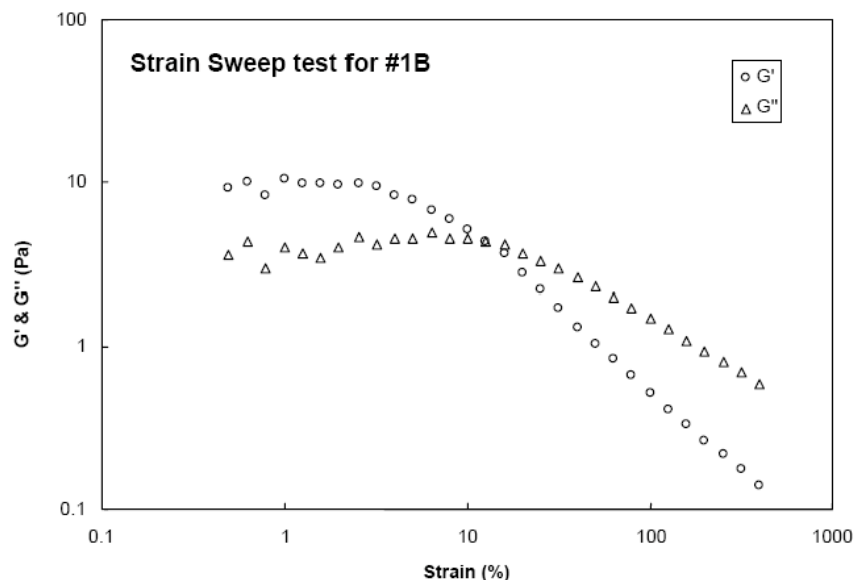


Figure 7: Storage (circles) and loss moduli (triangles) at 1 rad/s for Gel 1B versus strain.

G' and G'' for Gel 1C, 16.6:1 water-to-silica ratio, are plotted together in Figure 8. The moduli follow nearly parallel power-law behavior over the two decades of accessible frequency range. According to the criterion of Winter and Chambon (1986), this concentration is close to the incipient gel point.

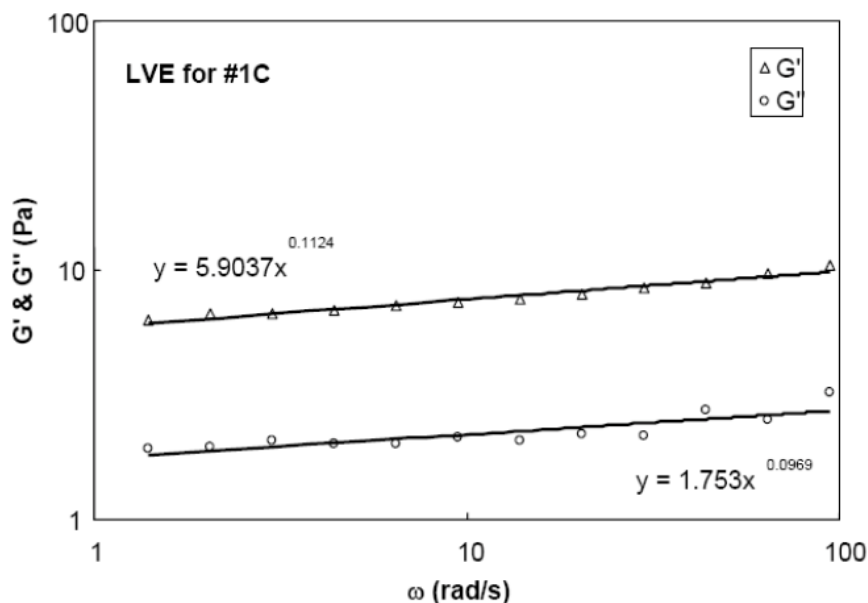


Figure 8: Storage and Loss Moduli of Gel 1C As Functions of Frequency.

2.4 Syneresis of Fumed Silica Gels

Experiments were conducted on water-based silica gels provided by CFDRC. A DuPont Sorvall RC 28S SUPRAspeed Centrifuge was used to measure the syneresis of water-based silica gels GEL 8, GEL 8.25 and GEL 8.5 provided by CFDRC over the range of

accelerations from 500 G to 30,000 G. Experiments were conducted at 20°C. As an example, photos presented in Figure 9 show a GEL 8 sample before and after the 30-min exposure to 5,500 G. We weighted the initial sample and the exudated water. Data on syneresis were then expressed in terms of the mass of exudated water as the fraction of the initial sample mass.

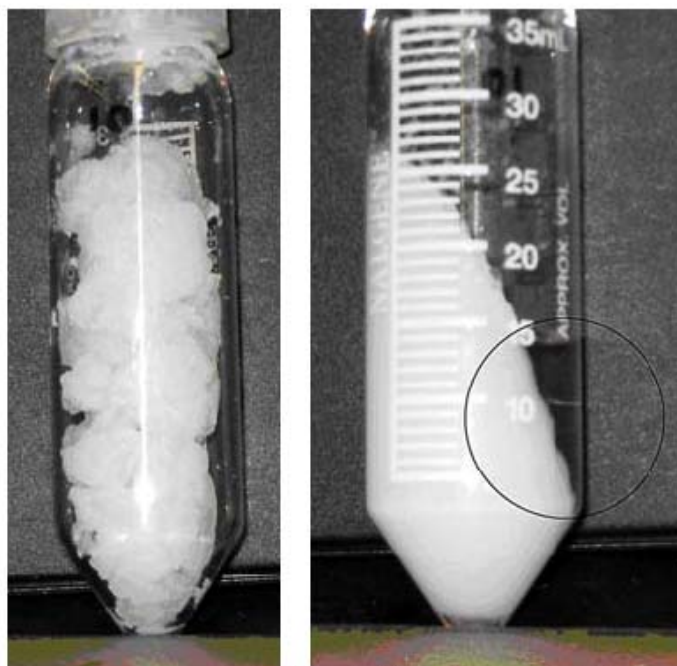


Figure 9: Photos of a GEL 8 sample before (left) and after (right) the 90-min exposure to 5,500 G at 20°C. The circle indicates the location of water exudated from the gel.

Plots in Figure 10 show the dependence of the amount of exudated water as the fraction of the initial sample mass, y , on the magnitude of the acceleration following the 30-min exposure. The extrapolation of logarithmic fitted curves to $y = 0$ indicates that the syneresis would start at the acceleration of about 2226 G for GEL 8, 590 G for GEL 8.25, and 526 G for GEL 8.5.

Plots in Figure 11 show the syneresis of GEL 8 as a function of the exposure time for the accelerations 5,500 G, 15,500 G, and 23,500 G. For comparison, we also measured the time dependence of syneresis of GEL 8.25 and GEL 8.5 for the acceleration of 5,500G by varying the exposure time from 1 min to 30 min. The mass fraction of water exudated from GEL 8 during the 90-min exposure to 1,500 G was found to be about 0.28%. Plots in Figure 12 present data on syneresis of GEL 8, GEL 8.25 and GEL 8.5 for the acceleration of 5,500G.

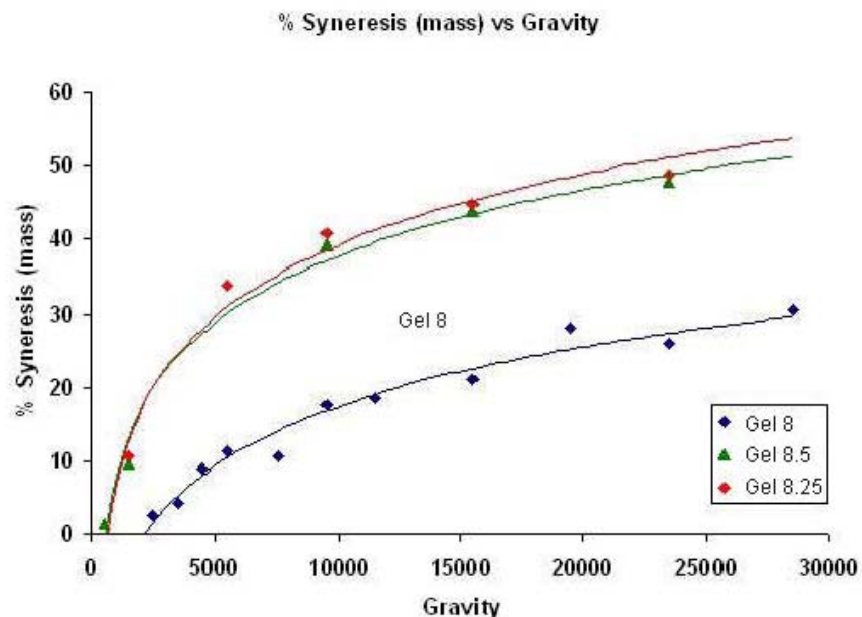


Figure 10: Syneresis of silica gels GEL 8, GEL 8.25 and GEL 8.5 for 200C following the 30-min exposure to acceleration (in G). The amount of exudated water is given as the fraction of the initial sample mass.

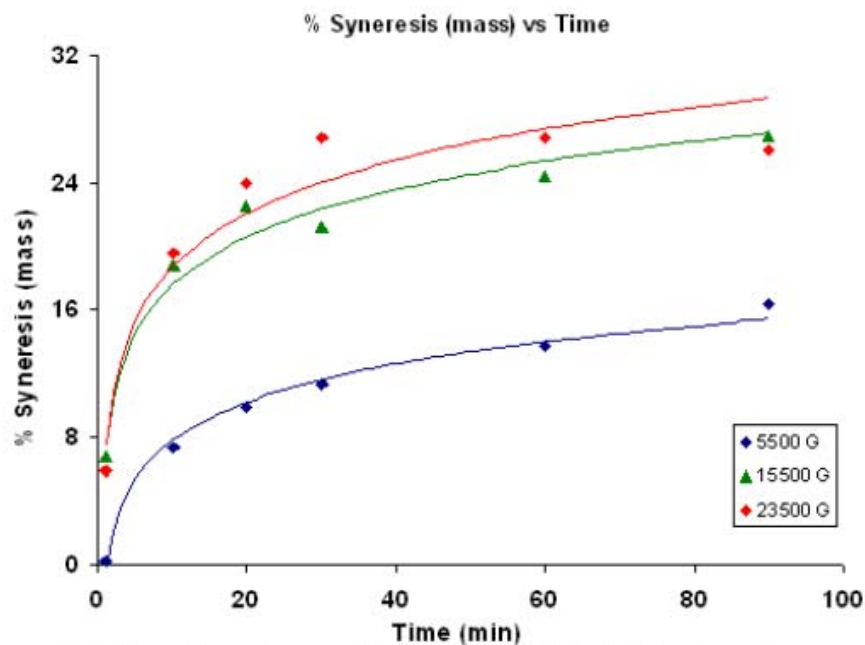


Figure 11: Time dependence of syneresis of GEL 8 following the exposure to acceleration for 20oC.

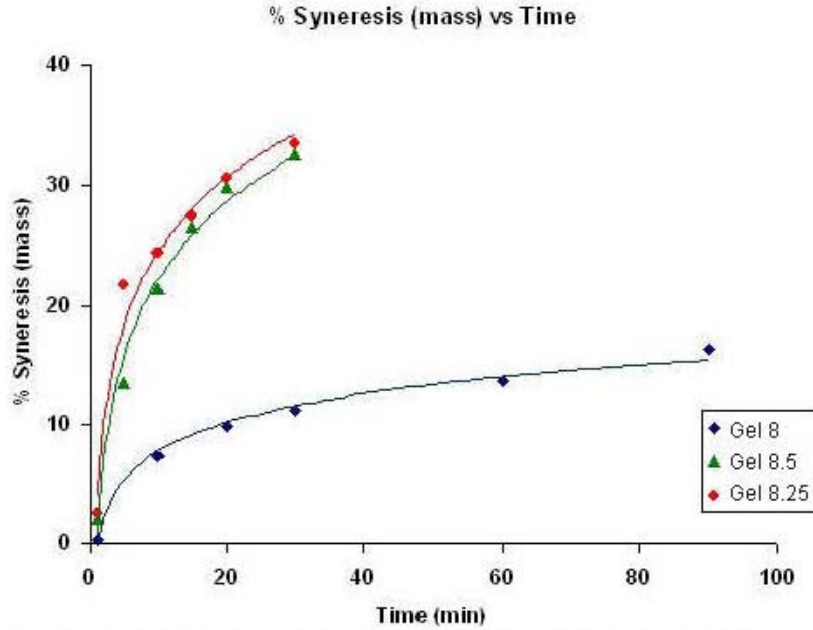


Figure 12: Time dependence of syneresis of GEL 8, GEL 8.25 and GEL 8.5 following the exposure to acceleration of 5,500G for 20oC.

To visualize the network formed by silica particles in a water-based silica gel, we removed water using the supercritical extraction process in liquid carbon dioxide [Taylor (1996)]. The water and CO₂ are fully miscible under these conditions, so that the water-CO₂ surface tension is zero. Thus capillary forces that would collapse the pores and rearrange the particles during the water extraction are avoided.

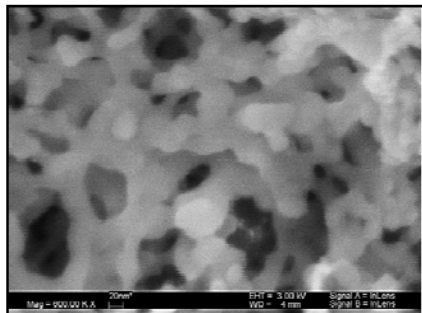
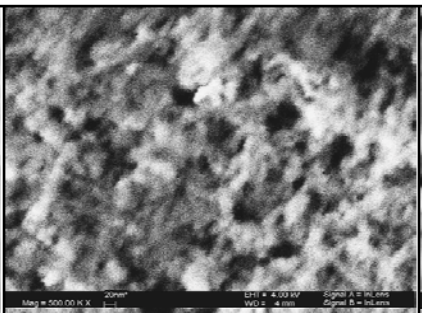
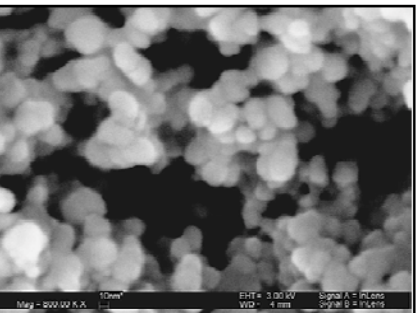
Experiments were conducted on samples of gels GEL 8, GEL 8.25 and GEL 8.5. Table 1 summarizes the data. The reproducibility of measurements was studied by repeating experiments (denoted as Run 1 and 2 in Table 1) and quantifying several SEM images taken from the same sample.

Gel	Sample No	Void shape factor	Mean void diameter, nm	Area fraction of voids
GEL 8	<i>Run 1</i>	0.66	86.29	0.434
GEL 8.25	<i>Run 1</i>	0.71	98.72	0.592
		0.64	92.86	0.625
	<i>Run 2</i>	0.68	95.32	0.601
GEL 8.5	<i>Run 1</i>	0.54	171.22	0.617
		0.62	154.22	0.585
	<i>Run 2</i>	0.41	150.10	0.641
GEL 8 30-min exposed to 11,500 G at 20 ^o C; syneresis 33.12(v/v)%	<i>Run 1</i>	0.68	74.25	0.144
		0.69	80.88	0.176
	<i>Run 2</i>	0.64	63.46	0.132
		0.68	73.80	0.159

Table 1: Characteristics of structures formed by silica particles

The SEM image in Figure 13 shows the network structure formed by silica particles in GEL 8. The surface fraction of pores and the mean diameter of pores are found to be about 43% and 86 nm, respectively (Table 1.1). The SEM images presented in Figures 14 and 15 show structures formed by silica particles in samples GEL 8.25 and GEL 8.5 revealed by the supercritical extraction of water. The surface fractions and the mean diameter of pores in these samples are found to be about 59-62% and 95-99 nm for GEL 8.25 and 58-64% and 150-171 nm for GEL 8.5 (Table 1.1). This explains why these samples being subjected to centrifuging lose water faster than GEL 8. (Figures. 10 and 12).

The bulk density of the structure formed by silica particles after the supercritical extraction of water from the inline filter loaded with a GEL 8 sample was found to be 527.76 kg/m³. Also, we attempted to characterize the rearrangement of silica particles caused by centrifuging a gel. The mass of water exudated under these conditions constituted about 16.2% of the initial mass of the sample. The SEM images presented in Figure 13 reveal structures formed by the silica particles as-received and exposed to centrifuging.

		
<p><i>The SEM image of the structure formed by particles in GEL 8 revealed by supercritical extraction of water in liquid carbon dioxide.</i></p>	<p><i>The SEM image of the structure formed by particles in GEL 8.25 revealed by supercritical extraction of water in liquid carbon dioxide.</i></p>	<p><i>The SEM image of the structure formed by particles in GEL 8.5 revealed by supercritical extraction of water in liquid carbon dioxide.</i></p>
<p><i>Figure 13</i></p>	<p><i>Figure 14</i></p>	<p><i>Figure 15</i></p>

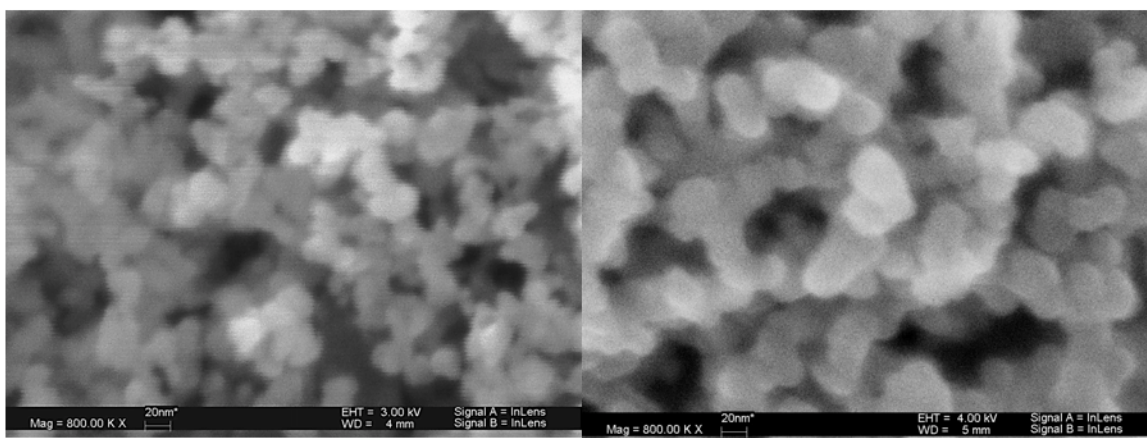


Figure 16: The SEM images of structures formed by particles in GEL 8 revealed by supercritical extraction of water: (left) as-received; (right) following the 30-min exposure to 11,500 G at 200C, syneresis 33.12 (v/v) %.

We employed nuclear magnetic resonance (NMR) spectroscopy to probe the interaction of water molecules with silica particles [Clifford, 1968; Zimmerman, 1957]. Water molecules are dynamically exchanged between an environment in which they relax slowly (free water) and one in which they relax rapidly (bound water). Under conditions of rapid exchange between free water and bound water on the NMR time scale, a single relaxation rate is observed, which represents the weighted average of the individual rate for each environment. We used ^{17}O nuclear magnetic relaxation to probe the mobility of water molecules in silica gels. For comparison, Oxygen-17 NMR measurements were carried out for an empty glass tube, a tube filled with D_2O up to 2 inches of height, a tube loaded with D_2O and 8 wt/wt % silica powder, and a tube loaded with D_2O mixed with GEL 8. The chemical shift (relative delta in resonance frequency reported in ppm)¹ of the ^{17}O resonance peak appears to be about 3.5 ppm for D_2O , 3.7 ppm for D_2O with silica powder, and 4.7 ppm for D_2O with GEL 8, as shown in Figure 17. These preliminary results indicate that NMR relaxation can be employed to characterize the interactions of solvent molecules with particles in silica-based gels.

¹ $\delta = (\nu - \nu_{\text{REF}}) \times 10^6 / \nu_{\text{REF}}$

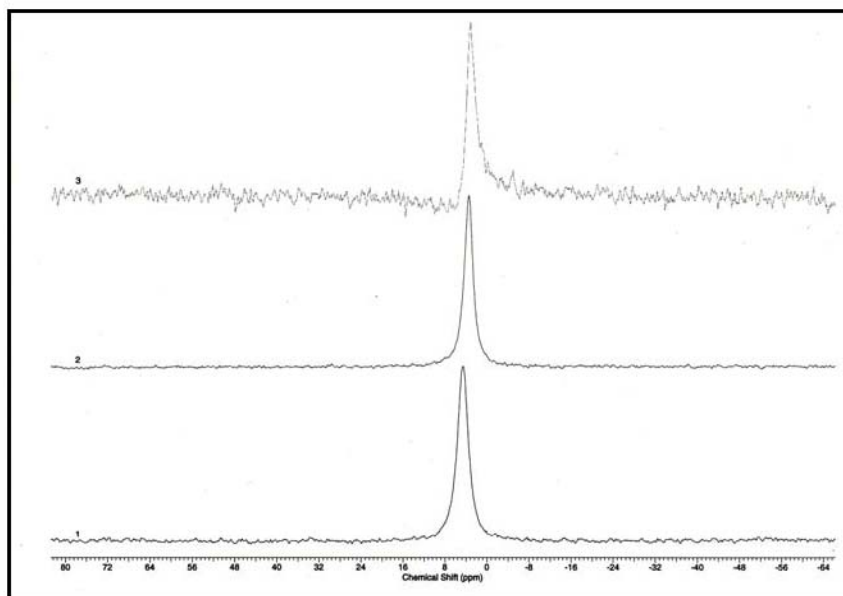


Figure 17: Oxygen-17 NMR resonance peaks for (1) D₂O, (2) D₂O with Degussa A200 silica powder, and (3) D₂O with GEL 8.

2.5 Molecular Level Modeling and Simulations

As experimental data were available for adsorption of water on silica, this system was used as a test to validate quantum mechanical and simulation methods that will be used in Phase II for propellant (IRFNA, MMA and DMAZ) + fumed silica systems. The procedure to be used for those systems is the one described here for the aqueous fumed silica systems. The force field for aqueous fumed silica gels was developed and validated using GCMC (Grand Canonical Monte Carlo) simulation to predict water adsorption on a silica nanoparticle. The tasks completed in Phase I included: (1) a search of the literature for the suitable interaction potentials to describe SiO₂ and water interactions; (2) an evaluation of the of the SiO₂-SiO₂ interaction potential by Pereira et al.(1999) and van Beest et al.(1990) that have been published; and (3) development of an SiO₂ + water interaction potential as this was not available in the literature. The interaction energy between atoms in the SiO₂ force fields is of the form:

$$U(r_{ij}) = A_{ij} e^{-b_{ij} r_{ij}} - \frac{c_{ij}}{r_{ij}} + \frac{q_i q_j}{r_{ij}}$$

where $U(r_{ij})$ is the potential energy between atoms i and j . A , b and C are parameters, q is the charge. We use this potential for each atom in SiO₂. We have used the extended simple point charge (SPCE) model [Berendsen, 1987] for water, as this model accurately represents the phase envelope (density versus temperature) of water when used in simulation.

We developed a force field for SiO₂ + water (cross interaction) using computational quantum mechanics. The interaction between the solid SiO₂ and H₂O was calculated

using the model clusters for SiO_2 , $\text{Si}(\text{OH})_4$, $\text{Si}_2\text{O}(\text{OH})_6$, $\text{Si}_3\text{O}_3(\text{OH})_6$, and $\text{Si}_4\text{O}_4(\text{OH})_8$ as shown in Figure 18.

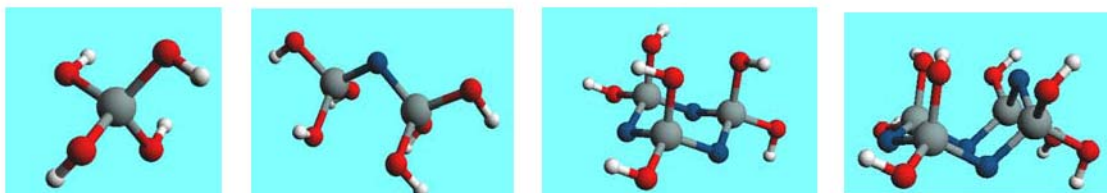


Figure 18: Four different structures of silicon clusters. The red atoms are terminal oxygen atoms (only bound to 1 Si atom), the blue atoms are bridging oxygen atoms (bound to two Si atoms) and the grey atoms are silicon atoms.

The electrostatic potential energy surface for the above isolated clusters was obtained from quantum mechanical calculations. The charges on each of the atoms of SiO_2 were determined by fitting point charges at each atomic center to this electrostatic potential energy surface. The interaction energies of each of these SiO_2 clusters and a water molecule were then calculated as a function of the distance between the centers of mass of the molecules at different relative orientations of the SiO_2 cluster and the water molecule. The interaction energies obtained are shown in Figure 19.

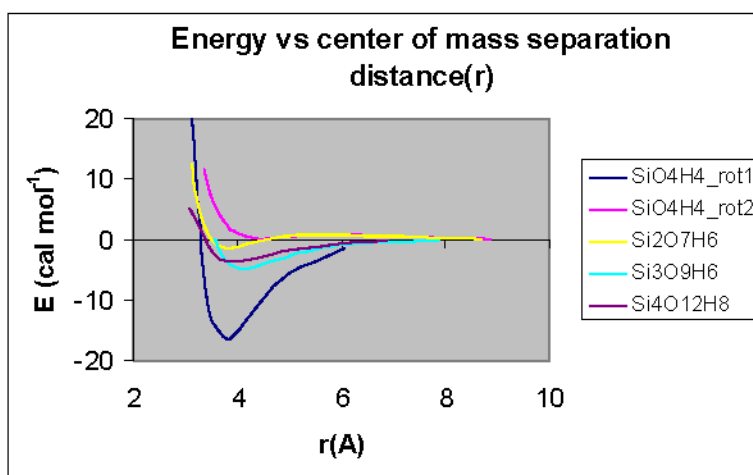


Figure 19: Calculated energies of the various molecular arrangements of SiO_2 cluster and water as a function of center-of-mass separation distance

The calculated quantum mechanical energies were then used to parameterize the force field for the interaction of water and various SiO_2 clusters used in simulation.

Experimental data on the adsorption of water on silica powders (fumed silica) were measured by Meyer and Hackerman (1966). We used this data to test the force field that we have developed by comparison with results from Grand Canonical Monte Carlo simulations of the adsorption of water on a 4 nm silica nanoparticle in an 8 nm simulation box. Figure 20 contains snapshots of such simulations at low and high relative humidity. The model particle we have used in simulation was obtained by computer annealing of a

spherical particle in a molecular dynamics simulation with the force field by Van Beest (1990).

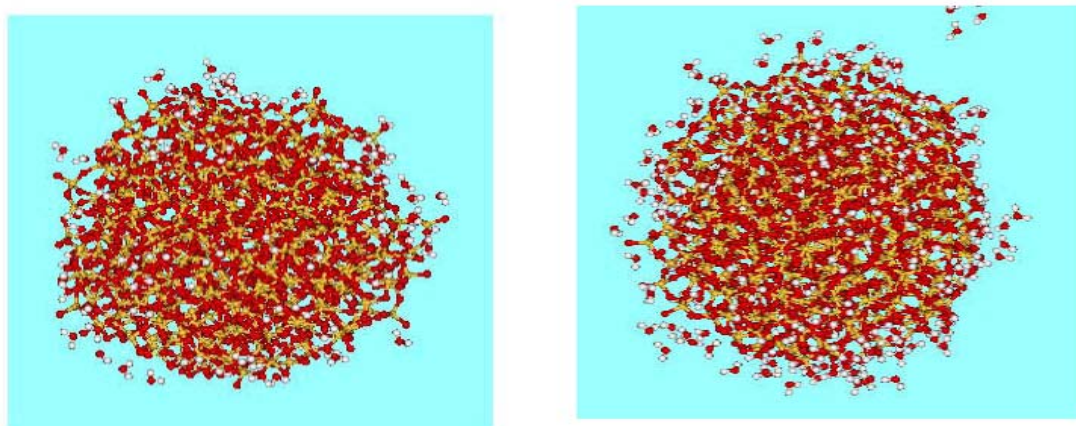


Figure 20: Snapshot of of final configurations a silica particle with water adsorbed to its surface at low and high relative humidities, respectively.

Figure 21 is a comparison of the adsorption isotherm from simulations using the force field we developed together with the available experimental data at 25°C. The simulations were run a two different relative humidities P/P_0 (where P_0 is the vapor pressure of pure water). The agreement with experiment is very good.

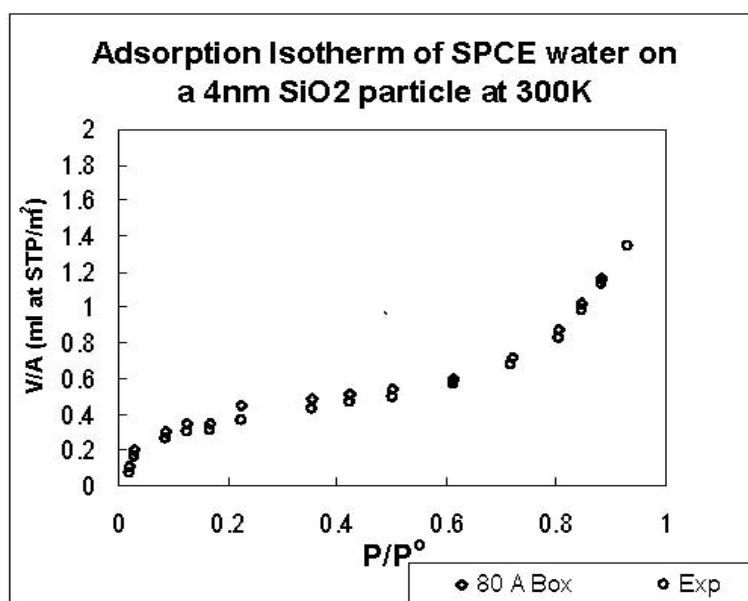


Figure 21: Adsorption isotherm for the adsorption of water onto the surface of a silica particle at 300 K compared to the experimental data [Meyer, 1966].

2.6 Particle Scale Models and Simulation

We have established a capability to simulate strongly attractive spherical particles in viscous liquids. Using heuristic but reasonable criteria based on closeness of particle

pairs to be termed “connected,” we have determined conditions resulting in fully connected structures, a condition needed for support of a shearing force without flow. We employ simulations that may incorporate hydrodynamic interactions (*HI*) through a Newtonian liquid, and that account for inter-particle forces expressible as a gradient of a pair-particle interaction potential (and thus dependent on knowledge of particle positions only).

Note that accounting for HI implies that the motion of one particle influences neighboring particle motions (and is a many-body problem dependent on instantaneous positions), whereas a simple drag that is independent of interaction hydrodynamics is a single-body problem. Based on the solid understanding of this condition for attractive particles, we have focused on development of the Stokesian Dynamics algorithm, implemented in standard and accelerated (Sierou and Brady 2001) form, for strongly attractive conditions. We are not aware of prior use of the method for particles with strongly attractive spherically symmetric potentials.

All of the potentials considered have a continuous force, unlike the square-well potential that is used in some studies (Foffi *et al.* 2005). This is illustrated for two forms of potential in Figure 22.

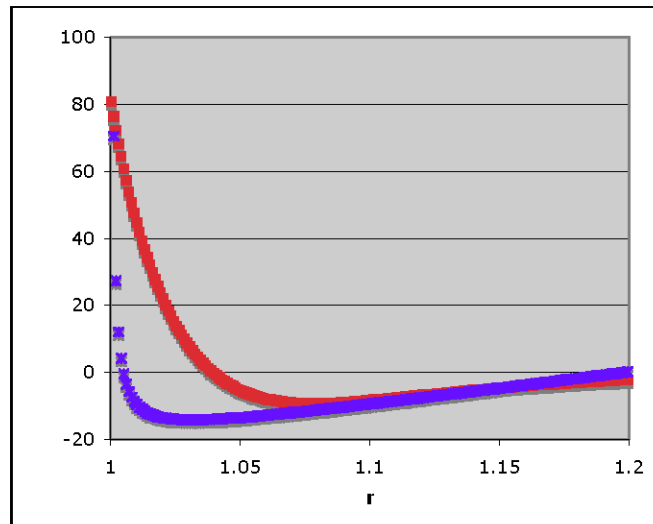


Figure 22: Examples of interparticle force forms employed, plotted as a function of r , with $r=1$ being particle contact. The squares denote a potential with a generalized Lennard-Jones (of 36–18 form) soft-core potential and minimum of $V/kT = -9.5$ at $r = 1.07$, while the crosses show a combined steeply repulsive hard-core potential near $r=1$ with a linear attraction out to $r=1.2$.

Successful simulation with these and other potentials has been demonstrated. In order to probe the microscale basis of the rheology of the gelled state in attractive colloids, we have developed forms with well-defined separation of inflection in the attractive portion from the energy minimum, and forms such as the linear attraction in which the inflection can be made arbitrarily close to the minimum.

We find that strong attraction, with $V > 5$ kT, results in structural development similar to that reported in Foffi et al (2005) for Brownian dynamics simulations. The energy function used is the combined form discussed above and illustrated in Figure 23 with minimum of 9.5 kT. In simulations in three dimensions, we have gone to 1000 particles.

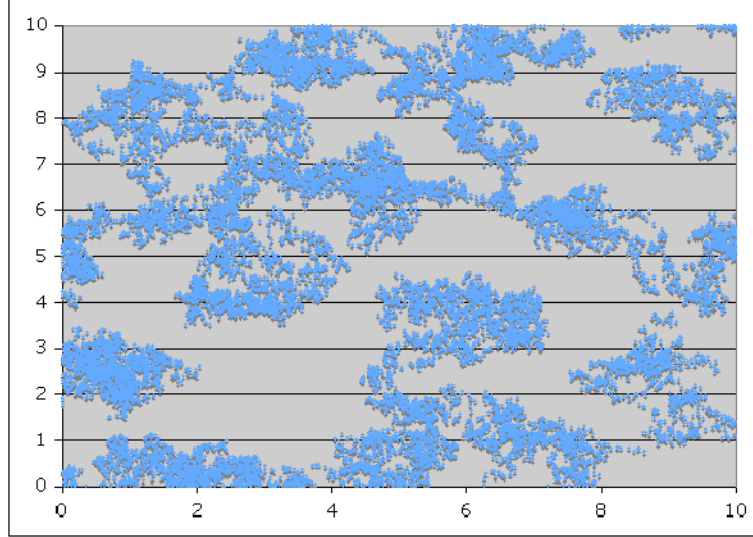


Figure 23: Plot of particle positions after 100 Brownian diffusion times ($100a^2/D_0$) showing clustering in a 15% by area dispersion with strong attraction.

An issue that was proposed for study was the role of shear in setting structure, and we have demonstrated using small systems (less than 100 particles) at larger fractions that the local structures generated can be affected by even a relatively weak shear, see Figure 24.

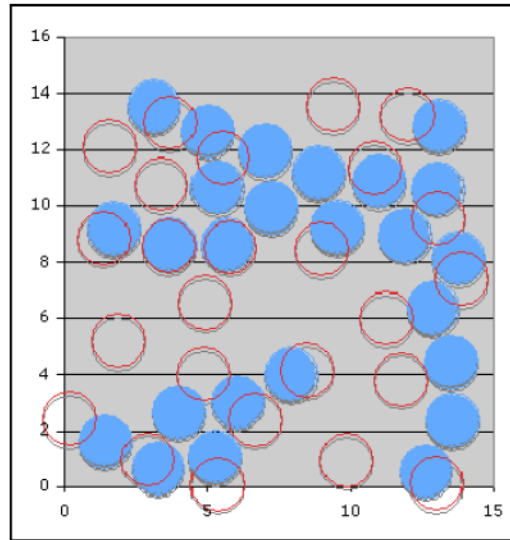


Figure 24: Full symbols show structure in unit cell of a small two-dimensional attractive particle simulation, with minimum energy of -3 kT at $r/a = 2.05$, for Peclet number of $Pe = 0.1$ ($Pe = \gamma a^2/D_0$ where γ is the shear rate) after a strain of 10.

3 . PHASE II TECHNICAL OBJECTIVES AND ACCOMPLISHMENTS

3.1 Objectives of the Phase II study

The overall objective of this project was to develop Quantitative Structure-Property Relationships (QSPR) for the prediction, synthesis, and optimization of gelled propellant formulations. The specific objectives of the Phase II effort were:

1. Prepare a number of gels of various solvent types and silica contents
2. Create an extensive gel property database, including the following measured properties of 1:
 - a. Density (CFDRC)
 - b. Modulus of elasticity (CFDRC)
 - c. 50-caliber test (CFDRC)
 - d. Syneresis (NJIT)
 - e. Yield stress and loss / storage modulus (CCNY)
3. Develop a QSPR model (neural network) to predict future gel properties from those already observed in the database
4. Create a Graphical User Interface (GUI) for the QSPR model to facilitate algorithm usage and database management
5. Continue efforts, from Phase I, to model the structural formation of gels through Brownian / Stokesian dynamics
6. Study the dynamics of gelation through Dynamic Light Scattering (DLS) and time dependent rheology

3.2 Summary of the Phase II accomplishments

The objectives of the Phase II study were successfully accomplished. These accomplishments can be summarized as follows:

1. *Gel mixing*

Mixing techniques were established for the preparation of organic-based gels. Over 39 different gels were then prepared and tested. Consistency error estimates were determined for various preparation uncertainties, which were shown to be negligible (below measurement uncertainty).

2. *Gel property database*

Measurement techniques were established and perfected over the course of the Phase II project. Gel properties were measured to form a training and validation database for the QSPR model. The database now contains 23 different organic entries from gels created with 9% silica and 16 entries from gels created with 11% silica.

3. *OSPR-Neural Network Development*

A feed-forward / back propagation neural network was created to predict properties of new gel formulations from those observed in the gel database. The algorithm was demonstrated with excellent results over the relatively limited training dataset (in terms of typical neural network training). Suggestions were

offered and demonstrated to deal with issues arising from limited amounts of training data, which show substantial possibilities to improve network predictability.

4. *Graphical User Interface (GUI) Development*

A GUI was developed for the QSPR model in Python programming language, which is platform independent. The GUI facilitates algorithm usage and database management.

5. *Brownian / Stokesian gelation dynamics model*

The inter-particle force potential was established and demonstrated for aqueous colloidal silica dispersions. A procedure for simulating larger systems faster and without much loss in accuracy was selected (11).

6. *Dynamic gelation measurements*

Both DLS and rotational rheometry were used to study the formation of aqueous gels. DLS provided insight into the structural evolution of gels, while rotational rheometry explored their mechanical evolution. These measurements were used to determine the onset of gelation and compared quite well.

Phase II efforts have successfully produced a validated QSPR (neural network) model capable of making accurate gel predictions in a user friendly way. Details of the work performed during the Phase II project are presented in detail in the following sections.

4. TECHNICAL APPROACH

4.1 Measurement Procedures

The workload of preparing and testing the gels was divided between each of the participating contractors. The following sections describe the experimental procedures that were utilized. Each organization's responsibilities are outlined below:

- **CFDRC**
 - Gel Mixing
 - Density
 - Modulus of Elasticity
 - 50-caliber Test
- **NJIT**
 - Syneresis
 - Extrusion and Drop Formation
 - Evaporation
- **CCNY**
 - Rotational Rheometry
 - Gelation Dynamics

4.1.1 Density

Gel densities were measured with a 10.49-ml Fisher Scientific pycnometer and a Mettler-Toledo Analytical Balance (see Figure 25). The total estimated uncertainty (instrument + operator variability) in measured density was less than $\pm 1\%$. In addition, measurements were made by CFDRC in Huntsville AL, where the samples were prepared. Consequently, the gels did not incur significant degradation due to long storage times.

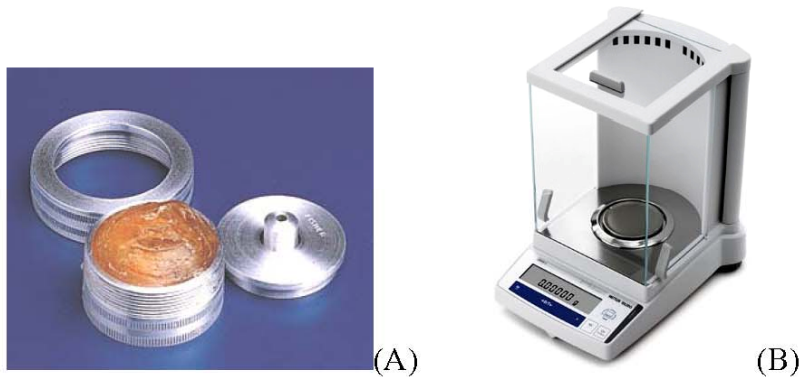


Figure 25: (A) Fisher Scientific Pycnometer, and (B) Digital Precision Balance Used to Determine Gel Density

4.1.2 50 Caliber Test

The 50-caliber test was based on specifications sent by Scott Michaels (AMRDEC). A gel fails the test if it will flow through a $\frac{1}{2}$ -inch hole with a head height of 7 inches; otherwise the gel passes. The intent of the test is to simulate a ruptured Hellfire sized missile lying on its side.

Initially, CFDRC prepared gels with 9% silica content by weight. Nearly all of these gels failed the 50-caliber test. The silica content was then raised to 11%, resulting in a substantial pass-rate improvement. Table 2 summarizes the results of the 50-caliber test.

Table 2: Summary of 50-Caliber Test Results Showing a Much Improved Pass Rate in the 11% Data Over the 9% Data

Solvent	9% Silica	
iso-Pentane	Fail	
Heptane	Fail	
Octane	Fail	
iso-Octane	Fail	
CycloHexane	Fail	
Hexene	Fail	
Benzene	Fail	
Diethyl Amine	Pass	
n-PropylAmine	Fail	
Cyclohexene	Fail	11% Silica
n-Pentane	Fail	Pass
Hexane	Fail	Pass
Decane	Fail	Pass
MEK	Fail	Fail
Acetone	Fail	Fail
MIBK	Fail	Fail
Decanol	Fail	Fail
Methanol	Fail	Fail
NitroMethane	Pass	Pass
NitroProp	Fail	Pass
NitroEthane	Fail	Pass
Triethyl Amine	Pass	Pass
1-Propanol	Fail	Fail
Dibutyl Amine	Fail	Fail
1-Pentanol	Fail	Fail
n-ButylAmine	Fail	Fail

4.1.3 Modulus of Elasticity

The modulus of elasticity of solids and semi-solid materials can be calculated with the following formula

$$E = c^2 \cdot \rho$$

Where c is the speed of sound in the material and ρ is its density. For our gels the density was available from measurement (as described in Section 4.1.1). The speed of sound was found by measuring the time required for an ultrasonic pulse to travel a known distance through the gel. The apparatus to determine the speed of sound is shown in Figure 26.



Figure 26: Setup for Gel Sound Speed Measurements (1) DP 2000 Ultrasonic Doppler Velocimeter / Pulse Generator, (2) Tektronics TDS-210 Digital Oscilloscope, (3) Dial Caliper, (4) Gel Samples, (5) Ultrasonic Probe, and (6) Plexiglass Disk

During these measurements the gel was placed in a thin polyethylene bag (small sandwich bag) and set between the tip of the ultrasonic probe and a Plexiglass disc (precision machined for a smooth flat surfaces). An ultrasonic 8-MHz signal, emitted by a 5-mm diameter cylindrical probe, was coupled (acoustically) to the gel bag by a thin film of GE Ultrasonic Gel (also used to couple the bag to the Plexiglass disk). The speed of sound (c) was then calculated with:

$$c = \frac{2d}{\Delta t}$$

Where d is the distance between the tip of the ultrasonic probe to the Plexiglass disk and Δt is the time between the outgoing ultrasonic pulse and the reflection from the first Plexiglass surface. The sound speed uncertainty was on average $\pm 4\%$ of the recorded value, which includes error introduced by the wall thickness of the bag and operator errors made during reading the oscilloscope trace. In addition, the sound speed measurement of each gel sample included 10-12 repeated measurements at distances ranging from 0.2 to 0.7 in.

4.1.4 Syneresis

Samples of organic-based fumed silica gels were sent by CFDRC to the NJIT for syneresis testing (the complete set of syneresis data is located in Appendix B). A DuPont Sorvall RC 28@ SUPRAspeed centrifuge was used to induce syneresis in the gels over the range of accelerations from 500 to 30,000 G at 20 °C. Figure 27 shows an example of hexane silica gel both before and after a 30-min exposure to 10,000 G. As can be seen in the image on the right, solvent has been exudated from the sample through the collapse of the gel structure (i.e. reduced gel volume).

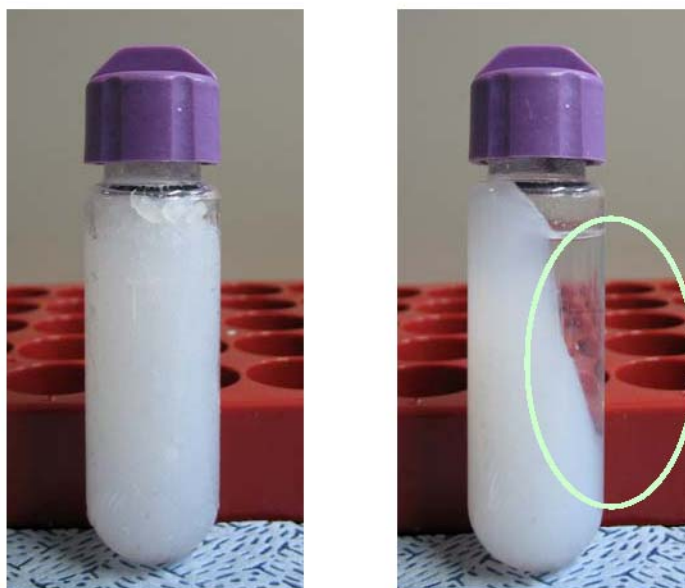


Figure 27: Photos of Hexane Silica Gel Before (left) and After (right) a 30-min Exposure to 10,000G at 20°C. The Circle Indicates the Location of Organic Solvent Exudated From the Sample.

Syneresis was expressed as the ratio of exudated solvent mass to initial sample mass. Measurement repeatability was established by duplicating experiments under typical operating conditions. Table 3 summarizes the consistency in duplicated measurements. It is noted that the greatest variation between experiments occurs at the smaller acceleration (500 G), due to a small value of exudated mass. It is also noted, that these values are not related to repeatability over long sample storage times, which will be addressed at the end of the Section.

Table 3: Reproducibility of Syneresis Measurements

Solvent	Operating Conditions			Syneresis, mass%		Variation, %
	Acceleration (G)	Temp (°C)	Time (min)	Run 1	Run 2	
Heptane	20,000	20	10	36	37	3.0
Decane	500	20	90	0.7	0.8	9.4
Decane	30,000	20	5	37	39	-3.7

In Phase I, the syneresis of water-based silica gels was found to be a strong function of the exposure time to acceleration. Conversely, the syneresis of organic-based gels did not demonstrate a strong dependence on exposure time at fixed accelerations (see Table 4 and Figure 28). Once subjected to centrifuging, an organic gel loses a certain amount of solvent very fast, but then retains the remaining amount of solvent.

Notice that some values in Table 4 show a re-absorption of the solvent (within the inherent measurement error). This may indicate a time dependent swelling of the

collapsed gel structure after the removal of acceleration (similar to a sponge). Consequently, residual swelling should be more pronounced under smaller accelerations, where a greater percentage of elasticity is recovered. It may be necessary to study this phenomenon further in order to reduce uncertainty.

Table 4: Syneresis of organic solvents gelled with 9 w/w% fumed silica following the exposure to 500G, 2,000G and 30,000G accelerations for 5 min and 90min at 20°C.

Gels (9% w/w silica)	Syneresis, mass %					
	500 G		2,000 G		30,000 G	
	5 min	90 min	5 min	90 min	5 min	90 min
Iso-Pentane	0.9	0.7	0.6	1.1	35.4	38.5
n-Pentane	0.3	0.4	0.4	0.6	30.0	29.1
Hexane	0.2	0.1	0.5	3.0	37.8	40.0
Heptane	0.1	0.1	3.3	5.2	35.7	40.0
Octane	0.1	0.1	6.8	8.4	38.2	42.6
Iso-Octane	1.7	1.5	12.4	11.5	41.6	46.7
Decane	0.7	0.7	9.7	9.9	36.9	42.8

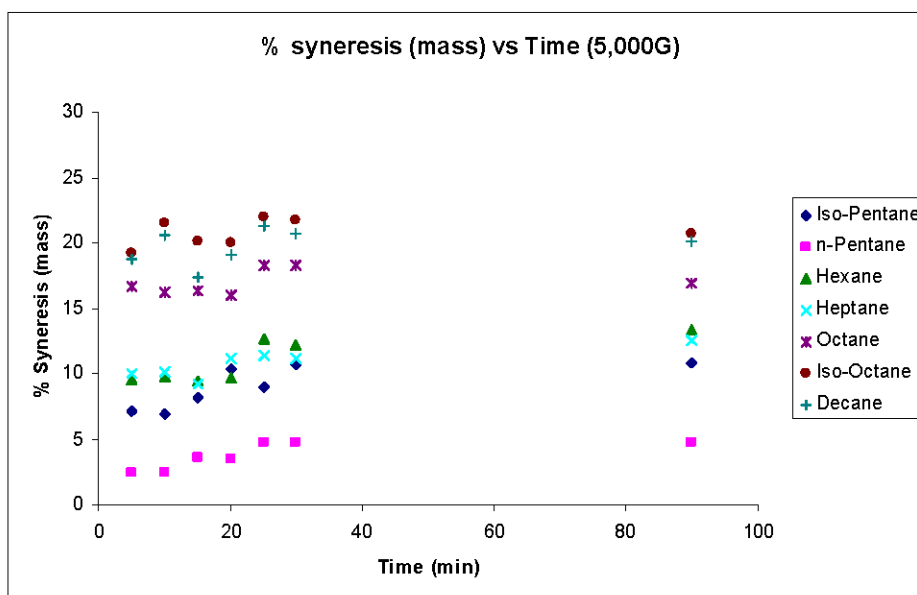


Figure 28: Time dependence of syneresis in organic solvents gelled with 9 w/w% fumed silica subjected to 5,000G acceleration at 20°C.

Similar to the water-based gels of Phase I (see Figure 30), the syneresis of organic-based gels showed strong dependence on acceleration rate. Figure 29 shows the syneresis of the alkanes following 5 and 10-minute exposures to various acceleration rates. The syneresis tends to taper off at high acceleration rates, indicating that the gel is approaching a limit of compression that cannot be recovered.

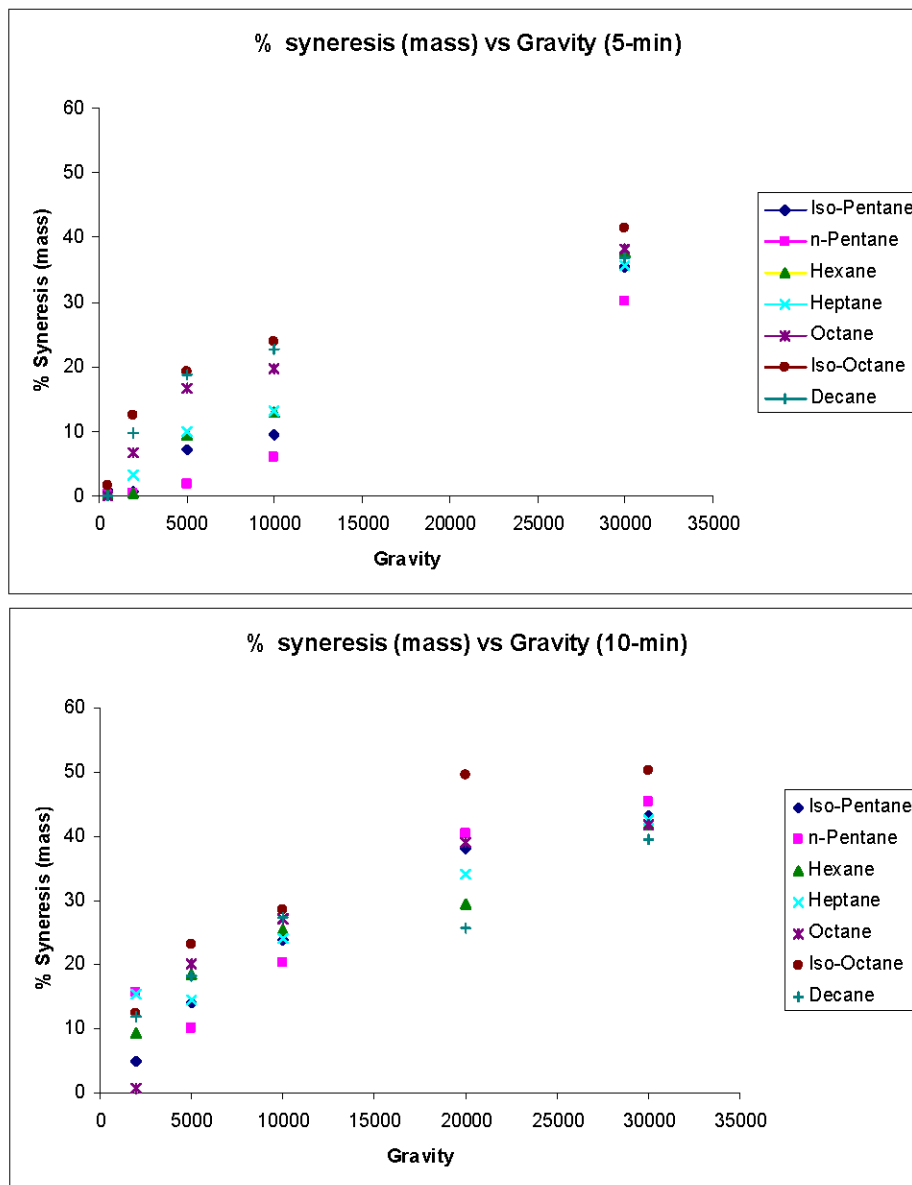


Figure 29: Syneresis of organic solvents (iso-pentane, n-pentane, hexane, heptane, octane, iso-octane, and decane) gelled with 9 w/w% fumed silica, following the 5 (top) and 10 (bottom) minute exposure to acceleration (in G) at 20°C.

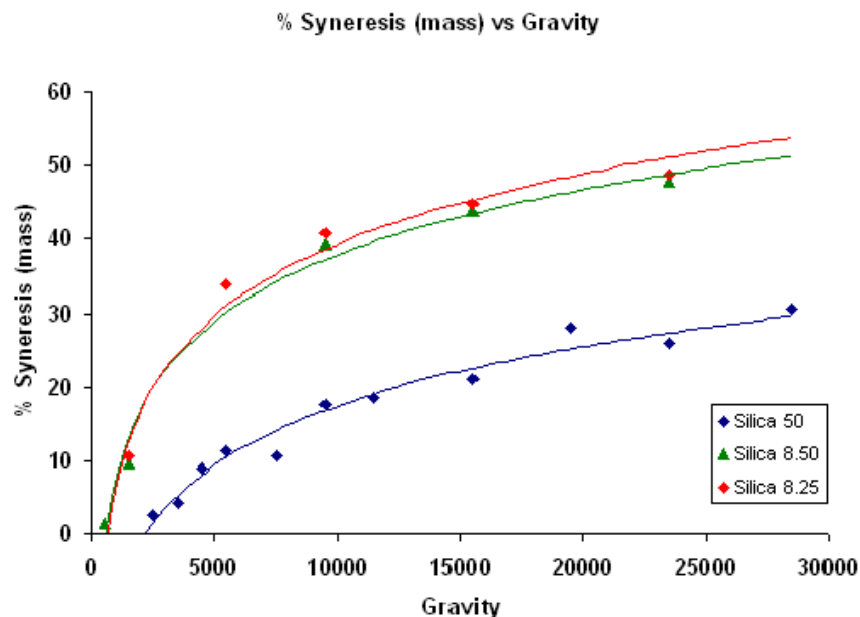


Figure 30: Syneresis of silica gels SILICA 50, SILICA 8.25 (8.25 parts of water to 1 part of fumed silica by weight) and SILICA 8.50 (8.50 parts of water to 1 part of fumed silica by weight) following the 30-min exposure to acceleration (in G) at 20°C. The amount of exudated water is given as the fraction of the initial sample mass. [7]

To reduce the 50-caliber failure rate, CFDRC increased the silica loading of the gels from 9 to 11%. The effect of this action on syneresis can be seen in Figure 31. It appears that syneresis decreases with increasing silica content. Also, MIBK demonstrated the highest reduction in syneresis.

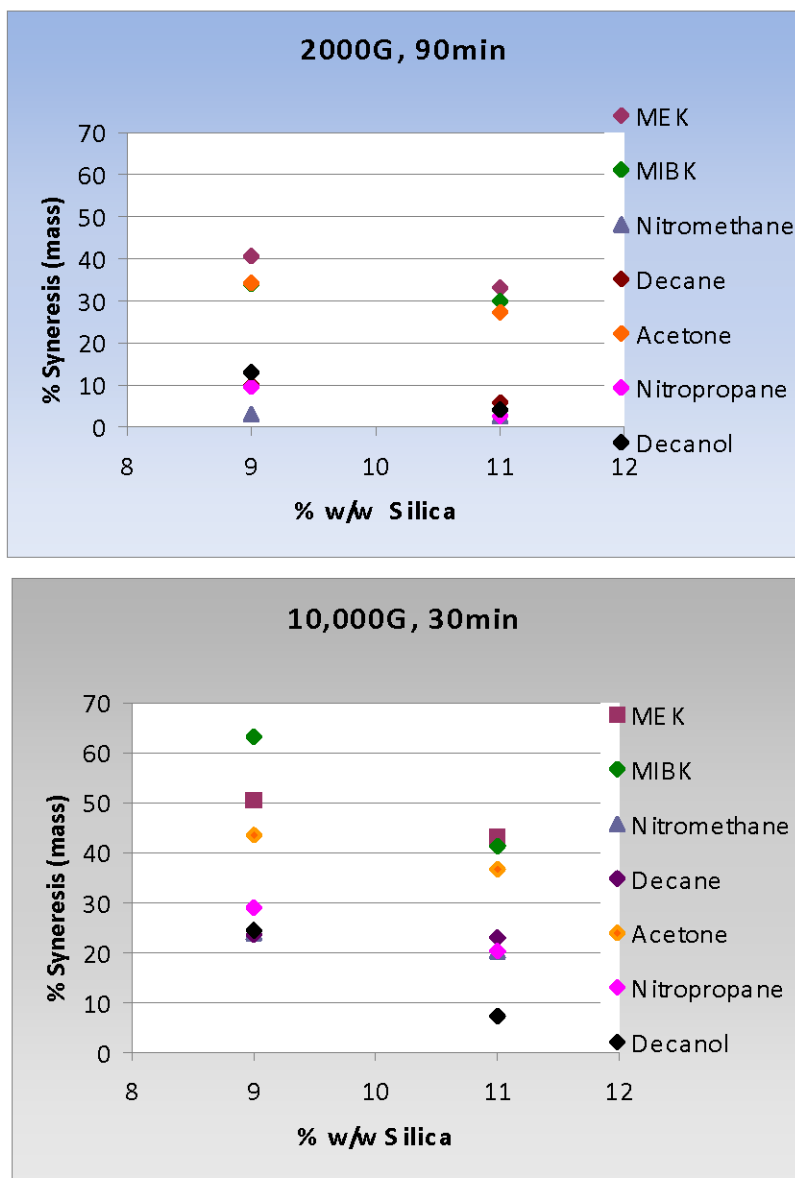


Figure 31: Syneresis of organic-based silica gels with 9 and 11% (w/w) silica following the exposure to acceleration 20,000 (top) and 10,000 (bottom) G for 30min at 20°C.

The data collected in Figure 31 was extracted from relatively fresh batches of gels on different test dates. Consequently, storage time had little effect on the results shown. The adverse effect of long sample storage times on syneresis repeatability is shown in Table 5. A reduction in syneresis with time is attributed to evaporation. Under evaporation, the collapsed gel volume will be similar, but the exposed solvent volume will not.

Table 5: Comparison of Syneresis after Long Storage Time (Decane)

Gels (9% silica w/w)	% Syneresis (mass) of 2,000G and 90min	
Decane	August 2007	March 2008
	9.86	6.35

4.1.5 Extrusion and Drop Formation

The jetting characteristics of CS gels were studied with the setup shown in Figure 32. Syringes 1 and 2 (both 10-ml with 16-mm barrel IDs) are coupled together by Tygon tubing, filled with oil to monitor the pressure acting on the piston rod of syringe 2. The piston rods of syringes 2 and 3 are directly connected together. Organic gel was loaded into syringe 3 (glass 5-ml with 11.6-mm barrel ID). It was necessary to use a glass syringe to hold the gel, since rubber piston seals would swell and eventually cause the piston to stall. Contrary, a glass syringe does not react with the organic-based gel and provides a relatively low friction between the piston rod and syringe barrel.

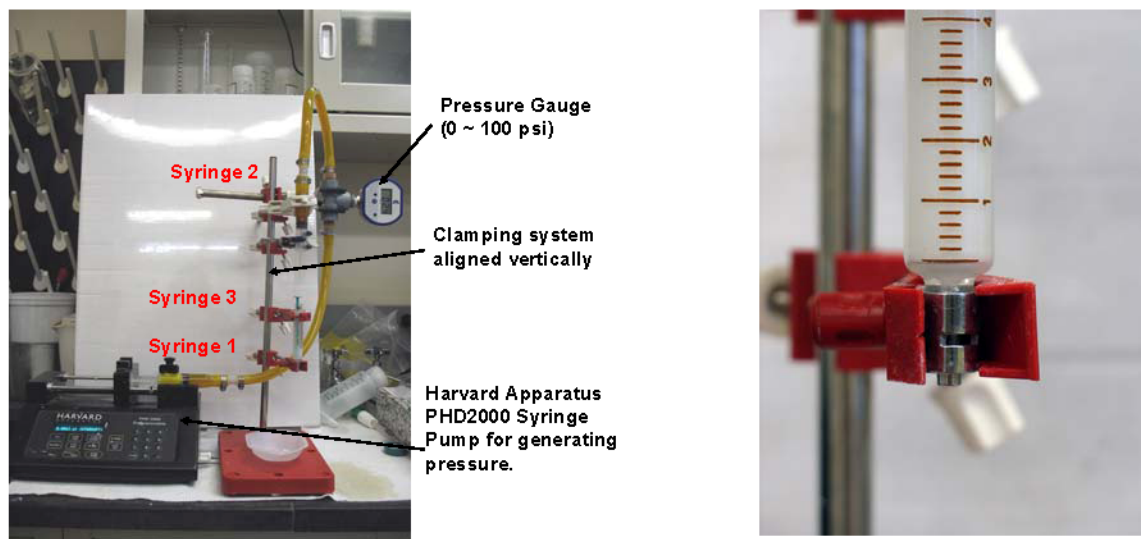


Figure 32: Gel Jetting Setup: (Left) Experimental setup for testing pressure driven syneresis (Right) Syringe 3 loaded with gel. (Volume: 5ml; barrel ID: 11.6 mm, nozzle ID: 2.0 mm, nozzle length: 17.0 mm)

The extrusion tests included two steps. First, a blank test (empty syringe 3) was conducted at the desired piston speed. This was done to measure the driving pressure due to friction in the setup (oil and piston seals). Next, syringe 3 was loaded with a gel and the test was conducted at the same piston speed as the blank case. The difference in pressure between the loaded and blank case was recorded as the driving pressure of the gel.

The setup was first used to study the flow of a hexane-based silica gel. Following the application of ~15 psi a solvent drop appeared from the nozzle (Figure 33). Solvent and CS particles slowly filled the pendant drop causing it to eventually detach from the nozzle. An increase of pressure (to ~26 psi) caused a transition from dripping to a column extrusion.



Figure 33: Pressure Driven Flow of a Hexane-based Gel Showing Drop Formation at 15 psi

Figure 34 shows the dripping (left) and jetting (right) action of a CS gel (4.7%) flowing through two different orifices at 400 ml/min. With a 250-micron diameter orifice (left), the gel drips out. With a 2-mm orifice at the same flow rate (right), the gel extrudes as a column. Notice the light regions in the figure, indicating the presence of silica.

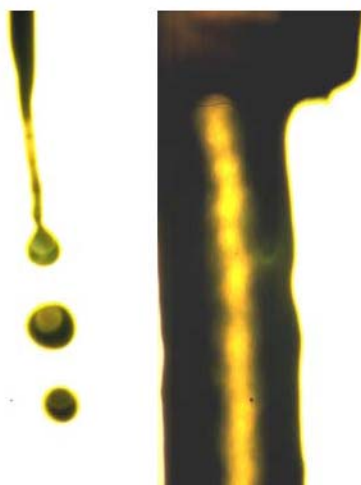


Figure 34: Extrusion and Drop Formation of a Colloidal Silica Gel (4.7%) at the Same Flow Rate Through a 250-micron (Left) and 2-mm (Right) Orifice

4.1.6 Gel Structure During Solvent Evaporation

Preliminary studies on the evolution of the gel structure during solvent evaporation were conducted on the NJIT fluorescence microscope system shown in Figure 35. The NIKON microscope is equipped with two fluorescence CCD cameras (a high-resolution CoolSNAP SQ2 and a high-speed Cascade 128+), a dual-view aperture imaging system, and a fluorescence illumination system EXFO X-Cite 120. The system allows the simultaneous recording of two types of fluorescent markers.

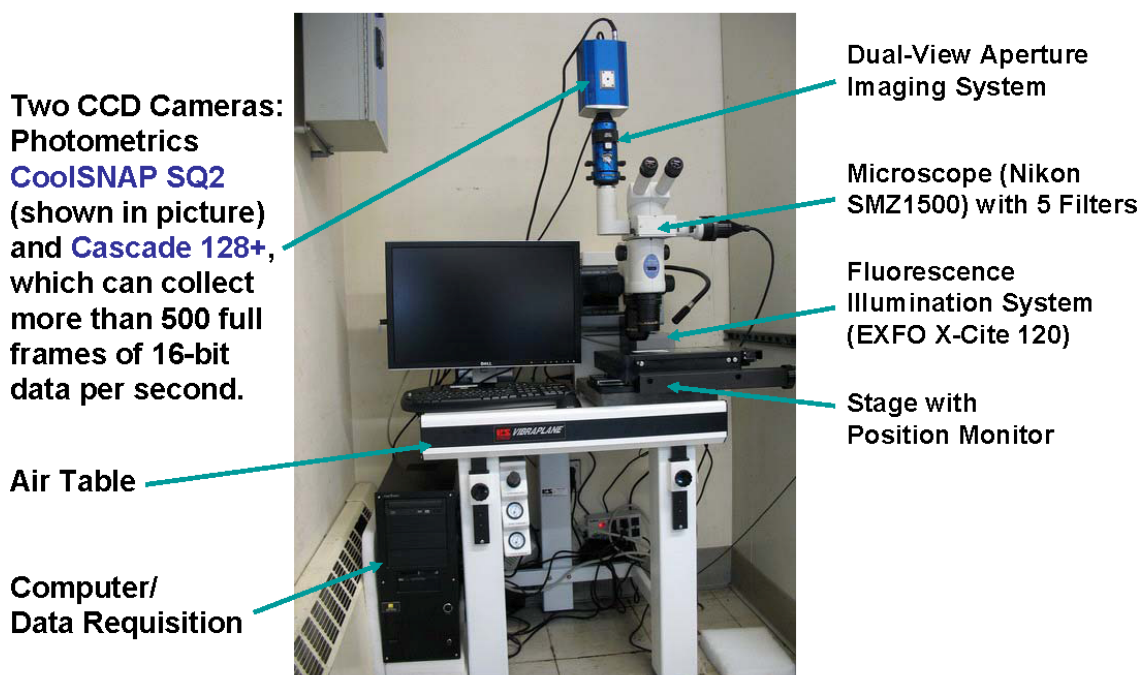


Figure 35: NIKON fluorescence microscope system used to study solvent evaporation

Figure 36 shows the structure transformations of a hexane-based silica gel during the evaporation of hexane. As the hexane vaporized, the gel structure began to shrink and break up. Shrinkage of the silica network occurs when the imbibitional pressure created by the solvent is removed. The gel structure transformations can be quantified by embedding fluorescent markers in the gel.

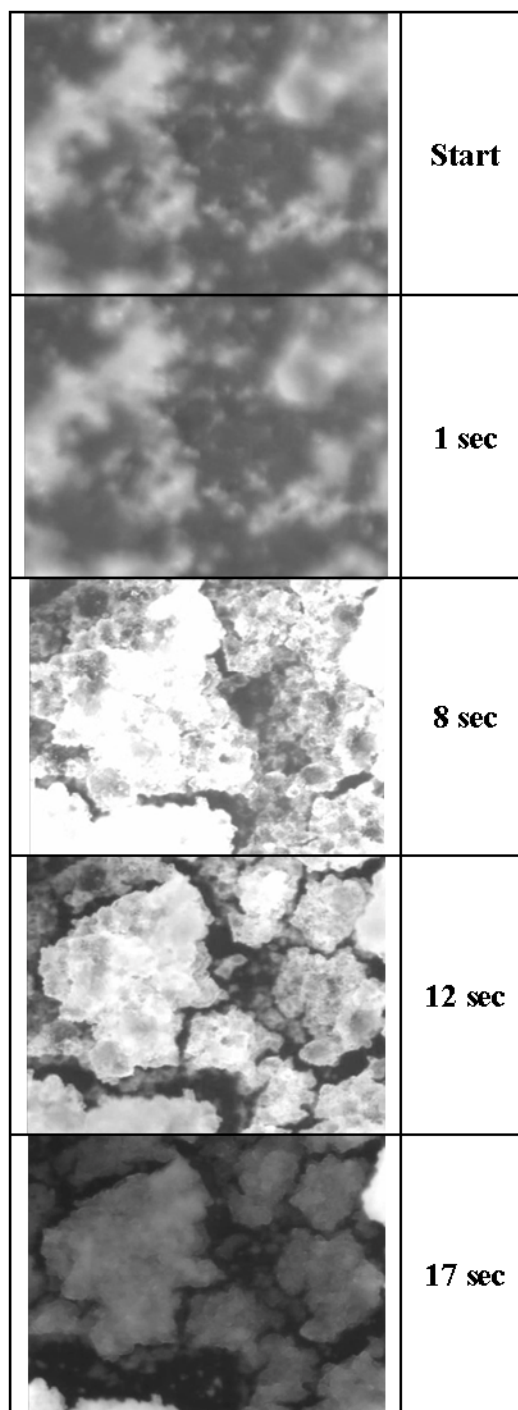


Figure 36: Evolution of a Hexane-based Gel Structure Under Evaporation

4.1.7 Rheometry (Yield Stress, Storage, and Loss Modulus)

All rotational rheometry was performed with a Rheometrics ARES strain-controlled rheometer at 25 °C. The rheometer works by measuring the response (shear stress: τ) of the gel to an oscillatory strain (ϵ). In purely elastic materials, τ occurs in phase with ϵ . In

purely viscous materials, τ will lead ε by 90° . The relationship of shear stress to strain of an intermediate material (elastic + viscous) is given by:

$$\begin{aligned}\varepsilon &= \varepsilon_o \sin(\omega \cdot t) \\ \tau &= \tau_o \sin(\omega \cdot t + \delta)\end{aligned}$$

From this, the shear storage (G') and loss (G'') modulus are defined as:

$$\begin{aligned}\text{Storage : } G' &= \frac{\tau_o}{\varepsilon_o} \cos(\delta) \\ \text{Loss : } G'' &= \frac{\tau_o}{\varepsilon_o} \sin(\delta)\end{aligned}$$

A sweep of frequency was performed at each strain amplitude to determine G' and G'' . The limit of the gel's linear response (yield point) was acquired by increasing strain amplitude until the shear stress began to disappear. At this point, yield stress ($\tau_y = G' \cdot \varepsilon$) was determined. If the strain did not exceed the established yield point, the test could be performed again with the same plateau in τ ; otherwise the plateau would always be lower (confirming the established assessment of yield point).

The values of G' , ε , and τ (at the yield point) were reported for each of the organic gels tested and formed the basis of subsequent property prediction. Figure 37 shows the response of a Tri-ethylamine gel (11% Cabosil) to increasing strain amplitude. This gel had a yield stress of ~ 460 Pa, as seen in the peak of the $\varepsilon \cdot G'$ curve.

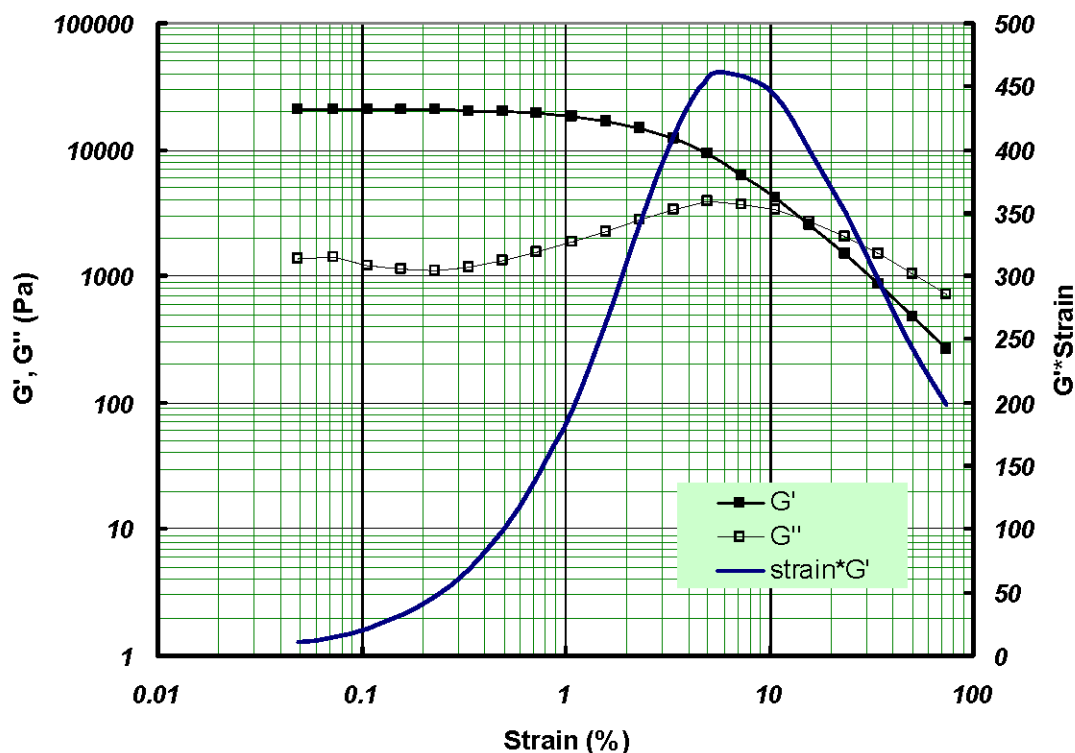


Figure 37: Storage Modulus G' , Loss Modulus G'' , and Stress vs. Strain. Yield Stress ~ 460 Pa. (Tri-ethylamine 11% Cabosil)

The primary determinant of gel yield point properties was found to be silica-loading level (see Figure 45). Yield stress increased with silica fraction (c), within the alkanes, approximately as:

$$\tau_y = K(c - c_o)^a$$

Where c_o denotes the minimum silica weight fraction capable of producing observable gel properties. For the alkanes: $a \approx 1$ and K was on the order of 25,000-30,000 Pa. Not all gels had the same measurable characteristics.

Strong gels of varying strength were formed by the alkanes, alkenes, and cyclic alkanes. Small nitro-generated alkanes (nitro-methane, nitro-ethane, and nitro-propane) all formed strong gels, with nitro-methane being notably stronger than the others (+50%). Weaker gels were formed from acetone (order of magnitude weaker than alkanes). Additionally, all of the alcohol-based gels were found to be weak and failed to remain gelled unless stored with no ullage space, to prevent evaporation.

The general conclusion from the rheometry studies is that the presence of an $-OH$ functionality in an organic solvent results in poor gelation (see Figure 38). The fact that ketone with $=O$ (doubly bonded oxygen) can undergo the keto-enol tautomerization (8) to

form an -OH , under the influence of a trace acid or base, suggests that the surface of the fumed silica may interact with ketones to promote this reaction. The evidence to this point seems to support literature claims (9) that the stabilizing force is due to solvation effects associated with the tendency of materials with H-bonding capabilities (other than water) to coat the silica surface.

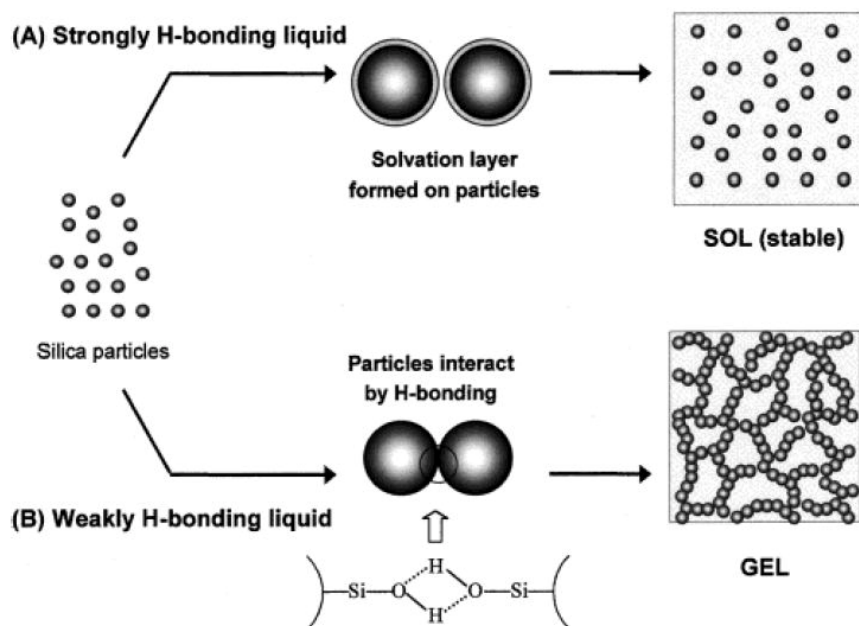


Figure 38: Schematic representation of two possible scenarios that can occur in the case of silica particles dispersed in a liquid: (A) strongly H-bonding liquid (a solvation layer is formed on the particles by H-bonding, resulting in a stable sol); (B) weakly H-bonding liquid (the particles interact directly by H-bonding to form a gel) [9].

4.1.8 Gelation Dynamics

The gelation process was studied on aqueous colloidal silica (CS) dispersions comprised of Ludox SM 30 (Grace-Davison / Sigma-Aldrich). The spherical CS particles, in these dispersions, are in the 15-18 nm diameter range, based on light scattering analysis in diluted samples. Dispersions were received as a stable mixture of 30% silica (by weight) in water. This corresponds to a baseline silica volume fraction (ϕ) of 0.16; the fraction was either reduced or increased through the addition of water or controlled evaporation respectively.

As delivered, the CS dispersions have a pH of 9 or slightly greater. At this pH, the silica surface is negatively charged, stabilizing the dispersion against flocculation (providing a protective maximum in the interaction potential due to Coulombic repulsion). The attractive forces, which bind the particles of a gel structure together, are thought to be due to van der Waals interactions (which occur beyond the Coulombic barrier); but may also involve hydrogen bonding of the silica surfaces. To destabilize the dispersion in a controlled and tunable fashion, varying levels of aqueous NaCl solution was added to the Ludox. Brinker and Scherer (3) indicate that the added ionic strength of the solvent upon salt addition causes the Coulombic repulsion from ionized surfaces of the dispersed silica particles to be screened, leading to capture in the attractive potential (van der Waals). The observed behaviors (structural-light scattering and mechanical-rheology) following the mixing time and quantity of added NaCl solution is described further in the following sections.

4.1.8.1 Dynamic Light Scattering (DLS)

Dynamic Light Scattering (DLS) was used to access the structure (average flocculated object size) of the emerging gel. DLS measures the de-correlation with time of the diffuse intensity in light passing through the mixture. De-correlation in intensity occurs near the mean free time of the mixture, which can be linked to the average particle radius through Brownian diffusion relationships.

The DLS studies were performed using scattering at 90 degrees from the incident Ar laser beam (wavelength of 488 nm) in either fixed or mobile mode; the latter involving translation at speeds on the order of microns/second to study the gelled materials. A standard photo-multiplier, counter, and correlator system was used.

Mixes of aqueous CS were prepared with varying levels of NaCl solution (used to destabilize the dispersion) and monitored by DLS for average hydrodynamic radius ($\langle r \rangle$). As can be seen in Figures 39 and 40, $\langle r \rangle$ has an initial power law growth period followed by a rapid divergent growth (indicating the onset of gelation). In addition, the rapid growth rate occurs earlier with higher NaCl concentration, due to a breakdown in the Coulombic repulsion barrier. This effect becomes saturated at large NaCl concentrations, where the growth is limited solely by diffusion. It is also noted that the mixtures become more poly-disperse as the flocculation process occurs (up to the point where the gel network begins to span the entire mixture) and there should be significant spread around the mean radius.

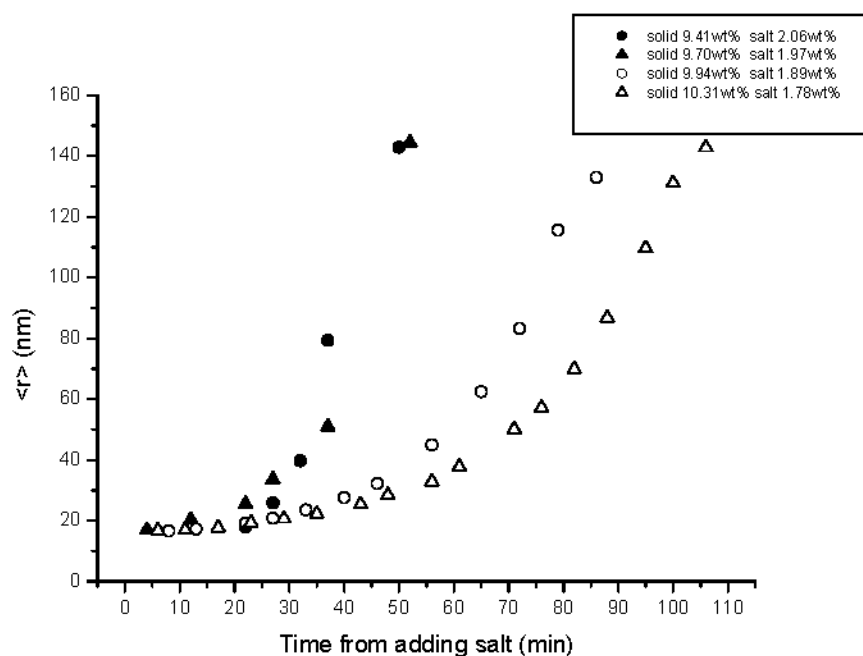


Figure 39: Hydrodynamic Radii of Clusters, Measured with DLS, During the Gelation Process Following Addition of Salt (% weight) at Various CS Percentages

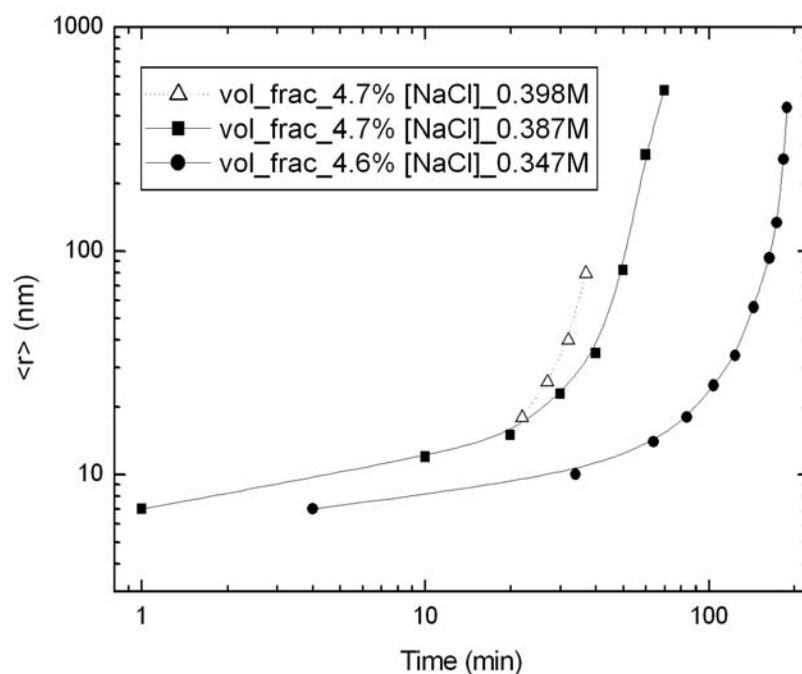


Figure 40: Hydrodynamic Radii of Clusters, Measured with DLS, During the Gelation Process Following Addition of Salt (molarity) at Various CS Percentages

The time at which divergence of $\langle r \rangle$ is observed is one measure of the gelation time of the dispersion. Table 6 shows DLS-based measurements of gelation time for some of the NaCl concentrations tested.

*Table 6: DLS-Based Measurements of Gelation Time at Various NaCl Concentrations
(From Results Shown in Figure 39)*

% Weight NaCl	2.06	1.97	1.89	1.78
Gelation Time (min) by DLS	40	52	92	106

A second more fundamental indication of gelation time is obtained through dynamic measurements of elastic modulus. As will be shown, these measurements agree well with one another, although the rheological approach indicates a slightly earlier gelation time. As noted in Richter et al. (4), DLS-based gelation times do not always accord with the mechanical definition of the gel determined by linear viscoelastic rheology. This is likely related to the fact that a single scattering angle experiment probes at a particular characteristic length (due to heterogeneity of the gel) while rheometric tests intrinsically probe all scales. Methods (5) have been applied to CS gels to develop improved understanding of the heterogeneity in the gel structure, which could help establish a better approach to DLS-based measurements of gelation time.

4.1.8.2 Dynamic Rheology

The same materials studied by DLS have been monitored continuously using oscillatory rheometry, by measuring the storage (G') and loss modulus (G''). In Phase I, a method using an overlaying layer of low viscosity oil (immiscible with the aqueous silica solutions) was shown to be essential for extended rheometric measurements; this approach was used in the rheometry described here.

The tests were performed at a fixed strain of 100% per cycle, as apposed to the standard fixed stress. Figures 41 and 42 show typical responses of G' and G'' after the addition of salt. The values of both G' and G'' are seen to increase strongly at a time starting just under 80 minutes after salt addition. According to the Winter and Chambon (6) criterion of parallel dependence of G' and G'' on frequency, the gel time associated with each figure appears to be between 80 and 90 minutes. The corresponding DLS measured gel time of Figure 39 is noticeably higher (106 minutes).

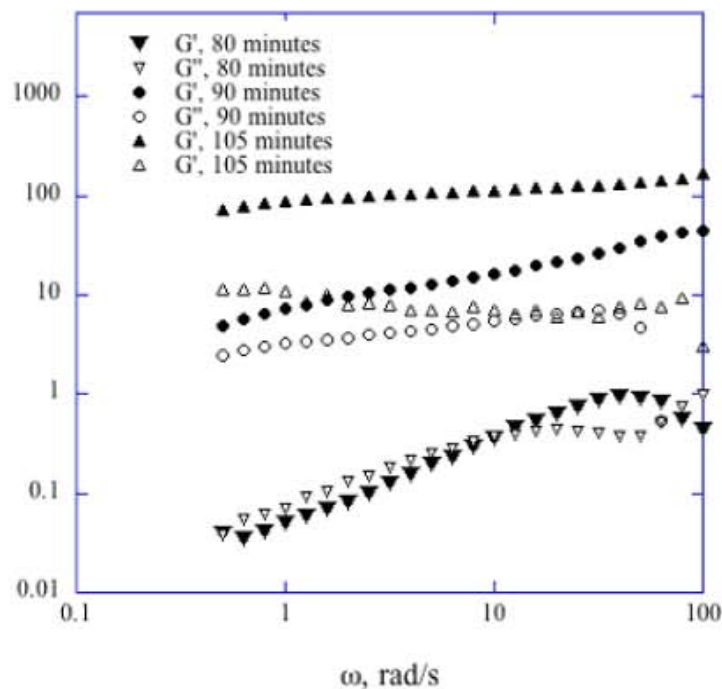


Figure 41: The storage and loss moduli obtained at a strain of 100% from the dispersion of 1.78-wt% salt and 10.31 wt % SiO₂. The same symbol, open and closed, respectively, is used for G' and G'' at the noted times after adding the destabilizing salt solution.

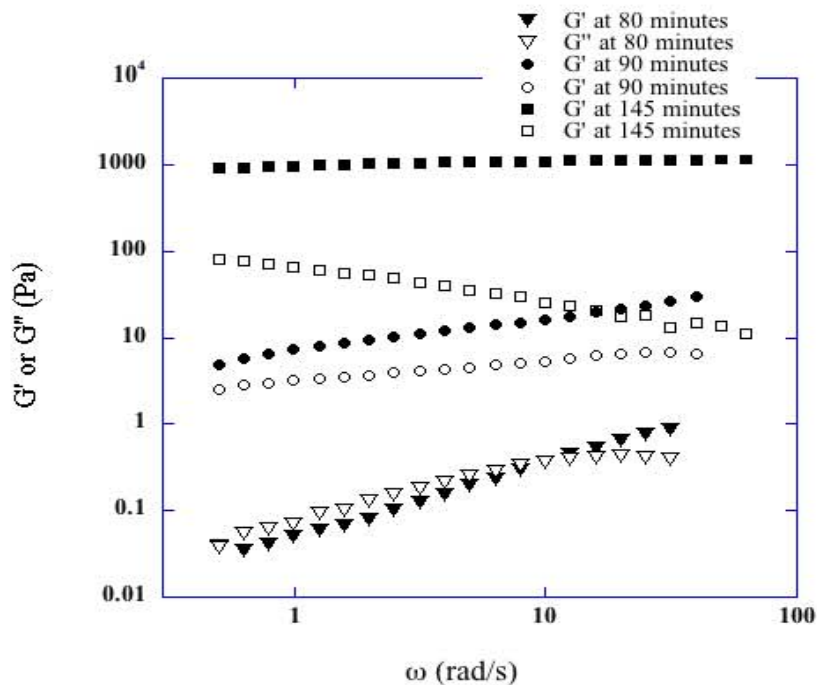


Figure 42: Elastic (G') and loss (G'') moduli as a function of the oscillation frequency for a CS dispersion of 5.2 % silica by volume, and 0.347 M in NaCl at three times following addition of salt.

It is noted that there was difficulty in establishing the exact time when the gel criterion was satisfied, since the duration of the frequency scan was comparable to the rate at which G' and G'' showed significant change. In addition, the LVR rheological properties were at the limit of the instruments torque measurement accuracy for the un-gelled aqueous CS dispersion. A pragmatic method of assessing the gelation time, which yields an essentially equivalent gel time, is to associate gelation with the onset of a growth in G' to reliable measurement levels.

Following gelation, two characteristics of the gel were most notable (see Figure 43). The first is that both G' and G'' increase markedly with time following the onset of gelation. The second point is that the failure strain (ϵ^*) decreases considerably (from 0.3 to 0.02 %). Loss in elasticity of the gel indicates that the microstructure is increasingly rigidified as time passes, due to greater connectivity, which allows less flexural motion without bond rupture.

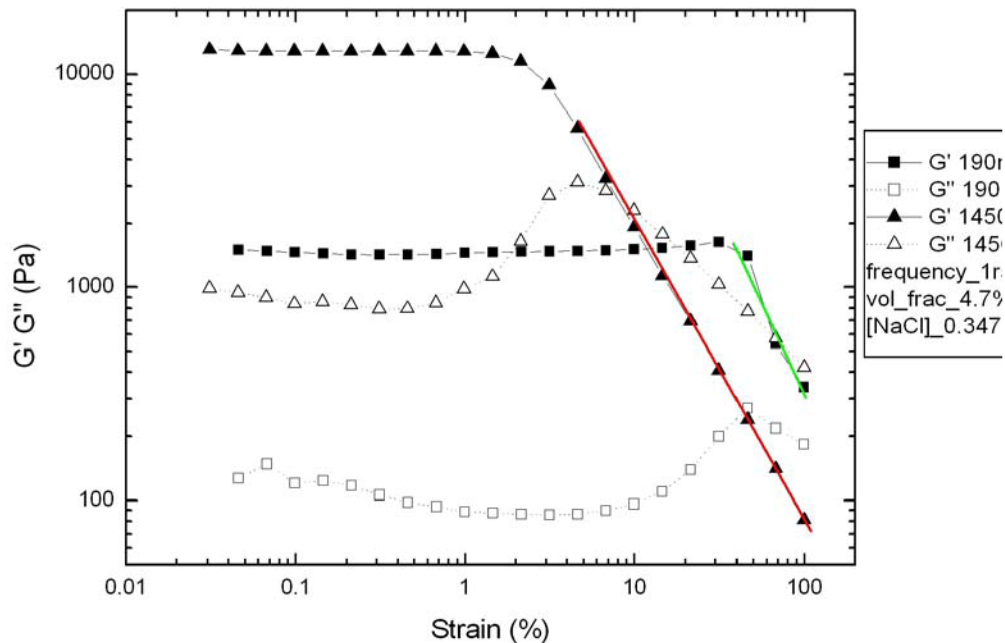


Figure 43: Strain Sweeps at 190 and 1450 Minutes After Salt Addition (0.347 M) for a Ludox Dispersion at $\phi = 0.047$

4.2 Organic Gel Mixing / Database Development

The main goal of this project was to develop a QSPR model that predicts bulk gel properties from the various components and mixing techniques used in creating the gel. Initial efforts were aimed at linear regression relationships originating from molecular level descriptors, such as molecular electrostatic potential (MEP). It was latter decided that using indirect macroscopic descriptors, such as: liquid density, viscosity, and silica loading, would work equally as well in a neural network-based architecture. In order to train the network, a large database of gel properties had to be constructed.

4.2.1 Initial Production

Organic gels were prepared by CFDRC in rented lab space at Oakwood College and latter at Shelby Research Center (Huntsville). The gels were mixed (using Cabosil fumed Silica) in a 1-gallon pneumatically actuated mixer; additional smaller batches were mixed with a 500-ml hand actuated mixer (see Figure 44).



*Figure 44: (A) Gallon Size, Pneumatic Mixer, and (B) 500ml Hand Operated Mixer
(Images Not to Scale)*

Initial samples of gelled heptane were prepared to form a baseline for subsequent mixing techniques and Cabosil loading percentages. With the product literature from Cabot and experience in making water gels, an initial 4% Cabosil loading (by weight of solvent) was used. This resulted in a gel that was too thin. Cabosil was then added to the mixture (up to 8.2% total) until the gel was too thick with incomplete mixing. A new batch of gel was prepared with 7.6% Cabosil, which was again too thin. Finally, a sequence of small batches was prepared until the desired consistency was attained at 9% Cabosil loading.

Following the heptane loading experiment, CFDRC concluded that after a gel is mixed, it is not possible to disperse any more Cabosil. Consequently, the Cabosil needs to be completely wetted with the liquid solvent quickly (comparable to the gelation time) to ensure total mixing of the gel batch.

As with heptane; hexane, pentane and iso-pentane were all gelled with 9% Cabosil. Gelling of alcohols, however, involved more than simple percentage Cabosil loading. As mentioned in Section 3.1.7, hydrogen bonding from the alcohol prevents the development of network formations between Cabosil aggregates. This can be overcome through the use of surfactants, which inhibit bonding between the solvent and Cabosil.

The surfactant recommended by Cabot (Duomeen TDO) is a waxy solid and had to be completely dissolved into the solvent before mixing in the Cabosil. After preparing a number of small test batches, it was found that an 8% Cabosil and 0.96% surfactant loading produced the desired gel consistency. These percentages were used to create gels from n-propanol, iso-propanol, methanol, and n-butanol.

It is noted that the total required loading (surfactant + Cabosil) of alcohol-based gels was similar to the alkanes but required less Cabosil. Future experimentation may find surfactants capable of lowering the required Cabosil loading even further for all types of gels.

4.2.2 Gel Test Matrix

With baseline mixing techniques and percentages in place, an initial test matrix was established to determine the relative influence of silica loading on gels of the following alkanes: hexane, octane, and decane. The gels were loaded with 7, 9, and 11% fumed silica and compared by yield stress using data in the Linear Viscoelastic Range (LVR) (see Figure 45). It was noted by CCNY that the gels were weak and failed to remain gelled unless stored with no ullage space.

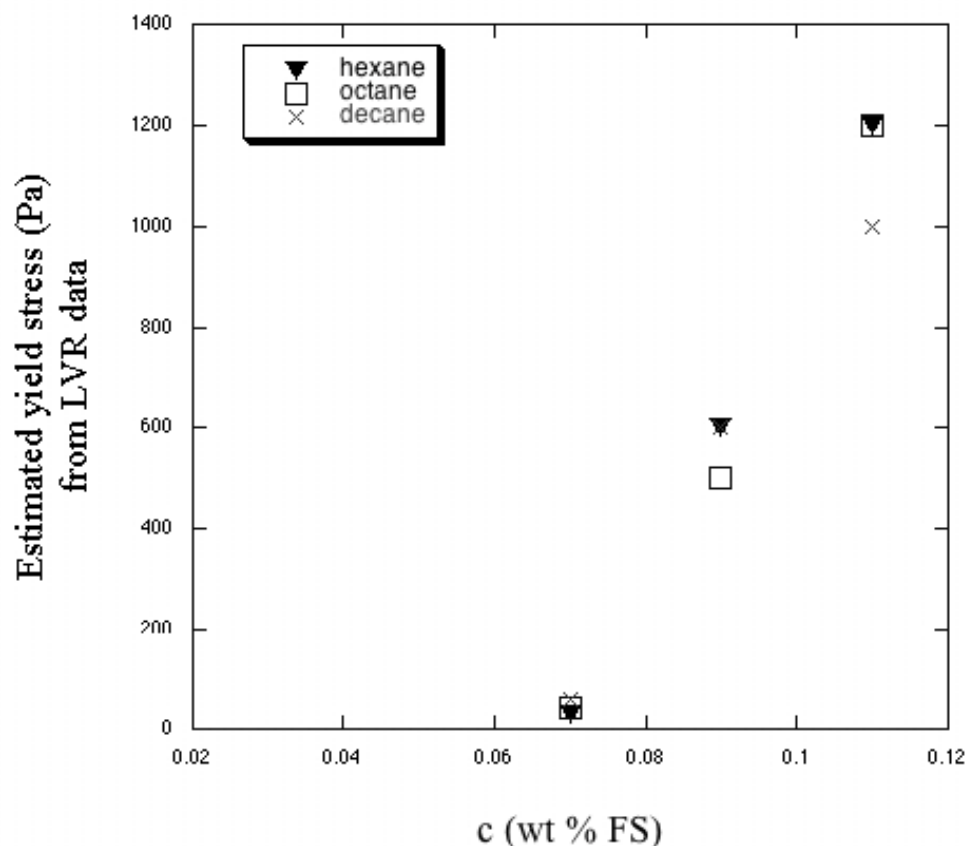


*Figure 45: Results of Yield Stress for Initial Test Matrix of Alkanes (CCNY data)
Showing a Strong Dependence on Silica %*

As can be seen in Figure 45, silica loading is more influential than solvent type (likewise MEP and other solvent descriptors) in determining yield stress within the alkanes family. As a result, it was determined that testing only select members of each organic group would significantly reduce the size of the test matrix without losing generality in the capabilities of the QSPR model. Consequently, the problem of determining descriptors characteristic of a specific organic group would have to be resolved.

In order to draw out the impact of solvent type, subsequent gel samples were mixed in distinct silica-loading groups across all of the selected solvents. The first group that was tested (9% silica) resulted in gels that were too thin (liquid in some cases), most of which failed the 50-caliber test. An additional group (11% silica) was added, which had a much higher 50-caliber pass rate (except for the alcohols, ketones, and the mono and di-substituted amines). The complete gel database is given in Tables 7 and 8. Gels from the 9% data that were too thin for storage modulus measurements were assigned a default value of 10 Pa for preliminary QSPR modeling purposes.

Table 7: The (9%) Gels Database (06/08/2008)

Solvent/Liquid	Measured Gel Properties (9% Silica by Weight)					
	Storage Modulus	2000G/90min	10000G/30min	Density	Bulk Modulus	.50 Cal Test
	G' (Pa) CCNY	(%) Syneresis NJIT	(%) Syneresis NJIT	(g/ccm) CFDRC	E (MPa) CFDRC	Pass/Fail CFDRC
1 N-Pentane	36092	0.6	6.15	0.71	671	Fail
2 Iso-Pentane	21422	1.1	11.11	0.69	654	Fail
3 Hexane	20747	3	17.14	0.76	928	Fail
4 Heptane	17265	5.2	17.39	0.76	957	Fail
5 Octane	24501	8.4	21.69	0.79	1059	Fail
6 Iso-Octane	17270	11.5	25.75	0.77	883	Fail
7 Decane	19163	9.9	23.52	0.83	1189	Fail
8 Cyclo-Hexane	23400	10.2	30.58	0.87	1312	Fail
9 Hexene	14666	8.57	31.98	0.77	817	Fail
10 Cyclo-Hexene	32798	2.21	22.76	0.91	1288	Fail
11 Benzene	36014	7.21	27.48	0.98	1458	Fail
12 Methanol (w/Surf)	729	31.6	46.72	0.91	1142	Fail
13 1-Propanol (w/Surf)	39	39.1	47.44	0.91	1367	Fail
14 1-Butanol (w/Surf)	10 (?) Liq.	38.34	47.72	0.93	1370	Fail
15 Hexanol (w/Surf)	10 (?) Liq.	41.11	50.29	0.94	1528	Fail
16 Octanol (w/Surf)	10 (?) Liq.	32.65	39.55	0.95	1630	Fail
17 Decanol	4806	12.96	24.44	0.93	1662	Fail
18 Nitromethane	47170	3.06	23.91	1.27	2029	Pass
19 Nitroethane	29893	7.68	27.63	1.16	1723	Fail
20 Nitropropane	33383	9.49	28.98	1.1	1621	Fail
21 Triethyl Amine	14300	25.34	43.5	0.82	1025	Pass
22 Diethyl Amine	19000	25.54	43.15	0.8	1008	Pass
23 n-PropylAmine	10 (?) Liq.	41.04	52.48	0.82	1248	Fail
24 Acetone	2357	34.2	43.46	0.909	1229	Fail
25 Methyl-Ethyl Ketone	1600	40.53	50.5	0.9	1305	Fail
26 MIBK	655	33.96	63.18	0.91	1308	Fail
27 1-Propanol No Surf.	1000	39.1	52.4	0.91	1324	Fail
28 Octanol No Surf.	N/A	N/A	N/A	0.95	1656	Fail
29 I-Propanol w. Surf	N/A	N/A	N/A	0.92	1346	Fail
30 Butanol No Surf.	N/A	N/A	N/A	0.93	1411	Fail
31 Hexanol No. Surf.	N/A	N/A	N/A	0.94	1540	Fail

Surfactant - Duomeen 0.9% by weight

Table 8: The (11%) Gels Database (06/08/2008)

Solvent/Liquid	Measured Gel Properties (11% Silica by Weight)					
	Storage Modulus	2000G/90min	10000G/30min	Density	Bulk Modulus	.50 Cal Test
	G' (Pa) CCNY	(%) Syneresis NJIT	(%) Syneresis NJIT	(g/ccm) CFDRC	E (MPa) CFDRC	Pass/Fail CFDRC
1 N-Pentane	58000	0.12	19.86	0.72	673	Passed
2 Hexane	36510	7.17	29.64	0.77	868	Passed
3 Decane	24000	5.8	22.96	0.83	1167	Passed
4 MEK	1689	33.08	43.17	0.93	1357	Failed
5 Acetone	3170	27.22	36.67	0.92	1258	Failed
6 1-Pentanol	310	39.92	49.56	0.92	1426	Failed
7 MIBK	894	29.93	41.26	0.92	1305	Failed
8 Decanol	3511	4.07	7.23	0.95	1731	Failed
9 Methanol	2089	32.69	42.12	0.92	1101	Failed
10 Nitromethane	74179	0.03	14.58	1.29	1964	Passed
11 Nitropropane	34887	2.57	20.26	1.19	1777	Passed
12 Nitroethane	62844	0.03	17.24	1.19	1751	Passed
13 TriEthylAmine	19813	16.49	37.2	0.85	1009	Passed
14 n-ButylAmine	1000	34.25	43.14	0.84	1289	Failed
15 iso-PropylAlcohol	5700	30.88	42.88	0.9	1176	Failed
16 DibutylAmine	1000	35.14	45.63	0.88	1338	Failed

4.2.3 Extraneous Factors

A series of tests were conducted to determine the influence of extraneous factors on gel properties. These include: operator, mixer size, surfactant usage, and storage time. Of these factors, storage time (due to sample transportation and lab-time availability) was found to be the most influential source of error.

In March 2008 the NJIT conducted a re-test on a decane sample prepared in August 2007. The results showed a change in the syneresis (2,000G / 90min) from 9.9 to 6.35 %. This change was attributed to the loss of solvent from the gel due to evaporation.

Repeat samples, not adversely influenced by storage time, were prepared for the solvents and conditions shown in Table 9. The average density (ρ) and modulus of elasticity (E) of the hand mixer batches were found to be within $\pm 1\%$ of the respective gallon mixer batches. This inaccuracy is within uncertainty estimates of the measurements ($\pm 1\%-\rho$, $\pm 5\%-E$). Unfortunately, the volume of the hand mixer batches was insufficient to be sent to CCNY and NJIT for testing. However, since the overall appearance, density, and E values were nearly identical, it is concluded that mixer geometry, mixer size, and variations in operator induced shear rates during mixing do not affect gel quality and properties significantly.

As mentioned earlier, surfactants were used to encourage gelation in alcohol-based gels. To determine the impact of surfactant usage, mixes of short (iso-propanol) and long (octanol) chain alcohols were prepared with and without surfactant, using both the gallon and hand-mixer. The measured values of density and E were identical (within uncertainty) for each case of solvent.

Table 9: List of Repeat Mixes Used to Determine Extraneous Factors in Gel Preparation

Solvent	Gallon Mixer Batch (1)	Hand Mixer Batch (2)	Operator (1), (2)
n-Pentane	G' , (% S)	ρ , E	WHD, WHD
Iso-Pentane	G' , (% S)	ρ , E	WHD, SSD
Hexane	G' , (% S), ρ , E	ρ , E	WHD, SSD
Heptane	G' , (% S), ρ , E	ρ , E	WHD, WHD
Octane	G' , (% S)	ρ , E	WHD, WHD
Iso-Octane	G' , (% S)	ρ , E	WHD, SSD
Decane	G' , (% S)	ρ , E	WHD, SSD
Octanol w/o Surf.	G' , (% S), ρ , E	ρ , E	WHD, WHD
1-Propanol w. Surf.	G' , (% S), ρ , E	ρ , E	WHD, SSD

(% S) – (%) Syneresis, Surf – Surfactant (here 0.9% by weight) Duomeen TDO (N-tallow trimethylene diamine dioleate), WHD – Waite Dykes, SSD – Stelu Deaconu

4.3 QSPR Model: Neural Network

4.3.1 Theory

The established method for estimating properties of new gel formulations is based on Quantitative Structure-Property Relationships (QSPR). Classic, algebraic QSPR has been successfully used in the past for pure liquids. Its application to gels, however, was ambiguous due to the addition of extra factors (gellant, surfactants, etc.).

The chosen method was to implement a QSPR-like property prediction algorithm as a feed-forward / backpropagation neural network (NN). A literature review shows that NN-based QSPR has been implemented, with good results, for the prediction of physical properties of organic compounds (1). The following are advantages of NN implementation:

- 1) Relatively straightforward computer implementation
- 2) A quantifiable, unambiguous breakdown of descriptor influence on the structure-property relationships
- 3) Use of solvent macroscopic physical properties (which are measured rather than computed)
- 4) The possibility of comprehensive learning over the entire liquid / solvent database of interest (at discrete or variable gellant mass fractions)
- 5) Easy to train / re-train with various (user) data sets.

Figure 46 shows the overall feed-forward / backpropagation NN architecture.

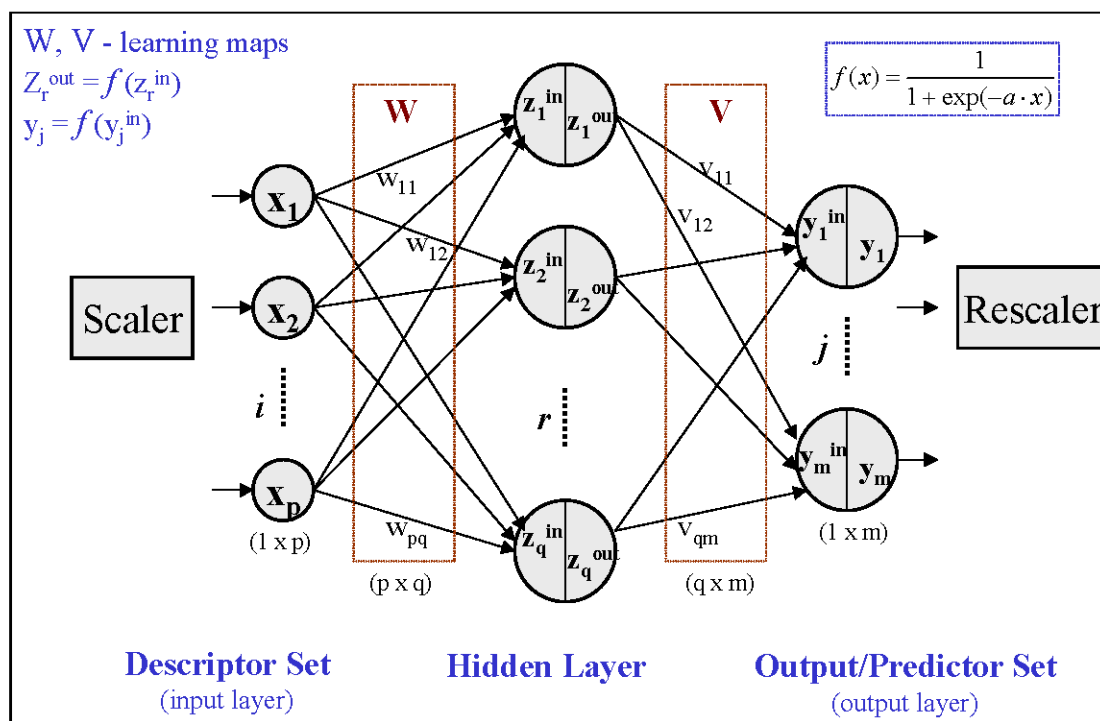


Figure 46: Feed-forward / Backpropagation NN Architecture Used to Predict Gel Properties From Solvent Descriptors

The architecture begins with values of select properties (descriptor set) passing through a scaler, which in our case brings values into the (0,1) range. This is done so that the network-training algorithm is not too far out of balance upon startup. Next, the values are weighted (according to **W**) and sent to the various nodes of the hidden layer. The hidden layer nodes accumulate weighted inputs and activate outputs (z_i^{out}) through an activation function. In our case, the Sigmoid function (shown below) is used for activation, which has the stabilizing advantage of bounding the output to the interval (0,1).

$$f(x) = \frac{1}{1 + e^{-x}}$$

Outputs of the hidden neurons are then weighted (according to **V**) and sent to the nodes of the output layer. The output layer nodes accumulate weighted inputs and activate outputs through another activation function (in our case Sigmoid). The outputs are then re-scaled (based on the scale utilized during training) to provide the predictor set. Output scaling is made compatible with the Sigmoid function range (0,1). In addition, the scale is set in excess of the training data to allow for extrapolated predictions. The overall architecture of the NN can be described by the following equation:

$$y_i^{out} = f\left(\sum_{j=1}^H v_{ij} f\left(\sum_{k=1}^I w_{jk} x_k\right)\right), \quad i \in (1, O)$$

Where H, I, and O are equal to the number of hidden neurons, input descriptors, and output descriptors respectively.

4.3.1.1 Training

The main problem in establishing a network is to select weight arrays (**W** and **V**), which provide an optimal predictor set for a given descriptor set. This is accomplished by providing positive feedback (training) in the form of an error function. The error function was chosen as the square error (SE) between the predictor (y^{pred}) and training (y^{true}) set:

$$SE = 0.5 \sum_{i=1}^N (y_i^{pred} - y_i^{true})^2$$

For the network we have chosen, the sensitivity of SE to the individual weights is given by:

$$\frac{\partial SE}{\partial w_{ir}} = x_i \cdot z_r^{out} \cdot (z_r^{out} - 1) \cdot \sum_{j=1}^O v_{rj} \cdot y_j^{pred} \cdot (1 - y_j^{pred}) \cdot (y_j^{true} - y_j^{pred})$$

$$\frac{\partial SE}{\partial v_{rj}} = z_r^{out} \cdot y_j^{pred} \cdot (y_j^{pred} - 1) \cdot (y_j^{true} - y_j^{pred})$$

These sensitivities define an optimal direction for weight advancement (Δw_{ij} and Δv_{ij}) given by:

$$\Delta w_{ij} = -\mu \frac{\partial SE}{\partial w_{ij}}$$

$$\Delta v_{ij} = -\mu \frac{\partial SE}{\partial v_{ij}}$$

where, μ is the learning rate. In our implementation, a local minimum error is found along the optimal direction before the direction is updated on the next training cycle. Training proceeds until a minimum is reached in the SE function. However, this minimum is not guaranteed to be optimal over the entire SE function.

4.3.1.2 Prediction Risk: Nonlinear Cross Validation (NCV)

As mentioned, the error function is used to establish how well the network fits its training data. A prediction risk establishes how well the network will likely predict future data. We have chosen to use nonlinear cross validation (NCV) for prediction risk estimation. In NCV, the training data is divided into v disjoint subsets (D_i) of size N_i . The network is trained with each subset removed from the training data, which forms the following error (CV_i) on the exempt data:

$$CV_i = \frac{1}{N_i} \sum_{D_i} (y^{pred} - y^{out})^2$$

The errors of all exempt subsets are then averaged to yield a prediction risk.

4.3.1.3 Sequential Network Construction (SNC)

Another important issue facing network selection is in determining its size. Excessively large networks tend to over-fit the training data at the expense of increased prediction risk. We use a procedure called Sequential Network Construction (SNC) to establish the optimal number of hidden neurons with respect to NCV.

In SNC, the network architecture is initialized to some arbitrarily small number of hidden neurons. After initial training is performed, NCV is used to establish a prediction risk. Nodes are then added to the hidden layer repeatedly, with training originating from the

previously determined weights. After an arbitrarily large number of hidden neurons has been reached, the network with the minimum prediction risk is chosen. SNC has the following main advantages (2):

- 1) As larger networks are constructed, the features of the previous networks are preserved.
- 2) It is less computationally expensive to cultivate a large network from a small one than to prune nodes of a larger network trained from scratch.

The coding for the SNC algorithm used in this study is listed in Appendix C.

4.3.2 Application

4.3.2.1 Descriptors / Predictors

For the NN to provide worthy predictions beyond curve fitting, there must be intrinsic relationships between the descriptors and output variables. As demonstrated earlier, gel properties follow closely with silica loading and less with the solvent properties of a given organic group. Consequently, appropriate descriptors should be characteristic of the organic group a particular gel belongs to, with some variation inside each group to address local dissimilarities. As seen in the distribution of MEP based parameters for alkanes and alcohols (Table 10), some MEP variables (i.e. σ_{tot}^2 and σ_-^2) would work well in distinguishing organic groups. However, the added effort of computing MEP descriptors was abandoned for the more computationally economic but indirect descriptors of Table 11 (see Appendix A for 9 and 11% silica loading descriptors). These were established by manually removing low impact descriptors from a larger arbitrary property matrix in order to optimize NN output (more than 50 descriptor combinations were tested). NN output was based on the following values:

1. Storage Modulus G' (Pa)
2. Yield Stress (Pa)
3. Syneresis 2000G/90min (%)
4. Syneresis 10000G/30min (%)
5. Gel Density (gm/cm^3)
6. Modulus of Elasticity (MPa)

Table 10: MEP Derived Parameters of Alkanes and Alcohols (Originally Intended as Descriptors in the QSPR Model)

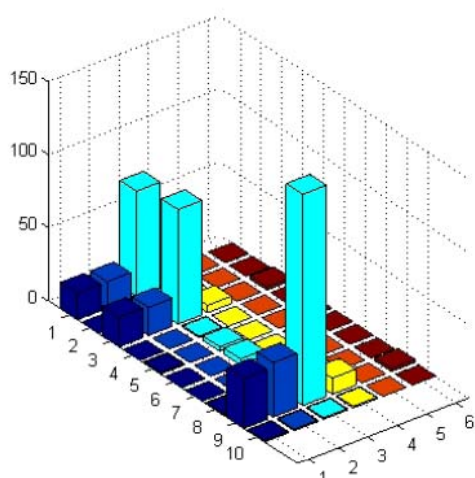
Molecule	\overline{V}_S^+	\overline{V}_S^-	σ_+^2	σ_-^2	σ_{tot}^2	v
Pentane	8.1	-5.0	32.4	10.9	43.2	8.1
Heptane	9.9	-8.0	28.8	17.5	46.3	10.9
Isopentane	4.9	-4.5	13.6	9.7	23.4	5.7
Isopropyl alcohol	6.1	-11.6	29.5	114.0	143.5	23.4
Methanol	11.3	-18.7	28.8	112.2	141.1	22.9

Butanol	8.2	-9.4	39.1	102.0	141.1	28.3
Propanol	5.6	-11.3	24.5	106.0	130.5	19.9

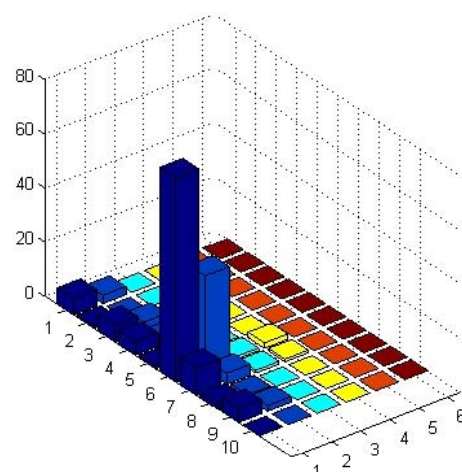
Table 11: Most Effective Descriptor Set (Solvent Properties) To Date (1/12/09) Manually Selected to Optimize NN Output

1. Density	(gm/ccm)
2. Viscosity	(cPoise)
3. Surface Tension	(mN/m)
4. Dielectric Constant	
5. Vapor Pressure	(kPa @ 25°C)
6. Accentric Factor	
7. Dipole Moment (Debye)	
8. Standard Enthalpy of Formation (HF)	(kJ/mole)
9. Melting Point	(°C)
10. Boiling Point	(°C)

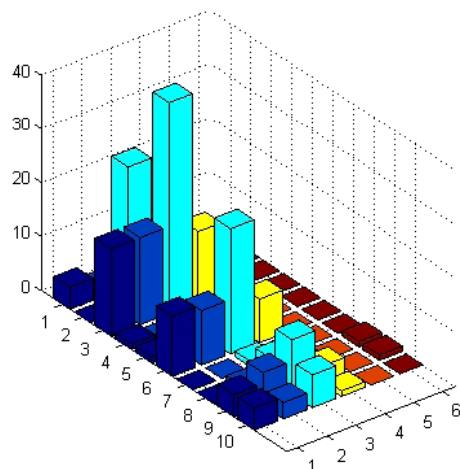
An important part of selecting appropriate descriptor variables was to determine how well the resulting NN detected patterns in the data (mainly group distinction). Without significant pattern recognition, the NN will simply curve fit the training data and exhibit limited predictive abilities. Figure 47 shows Percentage Descriptor Influence (PDI) patterns for a few of the solvents tested (Alkanes and Alcohols at 9% silica loading). PDI was calculated by individually perturbing each input variable, of a given solvent, by 10% and noting the percentage change in the output array. A clear pattern can be seen in the PDI's of the alcohols. The PDI pattern is also an indication of a group's sensitivity to input (predictor) variable error, which was considered negligible during this study.



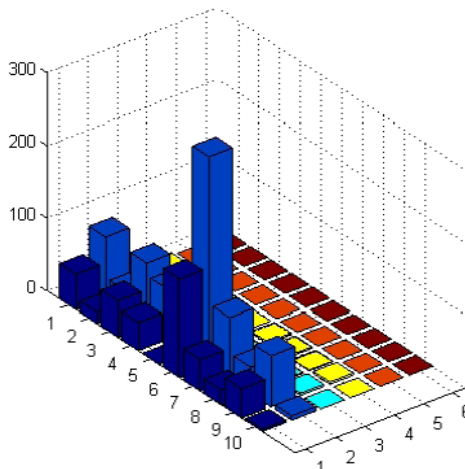
(A) N-Pentane



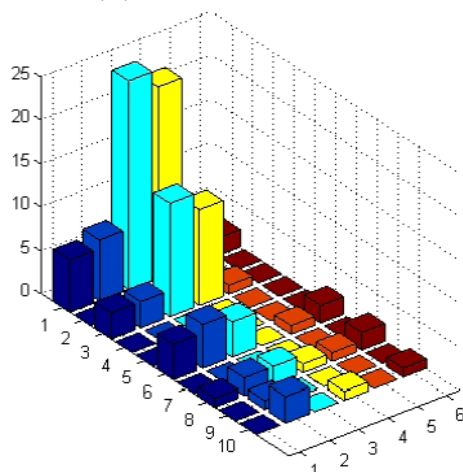
(D) Methanol



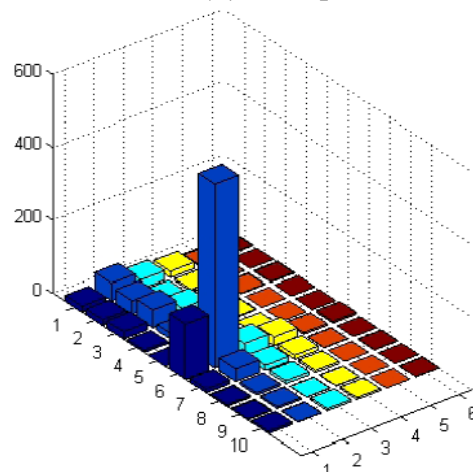
(B) Hexane



(E) n-Propanol



(C) Decane



(F) Decanol

Figure 47: Percentage Descriptor Influence for Alkanes (A, B, and C) and Alcohols (D, E, and F). NN Training with Set of Ten Descriptors and Six Gel Parameters

The PDI patterns of Figure 47 can be an indirect indication of a group's input proximity. Solvents, which are close, will display similar PDI sensitivities. Figure 48 shows the average Euclidian distance between input pairs of the alkanes and alcohols. As can be seen, there appears only a slight natural grouping of the descriptors as a whole. That is, the average distance between any two input descriptor arrays is roughly equivalent, regardless of the two groups the inputs belong to.

Proximity patterns within individual input variables were more favorable to learning. Of all the selected inputs, accentric factor was found the most capable of distinguishing groups (see Figure 49). It is also noted that alcohols showed the greatest PDI with respect to accentric factor.

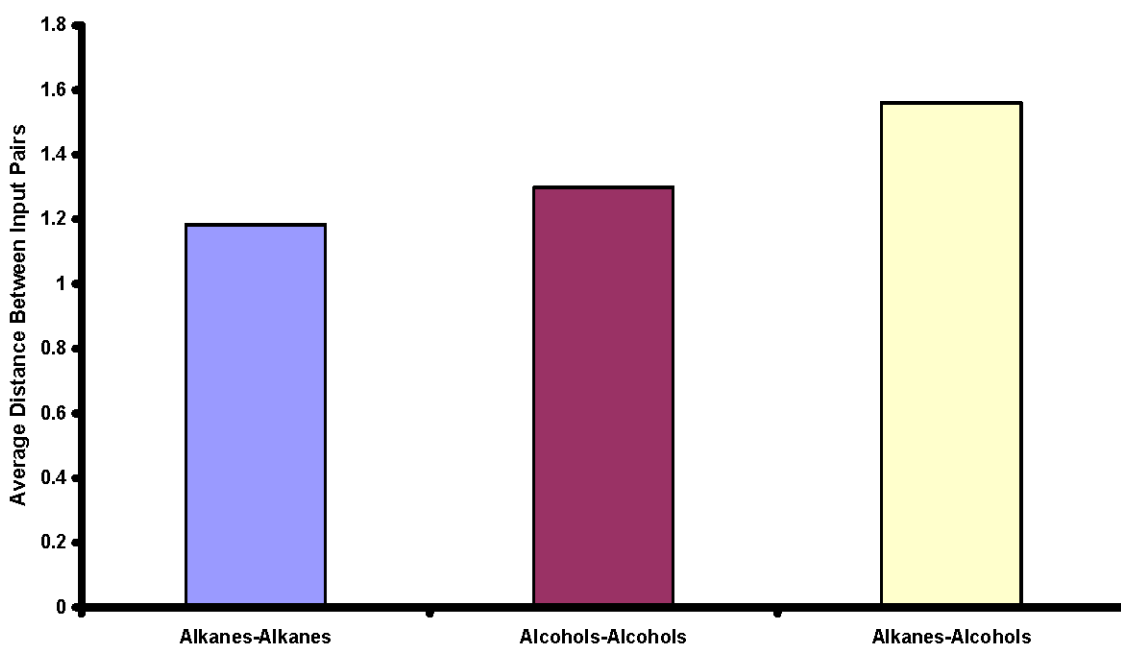


Figure 48: Average Euclidian Distance Between Input Pairs of the Alkanes and Alcohol Groups Showing Only a Slight Distinction Between the Groups

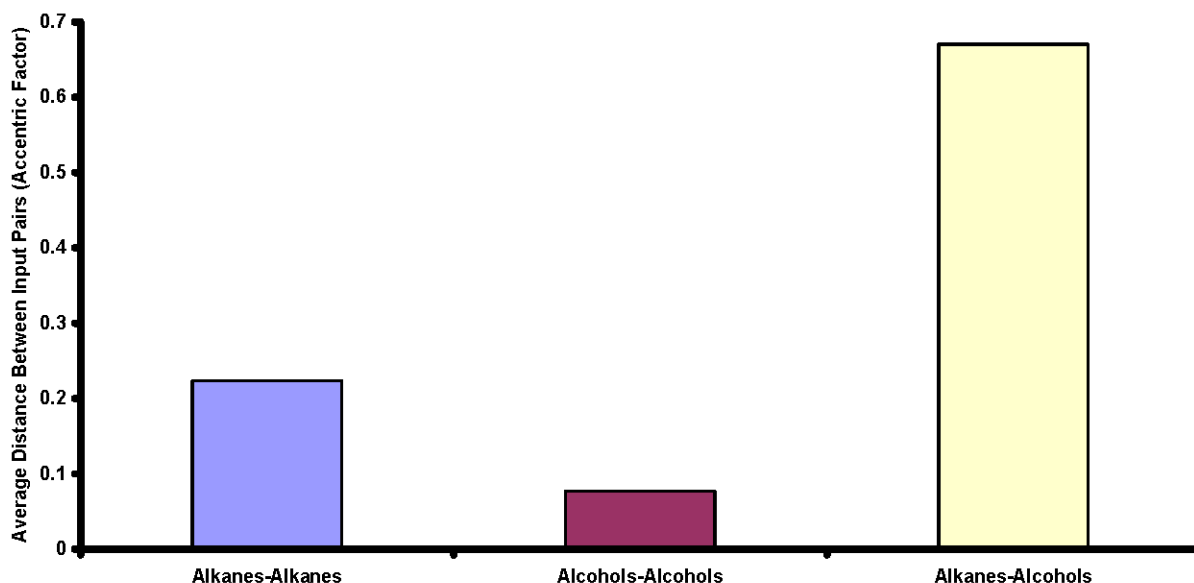


Figure 49: Average Distance (Accentric Factor) Between Input Pairs of the Alkanes and Alcohol Groups Showing a Significant Distinction Between the Groups

4.3.2.2 Training and Validation

Training was performed under constant silica loading using the descriptor (solvent) and predictor (gel) sets shown in Appendix A and Tables 7 and 8 respectively. A NN is typically trained with a large set of well-distributed data. This particular study was complex in that the distribution and number of training data are both limited by the nature of solvents available for testing. In addition, random errors within the training data can significantly warp the results of the network. This presents difficulties in training the NN to predict rather than training it to merely curve fit training sets. In spite of this, the network will in general make predictions no better than its ability to fit the training data. Figures 50 and 51 show examples of the NN's ability to fit its training values.

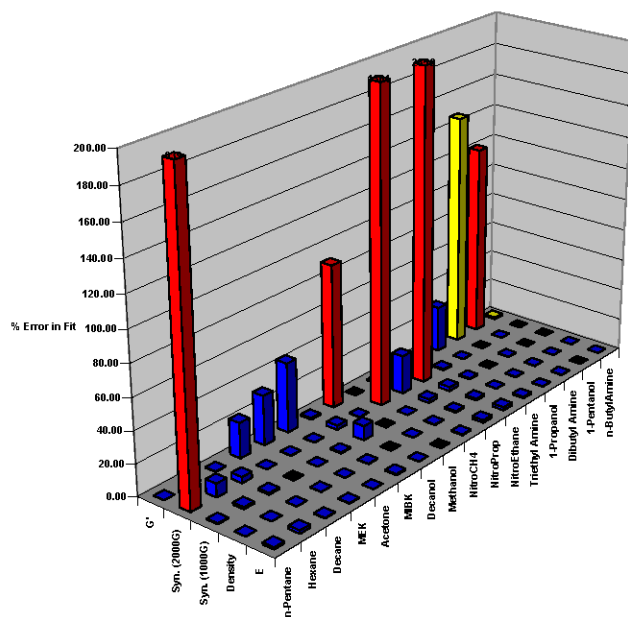


Figure 50: Comparison of NN Fit to its Training Values (Full 11% Data Base with 23 Hidden Neurons) Showing Good Agreement Over Most of the Training Data (Red-Large Spread in the Output Data, Yellow-Arbitrarily Chosen Output Values Used to Fill Void Data, Blue-Normal Data)

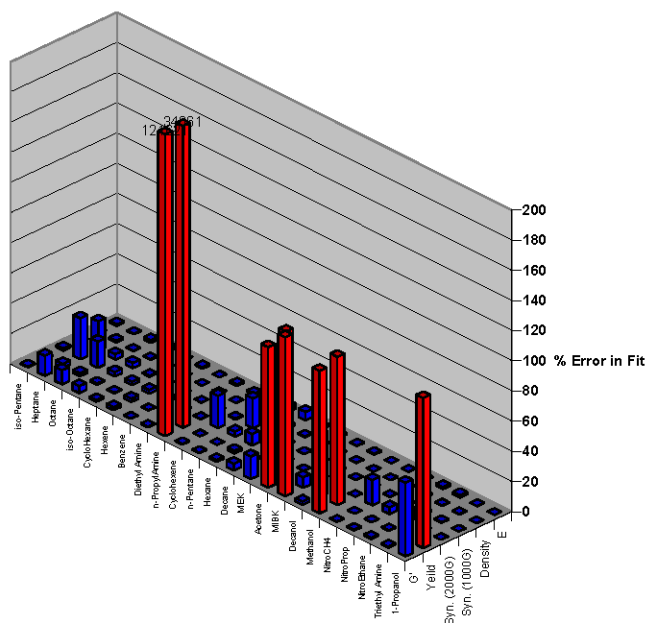
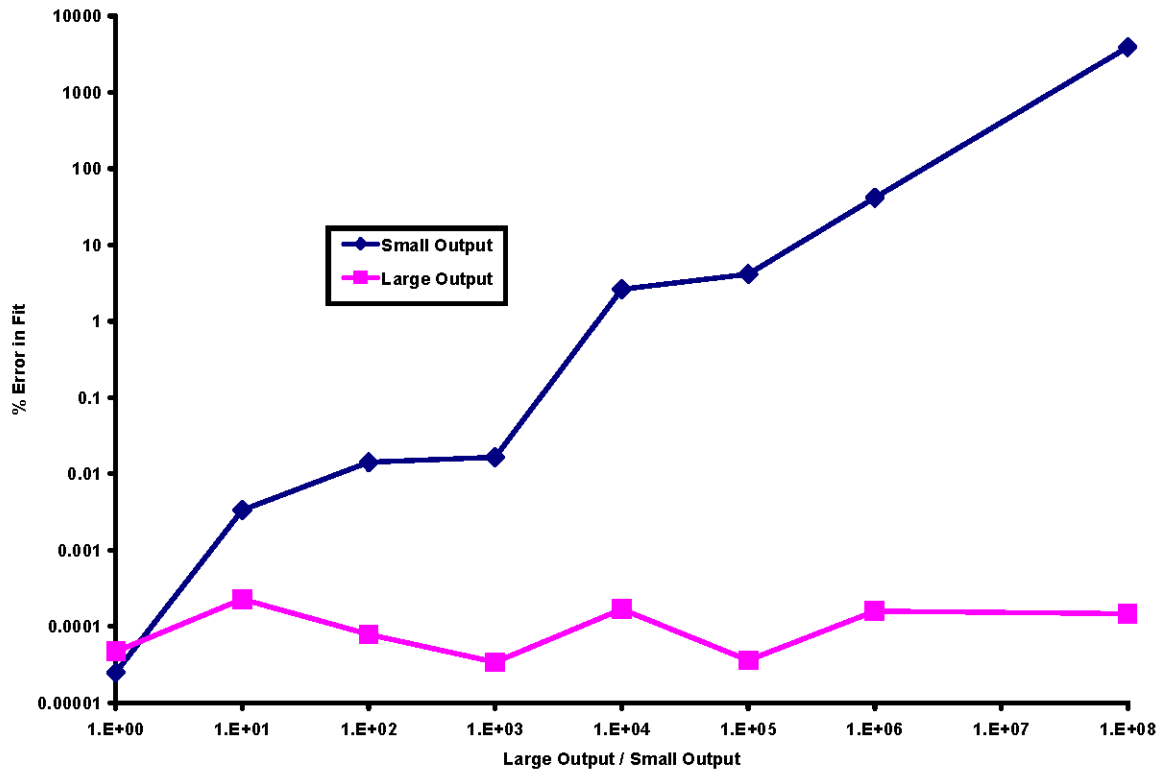


Figure 51: Comparison of NN Fit to its Training Values (Full 9% Data Base with 23 Hidden Neurons) Showing Good Agreement Over Most of the Training Data (Red-Large Spread in the Output Data, Blue-Normal Data)

As can be seen in Figures 50 and 51, the NN is capable of fitting most of the training data very well. However, some fit errors were in excess of 3000%. Poor fits were almost exclusively due to the type of error function used to train the network.

As mentioned, training is based on minimizing the scaled square error. In addition to accommodating the Sigmoid function, scaling is done to eliminate bias towards larger variables of the output array. Nonetheless, the un-scaled absolute error of a given fit is proportional the spread of the respective training variable. Consequently, the relative error of small values can be substantial for data with a large spread. Figure 52 shows the effect of training the NN on a single variable at various spread ratios in two training values. As can be seen, the network tends to favor the larger training variable as the spread increases. This can become especially problematic for training data with large outliers. The problem can be overcome through the use of an error function based on relative error but will require re-formulation of the training algorithm.



*Figure 52: Training on a Progressively Large Spread in the Training Set (Two Values)
Showing a Significant Favor Towards the Larger Output*

Predictability of the NN was established by calculating a prediction risk based on NCV. As the size of the excluded subsets used in NCV decrease (in relation to the full data set), prediction risk reliability increases. Unfortunately, with limited training data, the excluded subset had to be relatively large. Tables 12 and 13 show examples of prediction errors found by removing 6 training sets.

Table 12: Predicted 11% Values Obtained by Removing All of the Listed Solvents from the Training Set (13 Hidden Neurons and Single Output Variable)

Solvent	E (MPa)			Density (g/ccm)			Syn. (1000G/30min)			Syn. (2000G/30min)			G' (Pa)		
	TRUE E	Predicted	%Error	TRUE E	Predicted	%Error	TRUE E	Predicted	%Error	TRUE E	Predicted	%Error	TRUE E	Predicted	%Error
NitroEthane	1751	1881	7.4	1.19	1.22	2.9	17.24	17.19	0.3	0.03	0.84	2712.7	62844	58363	7.1
Triethyl Amine	1009	1022	1.3	0.85	0.85	0.3	37.20	27.59	25.8	16.49	8.33	49.5	19813	42788	116.0
1-Propanol	1176	1022	13.1	0.9	0.80	10.9	42.88	43.07	0.4	30.88	36.39	17.8	5700	1006	82.3
Dibutyl Amine	1338	1384	3.4	0.88	0.92	4.3	45.63	24.61	46.1	35.14	5.64	84.0	1000	37552	3655.2
1-Pentanol	1426	1353	5.1	0.92	0.86	6.7	49.56	23.70	52.2	39.92	13.05	67.3	310	10394	3252.8
n-ButylAmine	1289	1284	0.4	0.84	0.87	3.4	43.14	18.50	57.1	34.25	7.80	77.2	1000	3956	295.6

Table 13: Predicted 9% Values Obtained by Removing All of the Listed Solvents from the Training Set (13 Hidden Neurons and Single Output Variable)

Solvent	E (MPa)			Density (g/ccm)			Syn. (1000G/30min)			Syn. (2000G/30min)			Yeild (Pa)			G' (Pa)		
	TRUE	Predicted	%Error	TRUE	Predicted	%Error	TRUE	Predicted	%Error	TRUE	Predicted	%Error	TRUE	Predicted	%Error	TRUE	Predicted	%Error
Methanol	1142	1196.75	4.8	0.91	0.93	2.2	46.7	19.8	57.7	31.6	25.66	18.8	7	0.12	98.2	729	1594.86	118.8
NitroCH4	2029	1765.03	13.0	1.27	0.94	25.7	23.9	36.4	52.2	3.06	9.90	223.6	1000	237.14	76.3	47170	4453.89	90.6
NitroProp	1621	1614.04	0.4	1.1	0.97	11.6	29.0	58.8	102.9	9.49	36.87	288.5	1100	316.22	71.3	33383	381.83	98.9

NitroEthane	1723	1692.96	1.7	1.16	0.97	16.3	27.6	49.2	78.2	7.68	29.31	281.7	950	437.44	54.0	29893	1200.02	96.0
Triethyl Amine	1025	943.15	8.0	0.82	0.80	2.5	43.5	23.1	46.9	25.34	13.55	46.5	450	393.22	12.6	14300	8155.96	43.0
1-Propanol	1324	1029.03	22.3	0.91	0.88	3.8	52.4	26.7	49.0	27	30.07	11.4	50	0.10	99.8	1000	546.40	45.4

It can be seen that predictions of density and elasticity were on average much better than all other predictions. In addition, the maximum prediction error of these values is significantly less than variability in the test data (i.e. 57% in Density and 98% in E for the 11% data), suggesting that the network is not merely making predictions based on a bulk threshold. The density and E prediction errors are also very similar in size. This is likely due to the inherent similarity between the variables (i.e. $E = c^2 \cdot \rho$).

One possible reason that density and elasticity predictions were more accurate is that their values were measured at Huntsville and did not undergo significant degradation due to long transportation and storage times. A single repeatability study performed by NJIT concluded a 44% change in syneresis over an 8-month period. This amount of error can significantly warp the results of the network. Table 14 shows an example of the effect training set error has on elasticity prediction.

Table 14: Comparison of Predictions Made with Arbitrary Error (-30%) Imposed on One of Ten Training Values (Fit Error Was Within 0.001% for Each Case). Showing Significant Loss in Average Prediction Quality (11% Data)

Solvent	E (MPa)			E (MPa) trained with added error	
	TRUE	Predicted	%Error	Predicted	%Error
NitroEthane	1751	1881	7.4	1708	2.5
Triethyl Amine	1009	1022	1.3	1268	25.6
1-Propanol	1176	1022	13.1	923	21.5
Dibutyl Amine	1338	1384	3.4	1533	14.6
1-Pentanol	1426	1353	5.1	1170	18.0
n-ButylAmine	1289	1284	0.4	1791	38.9
Average			5.1	20.2	

In Table 14, 1 of 10 training values was arbitrarily reduced by 30% and the network was re-trained to predict the same set of values as the undisturbed case. A reduction was used to insure that the influence of variable spread was not introduced. As can be seen, a relatively modest error in just one of ten training values can significantly alter the networks prediction ability. The average prediction error rose from 5.1 to 20.2%. An average error of only 9% was obtained by leaving the training set (associated with the same reduced value) out of training entirely; suggesting that missing data is less detrimental than erroneous data.

As apposed to merely removing an entire data set or variable from training, due to a single missing or suspected faulty value (or even worse supplying arbitrary values to satisfy missing data), CFDRC elected to update the error function so that absent data is simply ignored. In this way, the network utilizes the most relevant information available, which is critical with limited training sets. Better predictability, on data with inherent error, might be achieved in the future through larger training sets involving repeat

samples. The network should disregard random error in the data if the number of repeats is sufficient enough to establish the error as random (i.e. un-correlated).

As mentioned earlier, the training set spread has an unfavorable influence on the networks ability to form accurate fits. Consequently, the upper limit of predictability will suffer for training data with a large spread. In order to achieve better accuracy without modifying the existing training algorithm, a procedure was established where the network is re-trained on the fit error. The new “error network” (NN_{error}) will favor large values and accordingly counter balance the effect of large spread ratios in the original network. The outputs of the two networks are then added for each input array (I) to obtain an overall output (O):

$$NN(I) + NN_{error}(I) = O$$

It is noted that the network size will effectively grow during this process, but significantly outperformed (in terms of speed and accuracy) a single network with comparable dimensions. In addition, the error network is not required to be the full size of the originally trained network. Figure 53 shows the effect of this procedure while training on single output variables of the 11% database. The procedure effectively broadens the networks ability to look past the first minimum it encounters in training error, which is likely, why it outperformed a single network of much larger size. This is due to the fact that the first error minimum reached in training is not necessarily optimal and correlation potential may still exist (inside the error) at this point. As such, the procedure may be repeated indefinitely or until the fit is truly optimal.

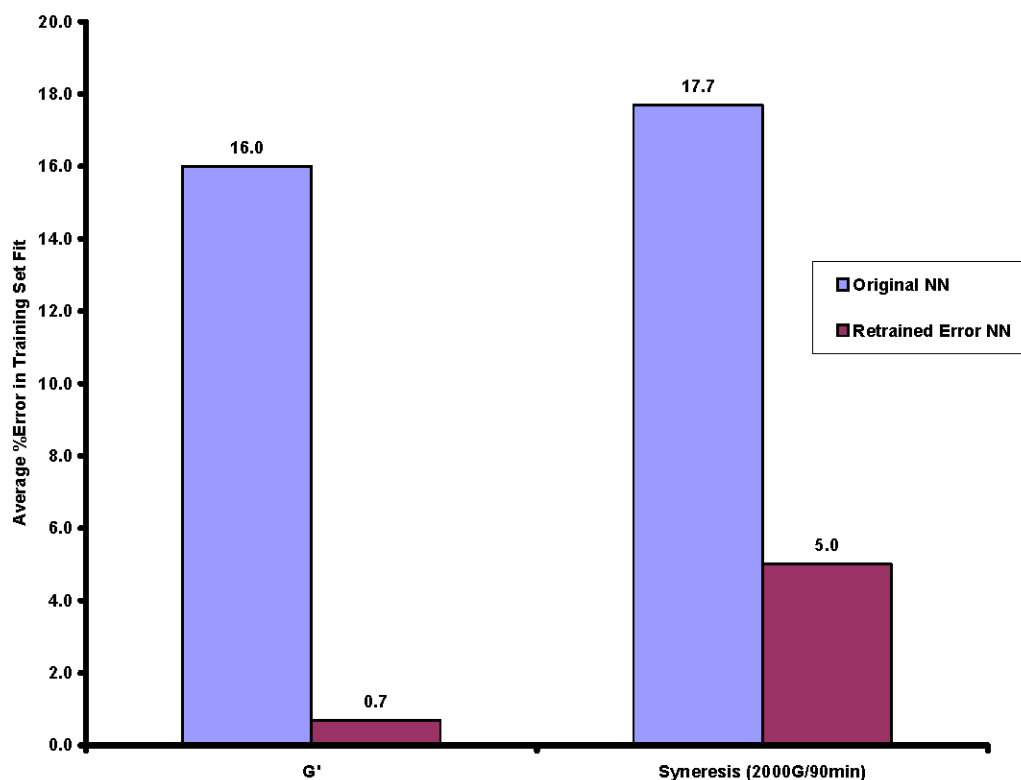


Figure 53: Comparison of Average Fit Errors in a Re-Trained “Error NN” to the Original NN Indicating Significant Potential to Increase Overall Predictive Quality

Another issue that was addressed is connected to the concept of over-fitting. If the error is not random (i.e. established as random through significant repeat data), a large network will tend to fit local correlations in the error. These correlations can be magnified in the predictions of new data. In addition, data that does not have an adequate distribution can create similar results. To address these problems, SNC was used to establish an optimal network size (number of hidden neurons). Figure 54 shows the path taken by SNC in establishing the optimal number of hidden neurons while training on a single output variable. As can be seen a larger network doesn’t necessarily correspond smaller prediction risk ($PR_9 < PR_{11}$), although, it does correspond to the smaller square error.

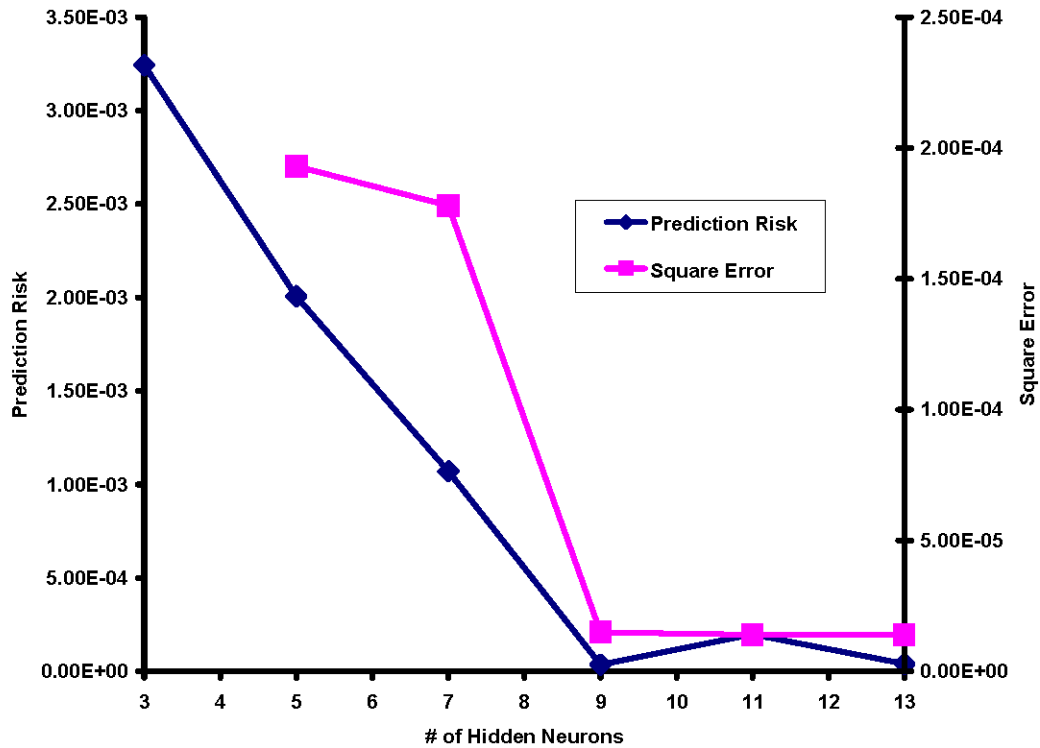


Figure 54: Path Taken by SNC in Determining the Optimal Number of Hidden Neurons (11%-G' Data)

The benefit of using SNC goes beyond finding an optimal number of hidden neurons to reduce prediction risk. As can be seen in Figure 55, SNC can reduce the prediction risk associated with a given network size altogether.

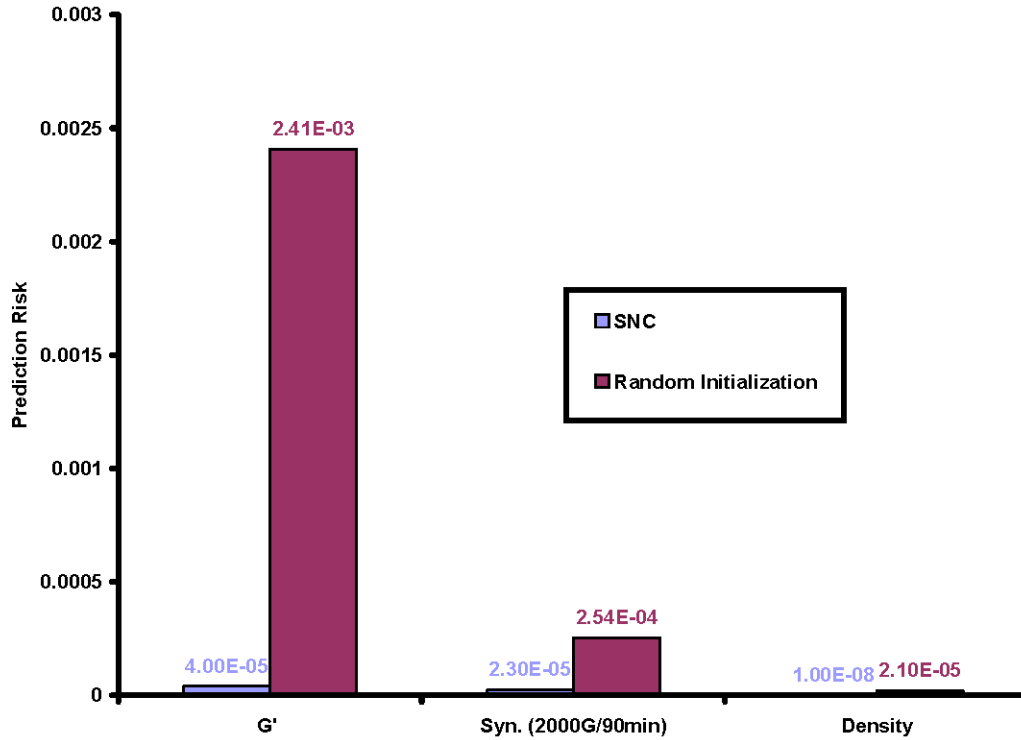


Figure 55: Comparison of Networks (Same Size) Trained with SNC and Random Initialization. Indicating That SNC has Potential Beyond Finding an Optimal Number of Hidden Neurons

Figure 55 compares the training results of SNC produced networks and their random start counterparts. As can be seen the SNC network tends to converge to an overall better prediction risk than training a network from a random weight initialization. This takes place because as the SNC network grows; it accumulates the traits of the networks before it. Starting from a random initialization with a large number of neurons will likely result in the network falling on a minimum error sooner than in SNC, but with a larger value. Consequently, the networks should be periodically optimized using SNC when new training data becomes available. Otherwise, the networks can be re-trained by initializing the weights to those last obtained by SNC.

4.3.3 Python GUI

The primary objective of this task was to design and implement a graphical user interface (GUI) for the NN algorithms and gel database files. The GUI facilitates NN training, prediction, and database organization through a windows-like environment. Consequently, user understanding of the underlying principles and details is not required. In addition, the GUI can be loaded on any platform.

4.3.3.1 Graphical User Interface Application Development

The Python programming language (<http://www.python.org/>) was selected for the implementation of the GUI. Python is an open source, platform independent programming language with minimal syntax and semantics, facilitating rapid implementation. The Python standard library is comprehensive, providing support for web and GUI application development. The Python standard library was supplemented with the wxPython library, an open source, platform independent GUI library developed from the wxWidgets library and the Python programming language. The wxPython library enables the development of applications that utilize the controls and utilities of the native platform, in this case Microsoft Windows. Extensible markup language (XML) read and write functions were implemented utilizing the open source pyXML library.

4.3.3.2 Development of a Chemical Compound Library

A chemical compound library was developed utilizing XML. A primary advantage to using XML is that information may be described in a hierarchical manner, facilitating its proper annotation. The chemical compound library contains physical properties information for three classes of compounds: gellants, surfactants and liquids. The custom XML schema of the chemical compound library is illustrated in Figure 56. The chemical compound library was populated with physical property information from Tables 7 and 8, which includes compound name, CAS number, molar mass, density, melting point, boiling point, standard enthalpy change of formation, viscosity, surface tension, dielectric constant, vapor pressure, accentric factor and dipole moment. In addition, physical properties associated with gel compounds are included in the chemical compound library. These physical properties include density, syneresis, storage modulus, bulk modulus and 50-caliber test. At the moment, the physical properties included in the chemical compound library enable the calculation of:

- ☐ Storage Modulus
- ☐ Yield Stress
- ☐ Syneresis
 - 2000G/90min
 - 100000G/30min
- ☐ Density
- ☐ Modulus of Elasticity

Calculation of other properties can be made possible through a slight restructuring of the GUI.

```

<?xml version="1.0" encoding="UTF-8" ?>
-<compoundLibrary>
-<listOfGellants>
- <gellant name="Sodium silicate" CASNumber="6834-92-0">
  <molarMass unit="g/mol" value="122.06" />
  <density unit="g/cm3" value="2.4" />
</gellant>
</listOfGellants>
-<listOfSurfactants>
- <surfactant name="Sodium dodecyl sulfate" CASNumber="151-21-3">
  <molarMass unit="g/mol" value="288.38" />
  <density unit="g/cm3" value="1.01" />
</surfactant>
</listOfSurfactants>
-<listOfLiquids>
- <liquid name="iso-Pentane" CASNumber="78-78-4">
  <molarMass unit="g/mol" value="72.15" />
  <density unit="g/cm3" value="0.6" />
  <meltingPoint unit="K" value="-160.0" />
  <boilingPoint unit="K" value="27.88" />
  <triplePoint unit="K" value="113.37" />
  <criticalTemperature unit="K" value="460.35" />
  <criticalPressure unit="kPa" value="3395.7" />
  <standardEnthalpyChangeOfFormation unit="kJ/mol" value="-179.0" />
  <standardMolarEntropy unit="J/molK" value="260.7" />
  <heatCapacity unit="J/molK" value="164.85" />
  <viscosity unit="mPas" value="0.214" />
  <surfaceTension unit="mN/m" value="14.45" />
  <dielectricConstant value="1.845" />
  <thermalConductivity unit="W/mK" value="0.111" />
  <vaporPressure unit="C" value="79.3" />
  <acentricFactor value="0.2296" />
  <dipoleMoment unit="D" value="0.1" />
</liquid>
- <liquid name="Hexene" CASNumber="592-41-6">
  <molarMass unit="g/mol" value="84.1608" />
  <density unit="g/cm3" value="0.6731" />
  <meltingPoint unit="K" value="-140.0" />
  <boilingPoint unit="K" value="63.48" />
  <standardEnthalpyChangeOfFormation unit="kJ/mol" value="-74.2" />
  <viscosity unit="mPas" value="0.252" />
  <surfaceTension unit="mN/m" value="17.9" />
  <dielectricConstant value="2.077" />
  <vaporPressure unit="C" value="24.8" />
  <acentricFactor value="0.281" />
  <dipoleMoment unit="D" value="0" />
</liquid>
</listOfLiquids>
</compoundLibrary>

```

Figure 56: The custom XML schema of the chemical compound library

4.3.3.3 Design and Implementation of Chemical Compound Library Management Page

The chemical compound library management page was designed and implemented to enable a user to view, create, edit and delete gellant, surfactant or liquid compounds in the chemical compound library.

A user may navigate to the ‘compound library’ page using the page tabs at the top of the application window (Figure 57). The default ‘compound class’ is liquid. A user may select the gellant, surfactant or gel radio buttons in the compound type panel in order to view the gellant, surfactant, or gel compounds and associated physical properties. The compound names associated with the selected compound class existing within the library are displayed in the list box within the ‘compound name’ panel. A user may select a compound name to view the physical properties associated with the compound name existing within the library. A user may create a new compound by selecting the desired compound class, clicking the ‘new’ button and entering the associated physical property information in the text boxes within the ‘compound properties’ panel. A user may also edit an existing compound by selecting the desired compound class, selecting the desired compound name and editing the associated physical property information. Finally, a user may delete an existing compound by selecting the desired compound class, selecting the desired compound name, and clicking the ‘delete’ button. A warning dialog box will be

displayed and the user may click the ‘yes’ button to delete the compound or the ‘no’ button to return to the compound library page. A user may click the ‘clear’ button to remove compound name selection and associated physical properties.

The chemical compound library management page was designed and implemented to include a minimal and intuitive interface in order to reduce the burden on the user. In addition, the user is aided by error messages displayed for nonnumeric physical property entries. Limiting user error in the management of the chemical compound library will assist in limiting error in calculation.

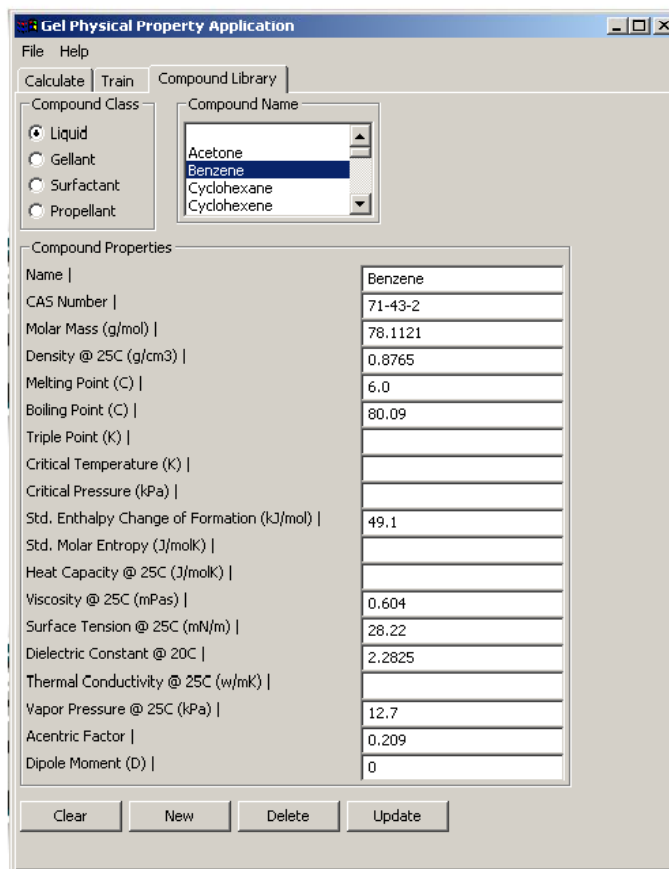


Figure 57: Screenshot of chemical compound library management page

4.3.3.4 Design and Implementation of Calculation Page

The calculation page was designed and implemented to enable a user to calculate the physical properties of a simulated propellant. The ‘calculate’ page is the default page of the application window (Figure 58), however, a user may navigate to the calculate page using the page tabs at the top of the application window. In order to perform a calculation, a user must select a compound name from the ‘compound name’ panel. The user must then select the training library file used in the calculation by entering the file location in the text box within the ‘training library’ panel or by clicking the browse button and selecting the file from the ‘Choose a file’ dialog box. In order to perform the calculation with the selected compound name and training library file, the user must click the ‘calculate’ button. The user may clear the entered information by clicking the ‘clear’ button. Results of the calculation are displayed in the ‘results’ panel.

4.3.3.5 Design and Implementation of Training Page

The training page was designed and implemented to enable a user to select multiple gels, available from the chemical compound library, to view their associated physical properties and to calculate a new training set, which may be saved by the user.

A user may navigate to the ‘training’ page using the page tabs at the top of the application window (Figure 58). A user may then select one or more gel names from the list box within the ‘gel name’ panel and click the ‘add’ button to append the gel name and its associated physical properties to the training list. A user may select a gel name in the training list and click the ‘remove’ button to remove the gel name and its associated physical properties from the training list. A user may remove all gel names and associated physical properties by clicking the ‘clear’ button. In order to create a new training set, a user may add the desired gel names and associated physical properties to the training list and click the ‘train’ button. The results of the training may be saved to a desired location by clicking the ‘save’ button.

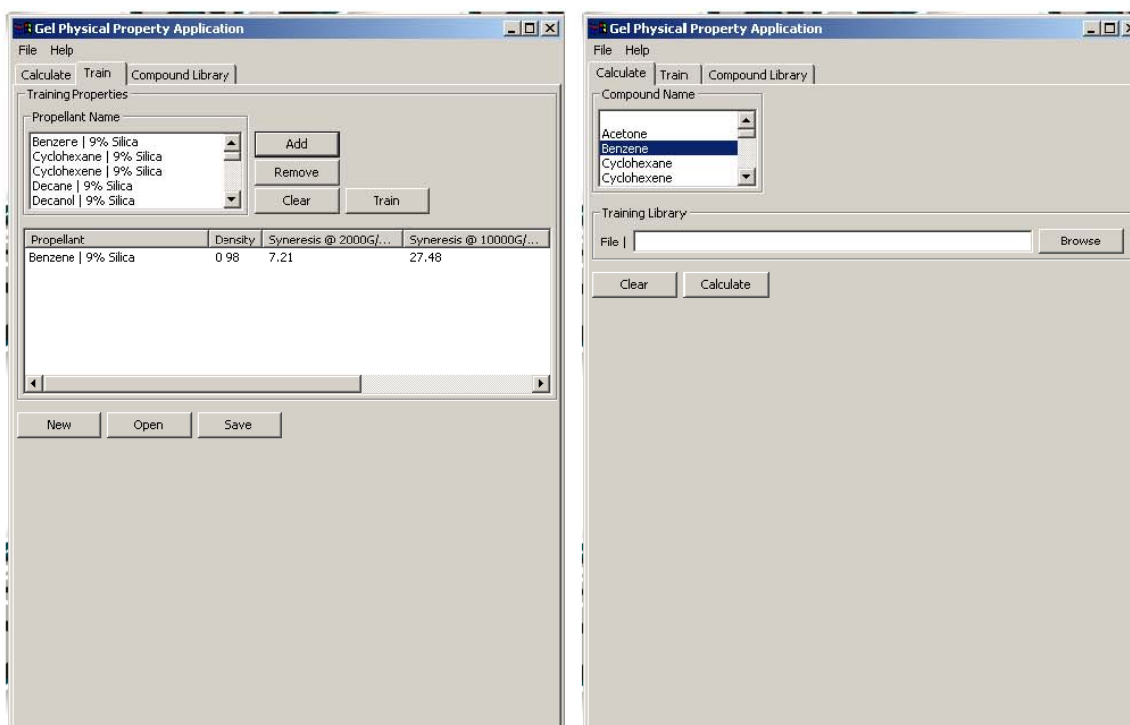


Figure 58: SOGeF GUI Application Windows: (Left) Screenshot of calculate page
(Right) Screenshot of training page

4.4 Dynamic Brownian / Stokesian Gelation Simulation

The modeling techniques of Brownian and Stokesian dynamics were established for strong attractive forces in Phase I. The focus of the Phase II effort was to develop parameterized forces, which include: van der Waals, solvation, depletion, and repulsive charge. Unfortunately, these forces depend on the type of solvent used. To date, only water solvents have been modeled.

In the Brownian dynamics approach, the silica particles are assumed to be much larger than the solvent particles. This approach is justified, in our case, by the fact that the silica particles are estimated to be at least 40,000 times more massive than the solvent molecules. Consequently, the solvent was modeled as a stationary continuum and only the motion of the silica particles were tracked. The particles move by the influence of inter-particle forces as well as the drag exerted by the solvent. In addition, random thermal motion is specified through Brownian modeling.

The inter-particle force potential (U) was modeled with the following equation:

$$\frac{U(r)}{k_B T} = 4A \cdot [(2/r)^{12} - (2/r)^6 + \exp(-r/2)/r]$$

Where r is the non-dimensional distance (with respect to particle radius) between particle centers (i.e. $r = 2$ implies contact). Figure 59 shows a potential barrier occurring just before contact followed by a closer stable “bonding” well.

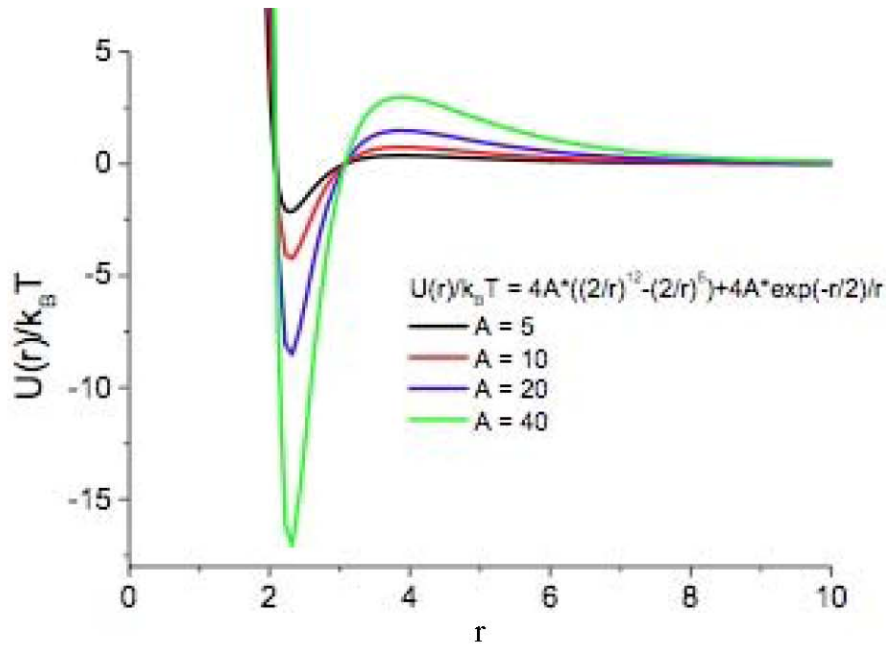


Figure 59: Form of the inter-particle force typical of silica in aqueous environments. The repulsive portion with local maximum away from contact ($r=2$) is due to charged surface

Figures 60 and 61 shown comparisons of the Stokesian and Brownian models for the prediction of mean square displacement and number of particle bonds respectively. Notice that bonds can be broken (Figure 61) and that the Stokesian model shows a slower gelation process (due to a larger hydrodynamic force).

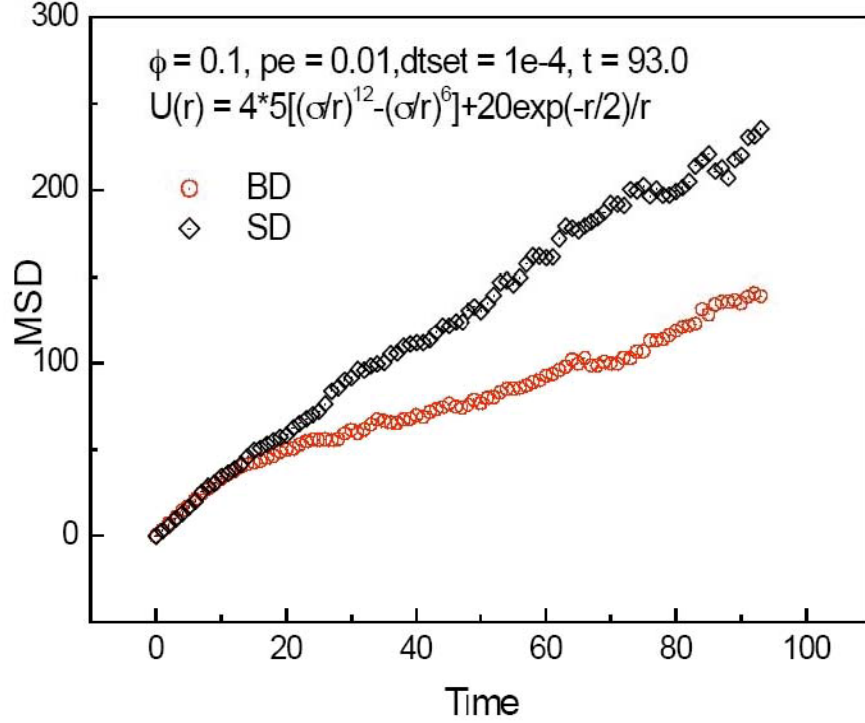


Figure 60: Mean square displacement (in units of particle radius a) as a function of dimensionless time, $t^* = Dt/a^2$ with D the bare-particle diffusion constant (Stokes-Einstein) for simulations by Brownian and Stokesian Dynamics (BD, SD) of identical initial configurations; the simulations differ in BD lacking hydrodynamic interactions which are rigorously accounted in SD. These are conditions yielding strong gels

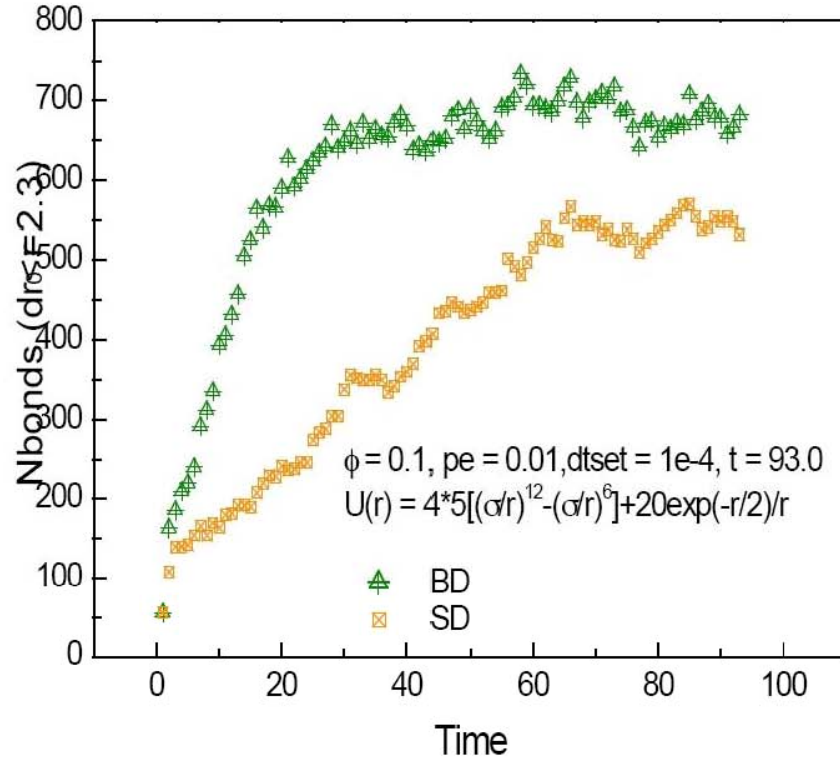


Figure 61: Number of bonds, defined as particle pairs having centers within 2.3 radii, as a function of dimensionless time with 124 particles in the unit cell

One flaw in the model is that the predicted aggregates form densely packed clusters (see Figure 62: Left), as apposed to a space-filling network typical of gels. The flaw is quantified by the pair distribution shown in Figure 62 (Right). Notice the high number of particles inside the “bonding” well. This tendency is believed to occur as a result of inadequate contact “frictional” modeling, which would prevent the fractal structures from collapsing.

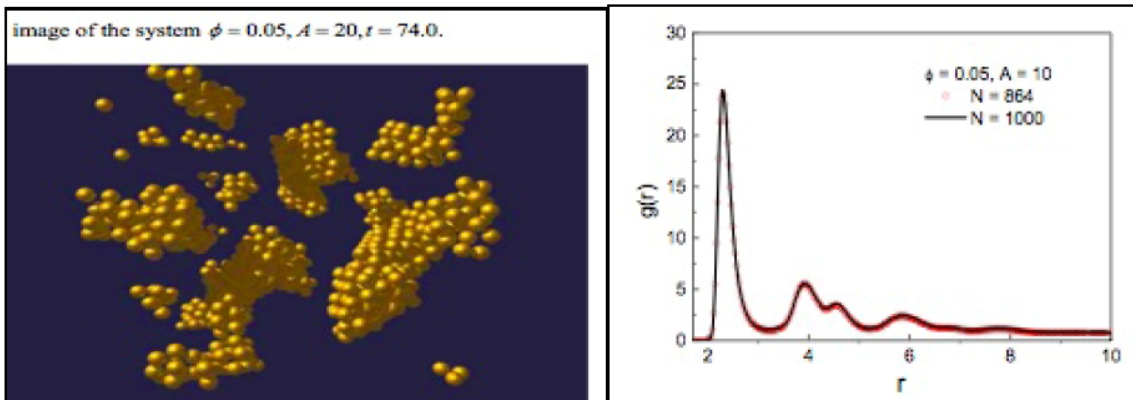


Figure 62: (Left) Snapshot of particle configuration for an initially uniformly distributed system, with 1000 particles in the unit cell, at solids fraction of $\phi = 0.05$ and the force parameter (see Fig 3) of $A=20$. (Right) The pair distribution function of a gelling system, showing large value at contact and local crystalline ordering.

The simulation tools, developed in Phase I and II, have two major drawbacks. First, the Accelerated Stokesian Dynamics model (ASD as described in **10**) limits system size and requires excessive run-time to achieve gelation, due to rigorous hydrodynamic calculations. Secondly, the Brownian Dynamics (BD) model, while allowing much larger system sizes and reduced computation time, does not account for realistic hydrodynamic interaction. A compromise can be established between the two models, as in **(11)**, where only hydrodynamic interactions of close pair particles are modeled. Far pair hydrodynamic interactions are captured through a “mean field” approach, which involves a systematic account of the added dissipation. This accelerates the overall method by more than an order of magnitude, with little loss in physical accuracy.

5. SUMMARY

The main goal of this STTR Phase II project was to develop a software tool to assist in the synthesis and optimization of gelled propellants. CFDRC successfully accomplished this goal with the creation of SOGeF. SOGeF is a neural network-based QSPR gel prediction algorithm wrapped in a convenient and robust GUI. The main advantage of SOGeF over physical-based models is that input parameters are easily identified at the macroscopic level. In addition, SOGeF predictions are explicit and do not require lengthy gelation simulations.

Validation and training of SOGeF began with the creation of an extensive gel database. In Phase II, over 39 different organic-based gels were prepared, whose various physical properties were measured by CFDRC, NJIT, and CCNY. Comparisons of predictions made by SOGeF to removed elements in the training database were promising and it is expected that accuracy will only get better as the number of training sets grows.

6. CONCLUSIONS

The overall conclusion from the Phase II study is that SOGeF is an extremely powerful tool for the synthesis and optimization of gelled propellants. A key advantage of SOGeF is that model predictions are explicit and do not require lengthy gelation simulations. In addition, SOGeF input parameters are easily identified, as apposed to the challenging specification physical identifiers in gelation models. Also, as the size of the training database grows, predictions from SOGeF will only become more reliable, whereas the accuracy of physical models is relatively fixed.

The main conclusions of the Phase II work can be summarized as follows:

1. Gel preparation

- a. It is necessary to mix gels thoroughly and relatively quick. Once a gel is established, it is impossible to increase its silica content.
- b. Preparation of alcohol-based gels requires the use of surfactants in order to reduce interfering hydrogen bonds between the solvent and silica network.
- c. Strong gels were formed from alkanes, alkenes, and cyclic alkanes, while weak gels were formed from the alcohols and acetone solvents.
- d. The influence of operator variability in preparing the gels had very little impact on their consistency.
- e. It was necessary to increase the silica content of the organic gels from 9 to 11% in order to improve the 50-caliber test pass rate.

2. Measurement observations

- a. Silica content has the most influence on the gel properties of a specific organic group.
- b. Storage time has a substantial impact on the properties of organic-based gels. This is believed to be a result of solvent evaporation.
- c. The syneresis of organic-based gels shows a strong dependence on the magnitude of acceleration exposure, with a minimal dependence on the duration of exposure. Once a gel is exposed to a given acceleration, it immediately loses a fixed amount of solvent.
- d. The presence of an –OH functionality in a solvent results in poor gelation.
- e. DLS and rotational rheometry form comparable estimates of gelation time.
- f. Salt was critical to the formation of aqueous colloidal silica gels, as it destabilizes the repulsive silica charges. The effect becomes saturated at large salt levels, where the structural growth is limited solely by diffusion.

3. Neural Network functionality

- a. The chosen descriptor set forms well-defined PDI patterns in the alcohol-based gels. This was mostly a result of the inherent ability of accentric factor to distinguish organic groups.
- b. In general, error in the training fit forms an upper bound on predictability.
- c. Spread in the training data directly scales into the errors seen in the training fit. Consequently, relative error will be biased towards larger values in the training set.

- d. Re-training the network on its fit error can counteract issues arising from training variable spread and local error minimums. The size of the re-trained network can be much smaller than the original network.
- e. Errors in training data can significantly warp the networks output. Consequently, it is crucial that missing data not be replaced by arbitrary values (the network was designed to disregard missing data).
- f. SNC has value not only in selecting an appropriate network size, but also in reducing the prediction risk associated with that size. It is therefore advisable to periodically re-train the network using SNC as new training data becomes available.

7. RECOMMENDATIONS

- ***Gel Database***
 - Collect more data to broaden the networks prediction ability
 - Collect repeat samples to establish random error in network training
- ***Neural Network (QSPR)***
 - Further optimize descriptor variable selection, as an automated process (Input Variable Pruning)
 - Explore the use of different error functions (relative error) to eliminate variable spread issues
 - Detect and optimize the networks ability to establish random error in the training data
 - Further explore network error re-training to obtain optimal models
 - As new training data is acquired, the network should be periodically re-trained using SNC
- ***Gelation Modeling***
 - Determine force fields for various organic solvent types
 - Adopt a compromised model, as in (11), to decrease run-time and increase system size
 - Include particle-particle friction so that space filling networks can be modeled (apposed to the current collapsed networks)

9. REFERENCES

- 1- Gabriela Espinosa, Denise Yaffe, Yoram Cohen, Alex Arenas, and Francesc Giralt, "Neural Network Based Quantitative Structural Property Relations (QSPRs) for Predicting Boiling Points of Aliphatic Hydrocarbons *J. Chem. Inf. Comput. Sci.* **2000**, *40*, 859-879
- 2- Prediction Risk and Neural Network Architecture Selection, John Moody, in *From Statistics to Neural Networks: Theory and Pattern Recognition Applications*, V. Cherkassky, J.H. Friedman, and H. Wechsler (eds), Springer-Verlag, 1994.
- 3- Brinker, C. J. & Scherer, G. W. *Sol-Gel Science: The Physics and Chemistry of Sol-Gel Processing* Academic Press (1989).
- 4- Richter, S., Matzker, R. and Schroeter, K. "Gelation Studies 4. Why do "Classical" Methods like Oscillatory Shear Rheology and Dynamic Light Scattering for Characterization of the Gelation Threshold Sometimes Not Provide Identical Results Especially on Thermoreversible Gels?" *Macromol. Rapid Commun.* **26**, 1626-1632 (2005).
- 5- P. N. Pusey and W. van Megen 1989 Dynamic light scattering by non-ergodic media. *Physica A* **157**, 705.
- 6- Winter, H. H., and Chambon, F., "Analysis of linear viscoelasticity of a crosslinking polymer at the gel point" *J. Rheol.* **30**, 367-382 (1986).
- 7- Roberto Di Salvo, *Computational Design Tool for the Synthesis and Optimization of Gel Formulations, Phase I Report*
- 8- March: *Advanced Organic Chemistry*, 2nd ed. 1981
- 9- Raghavan, S.R., Walls, H. J. & Khan, S. A. Rheology of silica dispersions in organic liquids: New evidence for solvation forces dictated by hydrogen bonding. *Langmuir* **16**, 7920-7930 (2000).
- 10- A. Banchio and J. F. Brady 2003 Accelerated Stokesian dynamics: Brownian motion. *J. Chem. Phys.* **118**, 10323.
- 11- J. J. L. Higdon 2007 (U. Illinois) Private communication.

Appendix A (Solvent Descriptor Values)

	(g/ccm) 25°C	(mPa*sec) 25°C	(mN/m) 25°C	(20°C)	kPa (25°C)		(Debye)	(kJ/mol) 298K	100=msc (g/100mL)	(°C)	(°C)
Comp/Param	Rho	Visc	SurfTens	DielCon st	VapPress	AccFact	Dipole M	Std HF	WaterSol	MeltP	BoilP
iso-Pentane	0.6	0.214	14.45	1.845	79.3	0.2296	0.1	-179	0	-160	27.88
Heptane	0.684	0.387	19.66	1.9209	6.09	0.349	0	-224.4	0	-91	98.4
Octane	0.703	0.508	21.14	1.948	1.86	0.393	0.07	-250.3	0	-57	125.67
iso-Octane	0.688	0.473	18.77	1.94	6.6	0.303	0	-259	0	-107	99.22
CycloHexane	0.7785	0.894	24.65	2.0243	13	0.211	0	-156.4	0	7	80.73
Hexene	0.6731	0.252	17.9	2.077	24.8	0.281	0	-74.2	0.005	-140	63.48
Benzene	0.8765	0.604	28.22	2.2825	12.7	0.209	0	49.1	0.179	6	80.09
Diethyl Amine	0.7056	0.319	19.85	3.68	30.1	0.291	0.92	-103.7	81	-50	55.5
n-PropylAmine	0.7173	0.376	21.75	5.08	42.1	0.303	1.17	-101.5	100	-83	47.22
Cyclohexene	0.811	0.625	26.17	2.2176	11.8	0.2312	0.332	-38.5	0	-103	82.98
n-Pentane	0.626	0.224	15.49	1.8371	68.3	0.251	0	-173.5	0.01	-130	36.06
Hexane	0.6548	0.294	17.59	1.8865	20.2	0.299	0.05	-198.7	0.0013	-95	68.73
Decane	0.73	0.838	23.37	1.9853	0.2	0.488	0.07	-301	0	-30	174.15
MEK	0.8054	0.405	23.97	18.56	12.6	0.32	2.78	-273.3	29	-87	79.59
Acetone	0.7899	0.306	23.46	21.01	30.8	0.306	2.88	-248.4	100	-95	56.05
MIBK	0.7978	0.545	23.9	13.11	2.64	0.37	4.2	-305.3	1.91	-84	116.5
Decanol	0.8297	10.91	28.51	7.93	0.009	0.624	1.8	-478.1	0.37	7	231.1
Methanol	0.7914	0.544	22.07	33	16.9	0.565	1.7	-239.2	100	-97	64.6
NitroCH4	1.1371	0.63	36.53	37.27	4.79	0.31	3.46	-112.6	10	-28	101.19
NitroProp	0.9961	0.798	29.29	24.7	1.36	0.376	3.66	-167.2	1.4	-108	131.1
NitroEthane	1.0448	0.688	32.13	29.11	2.79	0.341	3.23	-143.9	4.6	-89	114
Triethyl Amine	0.7275	0.347	20.22	2.418	7.7	0.32	0.61	-127.7	17	-115	89
1-Propanol	0.8035	1.945	23.32	20.8	0.154	0.628	1.55	-302.6	100	-126	97.2

surfactant

surfactant

Dibutyl Amine	0.767	0.918	24.12	2.765	0.34	0.329	1	-206	3.5	-62.15	159.6
1-Pentanol	0.8144	3.5	25.6	13.9	0.293	0.621	1.712	-295.63	2.1956	-78.2	137.983
n-ButylAmine	0.74	0.5	16.87	5.4	12.23	0.285	1.361	-94.98	100	-49	77

Appendix B (Additional Syneresis Data)

s/n	Solvent/Liquid	Serial No.	Composition	500G	
				5min	90min
1	n-Pentane	082307-01	9% Cabosil	0.93	0.402
2	Iso-Pentane	082307-02	9% Cabosil	0.34	0.67
3	Hexane	082207-01	9% Cabosil	0.2	0.134
4	Heptane	081407-01	9% Cabosil	0.06	0.135
5	Octane	082807-01	9% Cabosil	0.06	0.134
6	Iso-Octane	090607-01	9% Cabosil	1.73	1.54
7	Decane	082907-01	9% Cabosil	0.067	0.73

s/n	Solvent/Liquid	Serial No.	Composition	2000G			
				5min	10min	30min	90min
1	n-Pentane	082307-01	9% Cabosil	0.4			0.6
2	Iso-Pentane	082307-02	9% Cabosil	0.61			1.15
3	Hexane	082207-01	9% Cabosil	0.5			2.98
4	Heptane	081407-01	9% Cabosil	3.3			5.19
5	Octane	082807-01	9% Cabosil	6.75			8.39
6	Iso-Octane	090607-01	9% Cabosil	12.41			11.5
7	Decane	082907-01	9% Cabosil	9.72			9.86
8	1 - Propanol	032508-02	9% Cabosil, no Duomeen		35.64257	38.05896	39.10955
9	Nitroethane	022508-01	9% Cabosil		4.633094	7.477567	7.677275
10	Nitropropane	022708-01	9% Cabosil		6.028267	7.954173	9.494894
11	Benzene	021808-01	9% Cabosil		5.826636	3.969884	7.205179
12	Acetone	031108-01	9% Cabosil		28.56252	29.54695	34.17266
13	Nitromethane	022808-01	9% Cabosil		1.945412	4.154495	3.063759
14	Methanol	031208-01	9% Cabosil, 0.9% Surfactant		28.5155	29.89409	31.6416
15	Cyclohexane	021108-01	9% Cabosil		8.014049	9.330223	10.18804
16	1 - Hexene	021908-01	9% Cabosil		8.090379	6.284737	8.571429
17	1-Octanol	032008-01	9% Cabosil, 0.9% Duomeen		6.430077	34.1629	32.65993
18	1-Butanol	032708-01	9% Cabosil, 0.9% Duomeen		31.96605	35.98039	38.34163
19	Methyl-Ethyl Ketone	032608-02	9% Cabosil		39.16376	41.15409	40.53167
20	1-Propanol	031308-01	9% Cabosil, 0.9% Duomeen		23.31774	34.13249	37.04553
21	Cyclohexene	021308-01	9% Cabosil		1.739467	2.091768	2.217529
22	1-Hexanol	040208-02	9% Cabosil, 0.9% Duomeen				41.11963
23	Decanol	042208-01	9% Cabosil				12.96417
24	Triethyl Amine	042408-01	9% Cabosil				25.34562
25	n-Propyl Amine	042908-01	9% Cabosil				41.04596
26	Hexane	040308-01	11% Cabosil				7.177211
27	Diethyl Amine	043008-01	9% Cabosil				25.54897
28	Methyl-Ethyl Ketone	051408-01	11% Cabosil				33.07692
29	MIBK	052108-01	11% Cabosil				29.93241
30	Nitromethane	060408-01	11% Cabosil				0.03308
31	Decane	050508-01	11% Cabosil				5.804579
32	Acetone	051508-01	11% Cabosil				27.21722
33	MIBK	052008-01	9% Cabosil				33.95739
34	Nitropropane	060508-01	11% Cabosil				2.570778
35	Nitropropane	060908-01	11% Cabosil				0.032478
36	Methanol	060308-01	11% Cabosil				32.69105
37	Pentane	050708-01	11% Cabosil				0.119713
38	1-Decanol	060208-01	11% Cabosil				4.068241

s/n	Solvent/Liquid	Serial No.	Composition	5000G						
				5min	10min	15min	20min	25min	30min	90min
1	n-Pentane	082307-01	9% Cabosil	1.803607	0.475543	2.93725	1.615074	3.686327	3.459747	2.374491
2	Iso-Pentane	082307-02	9% Cabosil	7.138001	6.875834	8.198925	10.35404	8.916324	10.73826	10.79812
3	Hexane	082207-01	9% Cabosil	9.58445	9.716599	9.479306	9.659864	12.64446	12.20499	13.34675
4	Heptane	081407-01	9% Cabosil	9.986684	10.13423	9.152086	11.13333	11.32708	11.16342	12.56684
5	Octane	082807-01	9% Cabosil	16.70007	16.19813	16.34031	15.98934	18.27815	18.28533	16.84492
6	Iso-Octane	090607-01	9% Cabosil	19.1689	21.45722	20.09346	20.0133	21.9661	21.70963	20.73579
7	Decane	082907-01	9% Cabosil	18.67835	20.52314	17.38255	19.09212	21.30376	20.63385	20.10688

s/n	Solvent/Liquid	Serial No.	Composition	10000G					
				5min	10min	15min	20min	25min	30min
1	n-Pentane	082307-01	9% Cabosil	5.970149		8.296943	4.477612	6.841339	6.153846
2	Iso-Pentane	082307-02	9% Cabosil	9.538462		12.85714	7.575758	17.3913	11.11111
3	Hexane	082207-01	9% Cabosil	13.04348		13.63636	18.84058	18.08346	17.14286
4	Heptane	081407-01	9% Cabosil	13.23529		17.46479	16.41791	23.52941	17.3913
5	Octane	082807-01	9% Cabosil	19.69697		20.58824	18.46154	23.97661	21.6954
6	Iso-Octane	090607-01	9% Cabosil	23.8806		24	27.53623	26.47059	25.75758
7	Decane	082907-01	9% Cabosil	22.64706		23.05556	20.89552	24.63768	23.52941
8	1 - Propanol	032508-02	9% Cabosil, no Duomeen		47.9228				52.40642
9	Nitroethane	022508-01	9% Cabosil		23.45361				27.63701
10	Nitropropane	022708-01	9% Cabosil		24.84096				28.98507
11	Benzene	021808-01	9% Cabosil		24.7858				27.48188
12	Acetone	031108-01	9% Cabosil		42.27359				43.46532
13	Nitromethane	022808-01	9% Cabosil		22.09945				23.91559
14	Methanol	031208-01	9% Cabosil, 0.9% Surfactant		42.93177				46.726
15	Cyclohexane	021108-01	9% Cabosil		29.10401				30.58036
16	1 - Hexene	021908-01	9% Cabosil		28.32529				31.98847
17	1-Octanol	032008-01	9% Cabosil, 0.9% Duomeen		39.95098				39.55479
18	1-Butanol	032708-01	9% Cabosil, 0.9% Duomeen		48.03615				47.72539
19	Methyl-Ethyl Ketone	032608-02	9% Cabosil		50.43449				50.50882
20	1-Propanol	031308-01	9% Cabosil, 0.9% Duomeen		41.42471				47.44452
21	Cyclohexene	021308-01	9% Cabosil		22.1413				22.769
22	1-Hexanol	040208-02	9% Cabosil, 0.9% Duomeen						50.2928
23	Decanol	042208-01	9% Cabosil						24.44366
24	Triethyl Amine	042408-01	9% Cabosil						43.50243
25	n-Propyl Amine	042908-01	9% Cabosil						52.48933
26	Hexane	040308-01	11% Cabosil						29.64061
27	Diethyl Amine	043008-01	9% Cabosil						43.15899
28	Methyl-Ethyl Ketone	051408-01	11% Cabosil						43.17223
29	MIBK	052108-01	11% Cabosil						41.25989
30	Nitromethane	060408-01	11% Cabosil						14.58333
31	Decane	050508-01	11% Cabosil						22.95835
32	Acetone	051508-01	11% Cabosil						36.67322
33	MIBK	052008-01	9% Cabosil						63.18153
34	Nitropropane	060508-01	11% Cabosil						20.25565
35	Nitropropane	060908-01	11% Cabosil						17.2391
36	Methanol	060308-01	11% Cabosil						42.12466
37	Pentane	050708-01	11% Cabosil						19.85637
38	1-Decanol	060208-01	11% Cabosil						7.23

s/n	Solvent/Liquid	Serial No.	Composition	30000G	
				5min	90min
1	n-Pentane	082307-01	9% Cabosil	30.04	29.09
2	Iso-Pentane	082307-02	9% Cabosil	35.4	38.51
3	Hexane	082207-01	9% Cabosil	37.82	40
4	Heptane	081407-01	9% Cabosil	35.66	39.98
5	Octane	082807-01	9% Cabosil	38.23	42.64
6	Iso-Octane	090607-01	9% Cabosil	41.58	46.68
7	Decane	082907-01	9% Cabosil	36.94	42.75

Appendix C (NN Code Listing)

```

#include <stdio.h>
#include <stdlib.h>
#include <math.h>

int Activation=1; //0-sigmoid 1-(x2->x)
int Run=1; //0-Train from 0
(SNC) 1-Train from wo (train with H from file) 2-Output
int I=11; //Dimension of input
int O=1; //Dimension of output
int N=16; //Number of training sets
int H=12; //Maximum # of hidden
neurons
char wo_dat[50]="wo.dat", vo_dat[50]="vo.dat";

#define maxI 11 //maxDimension of
input (need dynamic memory)
#define maxO 6 //maxDimension of
output (need dynamic memory)
#define maxN 50 //maxNumber of training sets
(need dynamic memory)
#define maxH 23 //Maximum # of
hidden neurons (need dynamic memory)

int I_temp, O_temp, N_temp, H_temp; //Used to train subsets
float Input[maxN][maxI];
float Output[maxN][maxO];
float ScaledInput[maxN][maxI]; //Must scale unless using %
error
float ScaledOutput[maxN][maxO];
float maxIn[maxI],minIn[maxI],maxOut[maxO],minOut[maxO];
float w[maxI+1][maxH],v[maxH+1][maxO]; //Weights
including thresholds
float w_temp[maxI+1][maxH],v_temp[maxH+1][maxO];
float w_optimal[maxI+1][maxH],v_optimal[maxH+1][maxO];
float Input_temp[maxN][maxI], Output_temp[maxN][maxO];
int w_test[maxI+1][maxH],v_test[maxH+1][maxO]; //set 0 to hold
constant
float mu=0.02; //Initial step size

void LoadData(){
    FILE *LiquidFile=fopen("LiquidData.txt","r");
    FILE *GelFile=fopen("GelData.txt","r");
    int i,j,read;

```

```

fscanf(LiquidFile, "%i", &Run);
fscanf(LiquidFile, "%i", &Activation);
fscanf(LiquidFile, "%i", &I);
fscanf(LiquidFile, "%i", &N);
fscanf(LiquidFile, "%i", &H);
fscanf(LiquidFile, "%s", &wo_dat[0]);
fscanf(LiquidFile, "%s", &vo_dat[0]);

fscanf(GelFile, "%i", &O);
fscanf(GelFile, "%i", &read);
if(read!=N){printf("Incompatible liquid and gel files\n");}

for(i=0; i<N; i++){
    for(j=0; j<I; j++){
        fscanf(LiquidFile, "%f", &Input[i][j]);

        if(i==0){maxIn[j]=Input[i][j]*1.1; minIn[j]=Input[i][j]*0.9;} //Larger range for
        extrapolation under sigmoid activation
        else{
            if(maxIn[j]<Input[i][j]*1.1){maxIn[j]=Input[i][j]*1.1;}
            if(minIn[j]>Input[i][j]*0.9){minIn[j]=Input[i][j]*0.9;}
        }
    }
    for(j=0; j<O; j++){
        fscanf(GelFile, "%f", &Output[i][j]);
        if(i==0){maxOut[j]=Output[i][j]*1.1; minOut[j]=Output[i][j]*0.9;}
        else{
            if(maxOut[j]<Output[i][j]*1.1){maxOut[j]=Output[i][j]*1.1;}

            if(minOut[j]>Output[i][j]*0.9){minOut[j]=Output[i][j]*0.9;}
        }
    }
}

for(i=0; i<N; i++){
    for(j=0; j<I; j++){ScaledInput[i][j]=Input_temp[i][j]=(Input[i][j]-
minIn[j])/(maxIn[j]-minIn[j]);}
    for(j=0; j<O; j++){ScaledOutput[i][j]=Output_temp[i][j]=(Output[i][j]-
minOut[j])/(maxOut[j]-minOut[j]);}
}
fcloseall();
}

int ResetWeights(){
    int i, j;

```



```

        if(Run==0 || Run==3){//3->train with given H from zero

            for(i=0;i<I+1;i++){for(j=0;j<H;j++){w_temp[i][j]=float(rand()%100)/100-
0.5;w_test[i][j]=1;}} //Small random initial weights

            for(i=0;i<H+1;i++){for(j=0;j<O;j++){v_temp[i][j]=float(rand()%100)/100-
0.5;v_test[i][j]=1;}}
        }
        else{//Load old weights from wo.dat & vo.dat
            float read;
            FILE *fp=fopen(wo_dat,"r+");

            fscanf(fp,"%f",&read);
            if(read!=I){printf("Error in weight file compatibility retrain from
0.\n");return 0;}
            fscanf(fp,"%i",&H);
            for(i=0;i<I+1;i++){for(j=0;j<H;j++){fscanf(fp,"%f",&w_temp[i][j]);
w_test[i][j]=1;}}
            if(Run==2){//Read in Min/Max values used in training.
                for(i=0;i<I;i++){fscanf(fp,"%f",&maxIn[i]);}
                for(i=0;i<I;i++){fscanf(fp,"%f",&minIn[i]);}
            }
            fclose(fp);
            fp=fopen(vo_dat,"r+");
            fscanf(fp,"%f",&read);
            if(read!=O){printf("Error in weight file compatibility retrain from
0.\n");return 0;}
            fscanf(fp,"%i",&H);
            H_temp=H;
            for(i=0;i<H+1;i++){for(j=0;j<O;j++){fscanf(fp,"%f",&v_temp[i][j]);
v_test[i][j]=1;}}
            if(Run==2){//Read in Min/Max values used in training.
                for(i=0;i<O;i++){fscanf(fp,"%f",&maxOut[i]);}
                for(i=0;i<O;i++){fscanf(fp,"%f",&minOut[i]);}
            }
            fclose(fp);
            for(i=0;i<N;i++){
                for(j=0;j<I;j++){ScaledInput[i][j]=Input_temp[i][j]=(Input[i][j]-
minIn[j])/(maxIn[j]-minIn[j]);}

                for(j=0;j<O;j++){ScaledOutput[i][j]=Output_temp[i][j]=(Output[i][j]-
minOut[j])/(maxOut[j]-minOut[j]);}
            }
        }
        return 1;
    }
}

```

```

float g(float x, int i){//Hidden Layer
    if(Activation==0){return exp(-x*x);}
    return x*x;
}
float gprime(float x, int i){
    if(Activation==0){return exp(-x*x)*-2*x;}
    return 2*x;
}

float f(float x){//Output Layer
    if(Activation==0){return exp(-x*x);}
    return x;
}
float fprime(float x){
    if(Activation==0){return exp(-x*x)*-2*x;}
    return 1;
}

float zio(int i, int set){//Input to the ith hidden neuron assuming all temps using the
(set)th training values
    float z=0;
    int m;
    z=w_temp[0][i];
    for(m=0;m<I_temp;m++){z+=w_temp[m+1][i]*Input_temp[set][m];}
    return z;
}

float yio(int i, int set){//Input to the ith output neuron assuming all temps using the (set)th
training values
    float y=0;
    int m;
    y=v_temp[0][i];
    for(m=0;m<H_temp;m++){y+=v_temp[m+1][i]*g(zio(m,set),m);}
    return y;
}

float SE(){//Square scaled error assuming all temps
    float se,yi_o;
    int o,set;
    se=0;
    for(o=0;o<O_temp;o++){
        for(set=0;set<N_temp;set++){
            yi_o=yio(o,set);
            se=se+pow(Output_temp[set][o]-f(yi_o),2.0);
        }
    }
}

```

```

        }
        return 0.5*se;
    }

void train(){//Standard training with weight removal (_test[[]])
    int maxTrainDuration=5000, t,i,j,o,h,set;
    float se,seo,seb,der,dertemp,dero;
    float yi_o;
    float norm,x,xo,dx,ds;
    float dw[maxI+1][maxH],dv[maxH+1][maxO];

    seo=se=seb=SE();
    for(t=0;t<maxTrainDuration;t++){
        norm=0;
        for(o=0;o<O_temp;o++){
            for(h=0;h<=H_temp;h++){
                der=0;
                if(v_test[h][o]==1){
                    dero=1;
                    for(set=0;set<N_temp;set++){
                        if(h!=0){dero=f(zio(h-1,set));}
                        yi_o=yio(o,set);
                        der=der-(Output_temp[set][o]-
f(yi_o))*fprime(yi_o)*dero;
                    }
                }
                dv[h][o]=-der;//Perform update all at once to avoid error
growth
                norm=norm+pow(der,2.0);
            }
        }
        for(h=0;h<H_temp;h++){
            for(i=0;i<=I_temp;i++){
                der=0;
                if(w_test[i][h]==1){
                    dero=1;
                    for(set=0;set<N_temp;set++){
                        if(i!=0){dero=Input_temp[set][i-1];}
                        dertemp=0;
                        for(o=0;o<O_temp;o++){
                            yi_o=yio(o,set);
                            dertemp=dertemp-
(Output_temp[set][o]-f(yi_o))*fprime(yi_o)*v_temp[h+1][o];
                        }

                    der=der+dertemp*gprime(zio(h,set),h)*dero;
                }
            }
        }
    }
}

```

```

        }
    }
    dw[i][h]=-der;
    norm=norm+pow(der,2.0);
}
}
ds=pow(norm,0.5);
norm=1;
x=0;
xo=0;
dx=mu;
for(j=0;j<1000;j++){

    for(o=0;o<O_temp;o++){for(h=0;h<=H_temp;h++){v_temp[h][o]=v_temp[h][o]
+dx*dv[h][o]/norm;}}

    for(h=0;h<H_temp;h++){for(i=0;i<=I_temp;i++){w_temp[i][h]=w_temp[i][h]+dx
*dw[i][h]/norm;}}

        x=x+dx;
        se=SE();
        if(se<=seo){seo=se;xo=x;}
        if(se>seo){
            dx=(xo-x)/2.0;
        }
        if(fabs(dx)<=(mu/128)){break;}
    }
    printf("%i\tsef=%e\txf=%f\n",t,seo,xo);
    if(se>seo){
        dx=xo-x;

        for(o=0;o<O_temp;o++){for(h=0;h<=H_temp;h++){v_temp[h][o]=v_temp[h][o]
+dx*dv[h][o]/norm;}}

        for(h=0;h<H_temp;h++){for(i=0;i<=I_temp;i++){w_temp[i][h]=w_temp[i][h]+dx
*dw[i][h]/norm;}}

            x=x+dx;
        }
        if(fabs(xo)<=0 && t>=50){break;}
    }
}

float PRtrain(){//V-fold cross validation training
    float CV,CVj;
    int v_div=3, //Larger v_div will train slower but form better PR
        i,j,h,o,Nd,subgroup, N_tempPR;

```

```

train(); //Train with all N_temp data sets
CV=0;
N_tempPR=N_temp;
for(o=0;o<O_temp;o++){for(h=0;h<=H_temp;h++){v[h][o]=v_temp[h][o];}}
for(h=0;h<H_temp;h++){for(i=0;i<=I_temp;i++){w[i][h]=w_temp[i][h];}}
Nd=N_temp/v_div;
if(v_div*Nd<N_temp){Nd=Nd+1;}
for(subgroup=0;subgroup<Nd;subgroup++){

    for(o=0;o<O_temp;o++){for(h=0;h<=H_temp;h++){v_temp[h][o]=v[h][o];}}//Start
    art from same location as full training

    for(h=0;h<H_temp;h++){for(i=0;i<=I_temp;i++){w_temp[i][h]=w[i][h];}}
        N_temp=0;
        for(i=0;i<N_tempPR;i++){
            if(i<subgroup*Nd || i>=(subgroup+1)*Nd){

for(j=0;j<O_temp;j++){Output_temp[N_temp][j]=ScaledOutput[i][j];}

for(j=0;j<I_temp;j++){Input_temp[N_temp][j]=ScaledInput[i][j];}
                N_temp=N_temp+1;
            }
        }
        train();
        CVj=0;
        for(i=0;i<N_tempPR;i++){
            if(i>=subgroup*Nd && i<(subgroup+1)*Nd){

for(j=0;j<O_temp;j++){Output_temp[i][j]=ScaledOutput[i][j];}
                for(j=0;j<I_temp;j++){Input_temp[i][j]=ScaledInput[i][j];}
                for(j=0;j<O_temp;j++){CVj=CVj+pow(Output_temp[i][j]-
f(yio(j,i)),2.0)/N_temp;}
            }
        }
        CV=CV+CVj/v_div;
    }
    N_temp=N_tempPR;
    for(i=0;i<N_temp;i++){

for(j=0;j<O_temp;j++){Output_temp[i][j]=ScaledOutput[i][j];}
        for(j=0;j<I_temp;j++){Input_temp[i][j]=ScaledInput[i][j];}
    }
    for(o=0;o<O_temp;o++){for(h=0;h<=H_temp;h++){v_temp[h][o]=v[h][o];}}
    for(h=0;h<H_temp;h++){for(i=0;i<=I_temp;i++){w_temp[i][h]=w[i][h];}}
    return CV;
}

```

```

int SNC(){//Sequential network construction
    FILE *fp=fopen("H-PR.dat","w+");
    int optimalH;
    int i,j;
    float PR;
    float minPR;

    printf("SNC...\n");
    I_temp=I; O_temp=O; N_temp=N, H_temp=3;
    if(ResetWeights()==0){return -1;}
    PR=minPR=PRtrain();
    optimalH=H_temp;
        printf("PR(H=%i)=%f\n",H_temp,PR);
        fprintf(fp,"PR(H=%i)=%f\n",H_temp,PR);
    for(H_temp=5;H_temp<=H;H_temp+=2){
        for(i=0;i<I_temp+1;i++){for(j=0;j<H_temp-1;j++){w_test[i][j]=0;}}
        for(i=0;i<H_temp;i++){for(j=0;j<O;j++){v_test[i][j]=0;}}
        train();//1st train with old weights held fixed
        for(i=0;i<I_temp+1;i++){for(j=0;j<H_temp-1;j++){w_test[i][j]=1;}}
        for(i=0;i<H_temp;i++){for(j=0;j<O;j++){v_test[i][j]=1;}}
        PR=PRtrain();//2nd train on all weights
        if(PR<minPR){
            minPR=PR; optimalH=H_temp;

            for(i=0;i<I_temp+1;i++){for(j=0;j<H_temp;j++){w_optimal[i][j]=w_temp[i][j];}
        }

            for(i=0;i<=H_temp;i++){for(j=0;j<O_temp;j++){v_optimal[i][j]=v_temp[i][j];}}
            }
            printf("PR(H=%i)=%f\tSE=%f\n",H_temp,PR,SE());
            fprintf(fp,"PR(H=%i)=%f\tSE=%f\n",H_temp,PR,SE());
            if(PR<0.0000005){break;}
            }

        for(i=0;i<I_temp+1;i++){for(j=0;j<optimalH;j++){w_temp[i][j]=w_optimal[i][j];
    }}
    for(i=0;i<=optimalH;i++){for(j=0;j<O_temp;j++){v_temp[i][j]=v_optimal[i][j];}
    }

    fcloseall();
    return optimalH;
}

void PrintFit(){
    FILE *fp=fopen("Fit.dat","w+");
    int o, set;

```

```

float yn,yr;
fprintf(fp,"H=%i\n",H_temp);
fprintf(fp,"True\\tFit\\tError\\n");
printf("H=%i\n",H_temp);
printf("True\\tFit\\tError\\n");
for(set=0;set<N_temp;set++){
    for(o=0;o<O_temp;o++){
        yn=f(yio(o,set))*(maxOut[o]-minOut[o])+minOut[o];
        yr=ScaledOutput[set][o]*(maxOut[o]-minOut[o])+minOut[o];
        fprintf(fp,"%f\\t%f\\t%f\\n",yr,yn,fabs(yr-yn)/(yr)*100);
        printf("%f\\t%f\\t%f\\n",yr,yn,fabs(yr-yn)/(yr)*100);
    }
}
fcloseall();
}

void PrintWeights(){
    int i,j;
    FILE *fp=fopen(wo_dat,"w+");
    fprintf(fp,"%i\\n%i\\n",I_temp,H_temp);
    for(i=0;i<I_temp+1;i++){for(j=0;j<H_temp;j++){fprintf(fp,"%f\\t",w_temp[i][j]);}
fprintf(fp,"\\n");}
    fprintf(fp,"\\n");
    for(i=0;i<I_temp;i++){fprintf(fp,"%f\\t",maxIn[i]);}
    fprintf(fp,"\\n");
    for(i=0;i<I_temp;i++){fprintf(fp,"%f\\t",minIn[i]);}
    fclose(fp);

    fp=fopen(vo_dat,"w+");
    fprintf(fp,"%i\\n%i\\n",O_temp,H_temp);
    for(i=0;i<H_temp+1;i++){for(j=0;j<O;j++){fprintf(fp,"%f\\t",v_temp[i][j]);}fprintf
f(fp,"\\n");}
    fprintf(fp,"\\n");
    for(i=0;i<O;i++){fprintf(fp,"%f\\t",maxOut[i]);}
    fprintf(fp,"\\n");
    for(i=0;i<O;i++){fprintf(fp,"%f\\t",minOut[i]);}
    fclose(fp);
}


int main(){
    LoadData();
    if(Run==2){
        ResetWeights();
        H_temp=H; I_temp=I; O_temp=O; N_temp=N;
        PrintFit();
    }
}

```

```

else{
    if(Run==0){
        H_temp=SNC();
        I_temp=I; O_temp=O; N_temp=N;
        train();
        if(H_temp==-1){return 0;}
    }
    else{
        ResetWeights();
        H_temp=H; I_temp=I; O_temp=O; N_temp=N;
        printf("Re-training with H=%i from last training
values\n",H_temp);
        train();
    }
    PrintWeights();
    PrintFit();
}
return 1;
}

```


REPORT OF INVENTIONS AND SUBCONTRACTS (Pursuant to "Patent Rights" Contract Clause) (See instructions on Reverse side.)							Form Approved OMB No. 9000 0095 Expires Oct 31, 2004		
Public reporting burden for this collection of information is estimated to average 5 minutes per response, including the time for reviewing instructions, searching existing data sources, gathering and maintaining the data needed, and completing and reviewing the collection of information. Send comments regarding this burden estimate or any other aspect of this collection of information, including suggestions for reducing this burden, to Washington Headquarters Services, Directorate for Information Operations and Reports, 1215 Jefferson Davis Highway, Suite 1204, Arlington, VA 22202-4302, and to the Office of Management and Budget, Paperwork Reduction Project (0704-0297), Washington DC 20503.									
1a. NAME OF CONTRACTOR/SUBCONTRACTOR		c. CONTRACT NUMBER		2.a. NAME OF GOVERNMENT PRIME CONTRACTOR CFD Research Corporation		c. CONTRACT NUMBER W91NF-06-C-0186		3. TYPE OF REPORT (x one) <input type="checkbox"/> a. INTERIM <input checked="" type="checkbox"/> b. FINAL	
b. ADDRESS (Include ZIP Code)		d. AWARD DATE (YYMMDD)		b. ADDRESS (Include ZIP Code) 215 Wynn Drive Huntsville, AL 35805		d. AWARD DATE (YYMMDD) 06/09/29		4. REPORTING PERIOD (YYMMDD) a. FROM 06/09/29 b. TO 09/01/30	
SECTION I - SUBJECT INVENTIONS									
5. "SUBJECT INVENTIONS" REQUIRED TO BE REPORTED BY CONTRACTOR/SUBCONTRACTOR (if "None," so state)									
a. NAME(S) OF INVENTOR(S) (Last, First, MI)		b. TITLE OF INVENTION(S)		c. DISCLOSURE NO., PATENT APPLICATION SERIAL NO. OR PATENT NO.		d. ELECTION TO FILE PATENT APPLICATIONS (1) United States (2) Foreign (a) Yes (b) No (a) Yes (b) No		e. CONFIRMATORY INSTRUMENT OR ASSIGNMENT FORWARDED TO CONTRACTING OFFICER (1) Yes (2) No	
NONE		N/A		N/A		N/A N/A N/A N/A		N/A N/A	
f. EMPLOYER OF INVENTOR(S) NOT EMPLOYED BY CONTRACTOR/SUBCONTRACTOR				g. ELECTED FOREIGN COUNTRIES IN WHICH A PATENT APPLICATION WILL BE FILED					
(1)(a) Name of Inventor (Last, First, MI) NONE		(2)(a) Name of Inventor (Last, First, MI) N/A		(1) Title of Invention N/A			(2) Foreign Countries of Patent Application N/A		
(b) Name of Employer N/A		(b) Name of Employer N/A							
(c) Address of Employer (include ZIP Code) N/A		(c) Address of Employer (include ZIP Code) N/A							
SECTION II - SUBCONTRACTS (Containing a "Patent Rights" clause)									
6. SUBCONTRACTS AWARDED BY CONTRACTOR/SUBCONTRACTOR (If "None," so state)									
a. NAME OF SUBCONTRACTOR(S)		b. ADDRESS (Include ZIP Code)		c. SUBCONTRACT NO.(S)	d. DFAR "PATENT RIGHTS" (1) Clause Number (2) Date (YYMM)		e. DESCRIPTION OF WORK TO BE PERFORMED UNDER SUBCONTRACT(S)		f. SUBCONTRACT DATES (YYMMDD)
SECTION III - CERTIFICATION									
7. CERTIFICATION OF REPORT BY CONTRACTOR/SUBCONTRACTOR (Not required if <input checked="" type="checkbox"/> Small Business or <input type="checkbox"/> Non-Profit organization.) (X appropriate box)									
a. NAME OF AUTHORIZED CONTRACTOR/SUBCONTRACTOR OFFICIAL (Last, First, MI) Deborah Phipps				c. I certify that the reporting party has procedures for prompt identification and timely disclosure of "Subject Inventions," that such procedures have been followed and that all "Subject Inventions" have been reported.					
b. TITLE Sr. Contracts Specialist				d. SIGNATURE 				e. DATE SIGNED 1-30-09	